Alma Mater Studiorum · Università di Bologna

SCUOLA DI SCIENZE
Dipartimento di Fisica e Astronomia
Corso di Laurea magistrale in Astrofisica e Cosmologia

The time-resolved $E_p - L$ correlation in GRBs: characterization and implications

Relatore:
Prof. Cristian Vignali

Laureanda:
Chiara Giuri

Correlatore:
Dr. Lorenzo Amati

Sessione II
Anno Accademico 2016–2017

Indice

Abstract

Despite important observational progress in the last 20 years, our understanding of the GRB phenomenon is still affected by several and relevant open issues, including the physics of the prompt emission, the early afterglow phenomenology, the "problem" related to the trigger of the GRB activity, the emission up to GeV, the classification and identification of different classes of GRBs (long GRBs, short GRBs, X-ray flashes, sub-energetic GRBs) and their possible association with SNe and, finally, the degree of collimation of their emission. All of these issues have strong implications for a full comprehension of the nature of GRBs progenitors.
In addition, their huge luminosity and their redshift distribution up to the early Universe make GRBs very promising as cosmological tools. The most investigated way for "standardizing" GRBs and using them to measure cosmological parameters and, in perspective, the properties and evolution of "dark energy", is the correlation between the radiated energy (or luminosity) and the photon energy at which the spectrum peaks E_p (e.g., the so called "Amati relation").
The main subject of this thesis project is the further investigation of the time–resolved E_p – Luminosity correlation, based on large data sets from the BATSE/CGRO and Fermi/GBM space experiments, and its application to GRB cosmology. In our analysis we adopt the likelihood method developed by Reichardt (2001) that properly accounts for measurements uncertainties on both E_p and luminosity and parametrizes the extra-statistical scatter σ_{ext}. This is a novel (because of the adopted method) and powerful approach, that leads to a significant improvement in the estimates of cosmological parameters using GRBs with respect to previous analysis based on time-integrated or time-averaged spectra. Indeed, in time–resolved analysis we can exploit the correlation between flux and E_p existing in individual GRBs, allowing a cosmology independent and unbiased calibration of the slope and of the extra-statistical scatter of the correlation σ_{ext} and strenghten the reliability of the E_p – Luminosity correlation. This allows to improve the reliability and accuracy of the estimates of cosmological parameters through the E_p – Luminosity correlation.

The results of my thesis also provide important inputs and tests for the emission mechanisms and geometry of the prompt emission of GRBs. On the one hand, the confirmation of $E_p - Intensity$ correlation and the characterization of its properties in terms of spectral evolution provide fundamental inputs for allowing a discrimination among different emission models; on the other hand, the comparison between the dispersion of the time-resolved correlation and that obtained through the averaged spectra provides a precious estimate of the dispersion of jet opening angles, with strong implications regarding the nature of GRB progenitors and the effective rate of such events as a function of redshift.
Finally, my research activity includes also the fit of time-resolved spectra of some GRBs with both empirical models and a physical Comptonization model recently delevoped (the GRBCOMP model) and simulations of the expected contribution to this line of research by spectral measurements of GRBs through the Chinese satellite HXMT, launched in the mid of June 2017.

Sommario

Il lavoro della mia ricerca si basa sullo studio e l'analisi del fenomeno dei Gamma Ray Bursts (GRBs), le esplosioni più energetiche dell'intero Universo, i cui redshift arrivano fino a $z = 8 - 9$.
Nonostante gli importanti progressi osservativi degli ultimi 20 anni, la nostra comprensione di questo fenomeno è ancora limitata, in particolare per quanto riguarda la fisica dell'emissione prompt, la fenomenologia dell'early afterglow, la questione riguardante il motore centrale che genera l'attività dei GRBs, l'emissione fino alle più alte energie (GeV), la classificazione e l'identificazione delle differenti classi dei GRBs (i cosiddetti long GRBS, short GRBs, X-Ray Flashes e i subenergetic GRBs), la loro probabile associazione con le Supernovae, ed infine il grado di collimazione della loro emissione. Tutte queste problematiche ancora aperte sono di fondamentale importanza per la comprensione della natura dei GRBs e dei loro progenitori.
Inoltre, l'elevata luminosità da essi fornita e la loro distribuzione in redshift (fino al cosiddetto "early Universe) fanno sì che essi possano essere utilizzati come strumenti cosmologici molto promettenti. Infatti uno dei modi più diffusi per "standardizzare i GRBs e e stimare i parametri cosmologici, e quindi in prospettiva anche l'evoluzione e le proprietà della cosiddetta "Dark Energy, è la correlazione che lega la luminosità (o l'energia) irradiata e l'energia dei fotoni a cui lo spettro dei GRBs picca, ovvero la cosiddetta "Amati correlation.
Lo scopo principale di questa tesi è l'ulteriore studio della correlazione risolta temporalmente E_p – Luminosità, utilizzando vasti dataset provenienti dagli esperimenti BATSE/CGRO e Fermi/GBM, e dunque la sua applicazione alla fisica dei GRB e alla cosmologia.
Per l'analisi svolta in questo lavoro di tesi è stato adottato un metodo innovativo che prevede l'utilizzo della likelihood di Reichardt (2001), la quale tiene conto degli errori su entrambe le grandezze della correlazione e in più ne parametrizza la dispersione. Questo è un approccio del tutto innovativo (per il metodo adottato) ed assai potente, in quanto consente un significativo miglioramento nella stima dei parametri cosmologici, rispetto a quanto finora misurato tramite lo studio e l'analisi time-integrated o time-averaged. Ad esempio, l'analisi time-resolved della correlazione E_p – Flusso consente

una calibrazione sia della pendenza sia della dispersione extra-poissoniana di tale correlazione non affetta da alcuna "alterazione dovuta alla cosmologia o alla mancata conoscenza del grado di collimazione di emissione del getto. Questo permette di rendere più affidabili e accurate le stime dei parametri cosmologici attraverso la correlazione E_p – Luminosità.
Un altro risultato di questo lavoro consiste nell'aver fornito informazioni utili in relazione alla geometria e i meccanismi di emissione del prompt, fornendoci un mezzo utile alla distinzione fra i modelli che ne spiegano la fisica. Inoltre, confrontando la dispersione calcolata tramite l'analisi time-resolved con quella invece ottenuta grazie all'analisi time-integrated, si può avere una stima migliore della dispersione degli angoli del getto, con forti implicazioni circa la natura dei progenitori dei GRBs e l'effettivo tasso di tale eventi in funzione del redshift.
Infine questa attività di ricerca ha previsto anche l'analisi diretta di dati spettrali da Fermi/GBM sia con modelli empirici sia tramite l'utilizzo di un nuovo modello di Comptonizzazione recentemente sviluppato, il cosiddetto GRB-COMP model, e anche alcune simulazioni delle misure spettrali effettuate da un satellite lanciato a metà giugno, ovvero HXMT.

Capitolo 1

Introduction

1.1 The GRB phenomenon

Gamma–Ray Bursts (GRBs) are irregular pulses of hard X–ray / soft gamma–ray emissions coming from random directions across the sky, lasting from a fraction of a second up to several minutes, with a non thermal spectrum generally peaking at few hundreds keV. A typical example of GRB lightcurve is shown in Figure 1.1, while a typical GRB spectrum can be seen in Figure 1.2.
The measured rate of these phenomena by all-sky experiments on low Earth orbit (LEO) satellites is about 0.8/day and their measured fluences (i.e. averaged fluxes multiplied by the duration of burst) is typically of $10^{-7} - 10^{-4} erg/cm^2$ [110].
Nowadays, we know that they are the brightest cosmological sources in the Universe, with a redshift distribution ranging from $\sim$0.01 to more than 9 and huge energetic outputs up to 10^{54} erg in terms of isotropic energy, released in tens of seconds. However, their distance scale and luminosity, and hence their origin remained elusive for almost 30 years after their discovery in 1967 by the VELA satellites network [55].

A major contribution in the understanding of GRBs came in '90s thanks to the Burst and Transient Source Experiment (BATSE) on board of the NASA satellite Compton Gamma Ray Observatory (CGRO). It is based on NaI scintillator detectors, with 8 units covering a $\sim 2\pi$ FOV and operating in the energy range from 25 keV up to 2000 keV. Thanks to data collec-

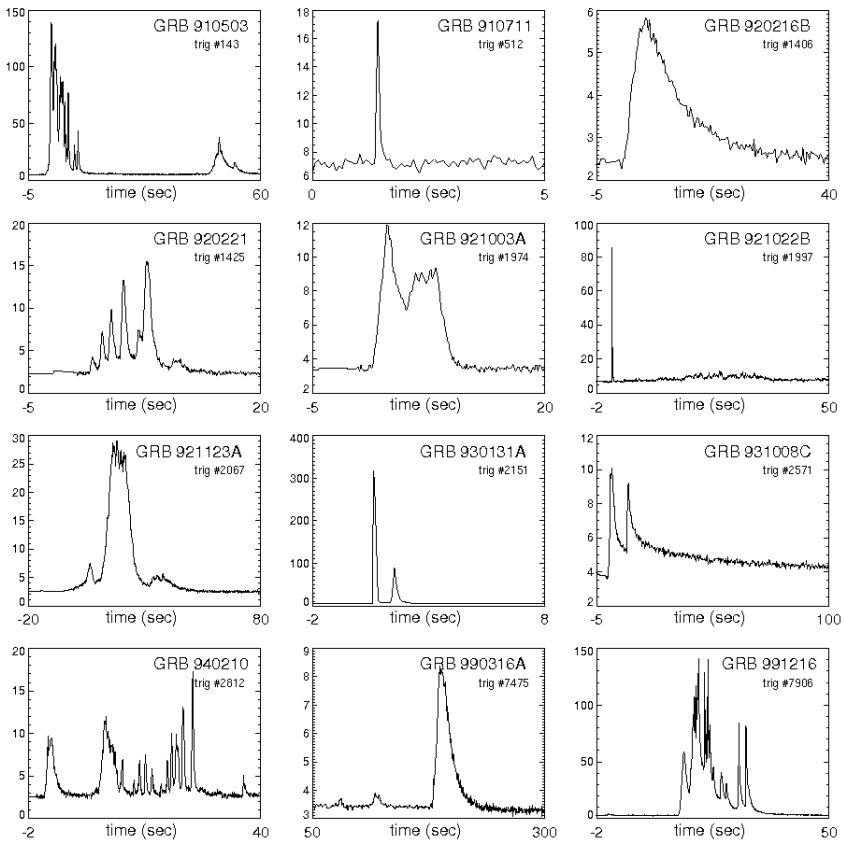

Figura 1.1: Examples of GRB light curves from BATSE from [27].

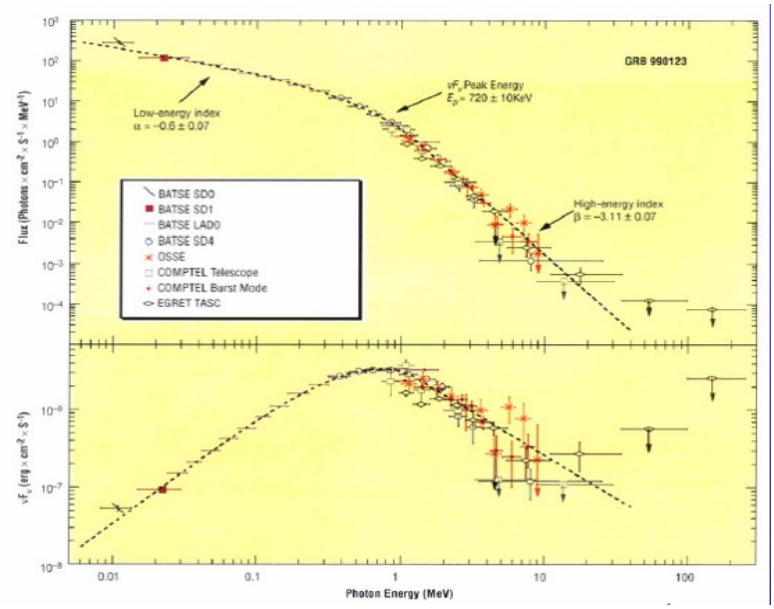

Figura 1.2: Typical photon (top) and νFν spectrum of GRB prompt emission modeled with the Band function [6], described in Sec. 2.1.

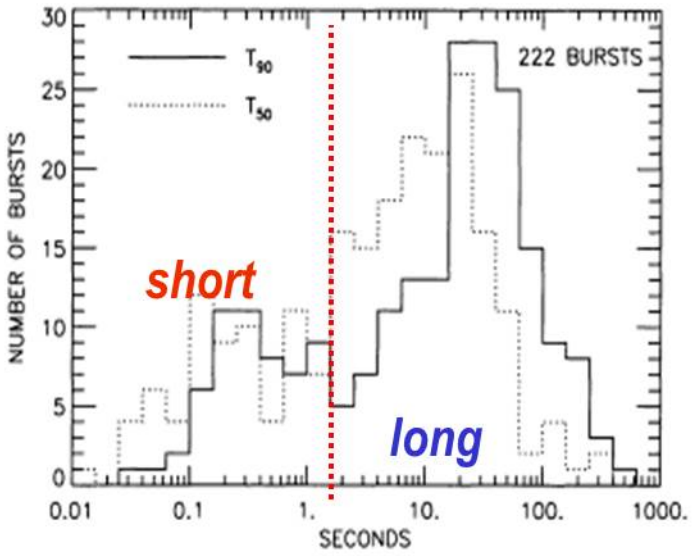

Figura 1.3: Bimodal distribution of GRBs detected by BATSE [57]. GRBs with a burst duration longer than 2 s are called long GRBs, otherwise they are called short GRBs.

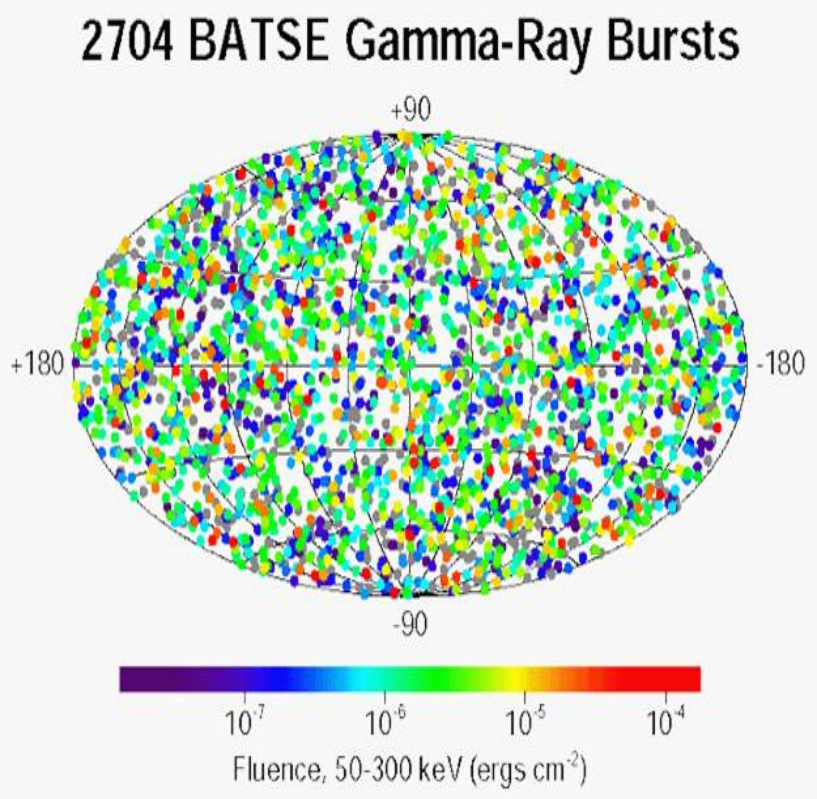

Figura 1.4: Distribution of GRB locations as measured from BATSE [76]; we can see that GRBs have an isotropic distribution.

ted by BATSE it was pointed out that GRBs could be distincted in two main types on the basis of their duration, i.e. long and short GRBs: bursts with duration less than 2 s are classified as short GRBs, and those which last for more than 2 s are called long GRBs [57]. As we can see in Figure 1.3, these two peaks in the GRBs duration distribution were a first hint of two physically different progenitors. BATSE also confirmed that GRBs have typically non-thermal spectra, which can be generally modeled with the smoothed broken–law proposed by Band et al. in 1993, i.e. the so called "BAND function, about which we talk later. Furthemore, thanks to Energetic Gamma Ray Experiment Telescope (EGRET), another instrument on board of CGRO, it was possible to detect for a few GRBs very high energy photons (i.e. from 30 MeV up to 18 GeV), which can last up to thousands of s after the GRB onset. Despite its burst location capability was limited to a few degrees at best, thus preventing a sensitive follow–up with focusing X–ray and optical/IR telescopes, this instrument provided evidence that the distribution of GRB directions in the sky is isotropic, as we can see in Figure 1.4, and it was suggested an extra–galactic origin for them [28]. Nevertheless, a Galactic (i.e., from a population of neutron stars distributed in a $\sim$100 kpc radius halo) or even local (Oort cloud) origin could not be excluded.

In 1997 a revolution in the GRB study happened thanks to the Italian-Dutch satellite BeppoSAX. It was the first X-ray mission with a scientific payload covering more than three decades of energy, from 0.1 to 300 keV, with a relatively large effective area, medium energy resolution and focusing capabilities in the range of 0.1-10 keV. The key feature of the BeppoSAX payload for GRB science was the co–alignment of two detectors of its Gamma–Ray Burst Monitor (GRBM), made of four CsI scintillators slabs of $\sim$1000 cm^2 each, with the two Wide Field Cameras (WFC), coded mask instruments based on position sensitive proportional counters operating in the 2–28 keV energy band with a source location accuracy of a few arcmin and a FOV of $\sim 40^\circ$. This combination made it possible to detect $\sim$15 GRBs per year with both instruments, to characterize their prompt emission down to the X–rays and to localize them with unprecedented accuracy, thus allowing follow–up observation with the on-board X-ray telescopes and transmitting the arcmin position to ground for follow–up with large optical, IR and radio telescopes. On 28th February 1997, by exploiting these capabilities, BeppoSAX, about 8 hours after the detection of the actual prompt emission, detected for the first time a rapidly fading X-ray/optical emission [15], the so called "afterglow. Afterglow emission was also detected in the optical, IR and radio thanks to

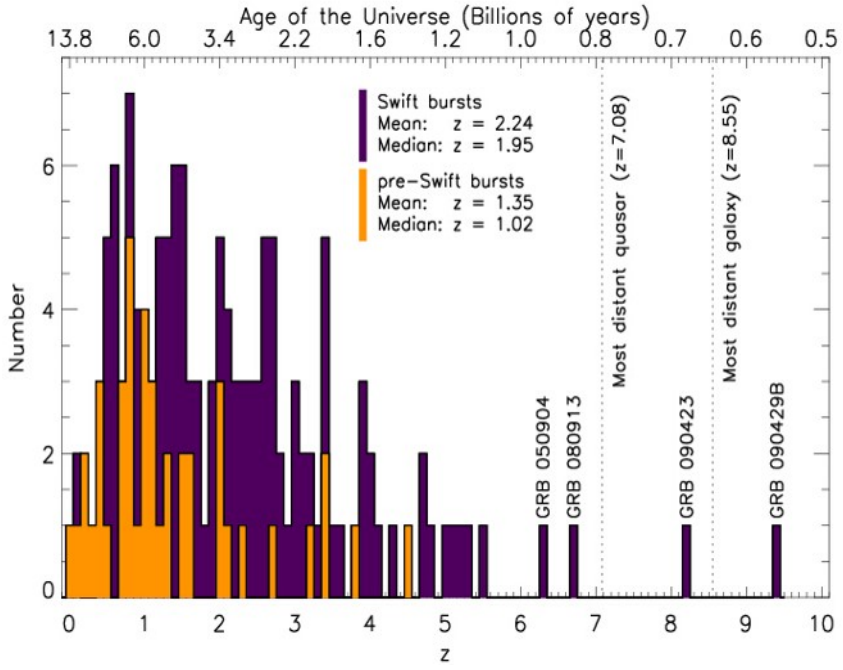

Figura 1.5: Distribution of GRB redshifts as of 2011. It peaks at $z \sim 1.95$ after Swift era [54].

follow–up observations of the GRB error box provided by BeppoSAX [102], [29]. The observations of this and subsequent events showed that afterglow lightcurves decay with time as a power law, with typical index ∼1.3, and have a power law spectrum with photon index around 2.
However, the main and immediate consequences of the afterglow discovery was that optical absorption spectroscopy allowed the first measurements of GRB redshift [77], showing that GRB redshifts are higher than 0.01 and up to 9, eventually confirming that they lie at cosmological distances (Fig 1.5 shows their redshift distribution), and their isotropic–equivalent radiated energy or luminosity spans several orders of magnitude and can be as huge as more than 10^{54} erg released in one minute or so.

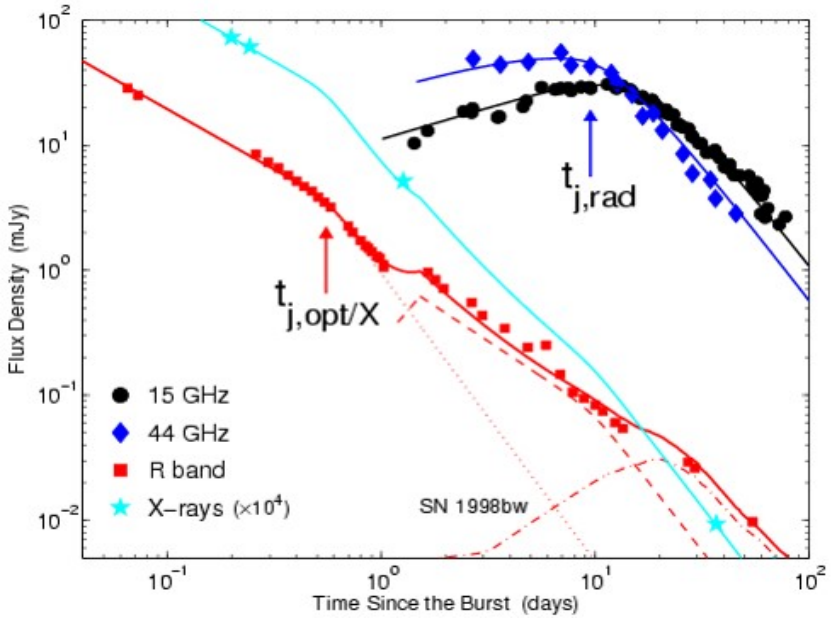

Figura 1.6: GRB-SN association: at the right bottom of the graph the SN bump in the optical afterglow light curve of GRB 030329 [34], [52]. $t_{j,rad}$ and $t_{Opt/X}$ are the time break typically observed in the lightcurve of the afterglow, due to the geometry of the jet, in the radio and Optical/X-ray band. In this figure we can see the flux of the afterglow detected in the optical/X-ray band and in the radio.

At the end of '90s another milestone discovery was made; indeed the normal GRB 980425 was detected and localized in temporal/spatial coincidence with a type Ib/c SN at z = 0.008 (SN1998bw) [34], [85]. A further evidence of a GRB/SN connection was later provided by bumps in optical afterglow

light curves of some of the lower redshift long GRBs, whose optical spectra resembled that of SN1998bw (Fig. 1.6), so it was pointed out that a sort of connection between SN and GRBs could be possible. Moreover, optical/NIR observations from the late '90s and early 00's started to provide information about host galaxies of GRBs.

The unique capabilities of BeppoSAX of detecting and measuring GRB prompt emission down to the X–rays allowed also to uncover the existence of a particular class of GRBs with only X-ray emission, the so called X-ray Flashes (XRFs); thus the distribution of spectral energy peaks has a long low tail. XRFs were deeply investigated in the early 00's by the HETE-2 (High Energy Transient Explorer) satellite, launched in 2000 and operating up to 2007 with accurate localization of few arcmin. The HETE–2 observations also confirmed and extended the correlation between spectral peak energy and radiated energy ($E_{p,i}$–E_{iso} or "Amati relation), discovered by Amati et al., 2002 [1], about which we discuss better below.

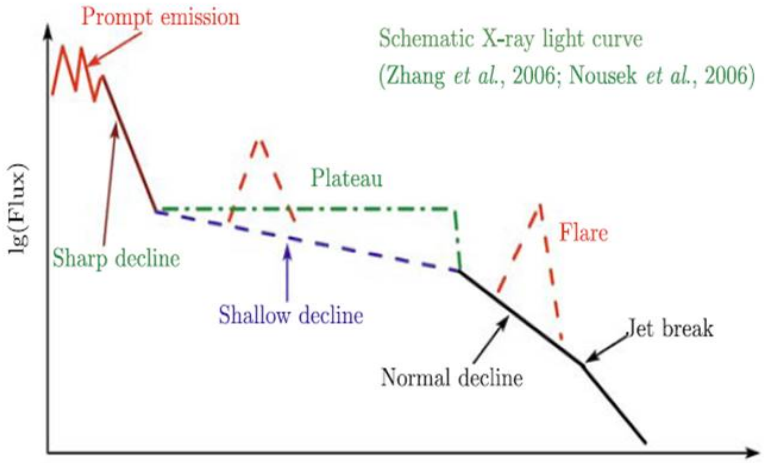

Figura 1.7: A canonical afterglow lightcurve, composed by four power-laws with different slopes, reconstructed thanks to Swift observations [112], [82].

Another major step forward in GRB science was allowed by the NASA mission dedicated to GRB studies Swift, launched in 2004 and still operative, which was developed and managed by a consortium including USA, Italy and UK. Swift has a great capability of a prompt localization within a few arcmins accuracy the GRBs detected by its BAT (Burst Alert Telescope), based on coded mask CZT detection system operating in 15–150 keV

energy band, which autonomously slews the whole satellite so to point its focusing X-ray Telescope (XRT) and UV-Optical Telescope (UVOT) to the burst position within 1–2 minutes. The main goals of Swift are the study of afterglow onset, the connection prompt-afterglow, and a substantial increase of counterparts detection at all wavelengths (and thus of redshift estimates) thanks to the very prompt dissemination of GRB position allowing immediate follow–up with optical/IR telescopes. Swift discovered the new and completely unpredicted phenomenology of the "early afterglow, consisting of a steep decay following the prompt emission, a subsequent "plateau or flat decay and flares superimposed to the plateau and the first part of the "late afterglow; an example of a schematical afterglow lightcurve is shown in the Fig. 1.7. Also, as expected, it allowed a substantial improvement in GRB redshift determination and characterization of multi–wavelength afterglow and host galaxies, including short GRBs. Other important discoveries include the evidence of a soft long tail in some short GRBs and the detection and characterization of sub–energetic GRBs (very weak GRBs) associated to SNe, like GRB 0602178. A further contribution to the observational picture is being provided since 2008 by the Fermi satellite, carrying a payload capable of detecting and studying GRBs from $\sim$10 keV (thanks to the GBM instrument, made of scintillators) up to the GeV energy range (thanks to the LAT pair conversion telescope), with dramatic improvement with respect to CGRO/EGRET. The huge radiated energy, the spectrum extending up to VHE without any excess or cut-off, an additional power-law component and time-delayed GeV photons of GRB 080916C measured by Fermi, are challenging evidences for GRB prompt emission models.

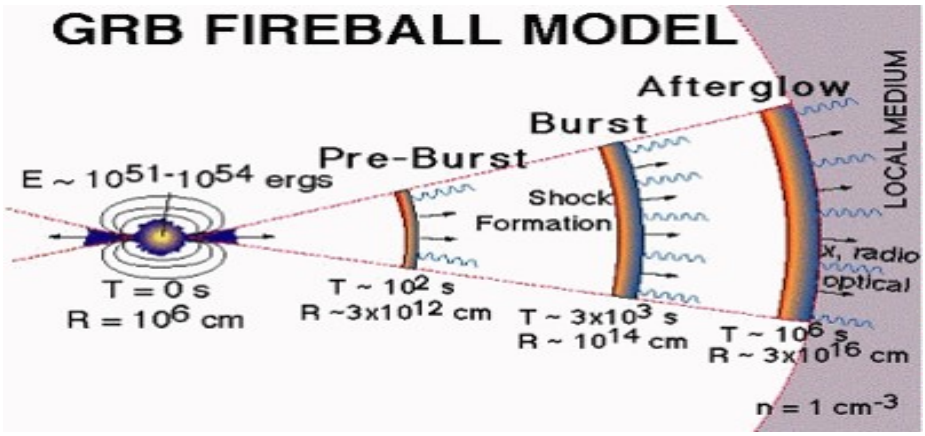

Figura 1.8: The standard kinetic energy dominated fireball for GRB emission. Here we can see the different phases of the GRB emission, as a function of the radius at which each one of them occurs, more specifically the burst or prompt emission generated by the internal shocks, then the afterglow emission produced by the external shock [47].

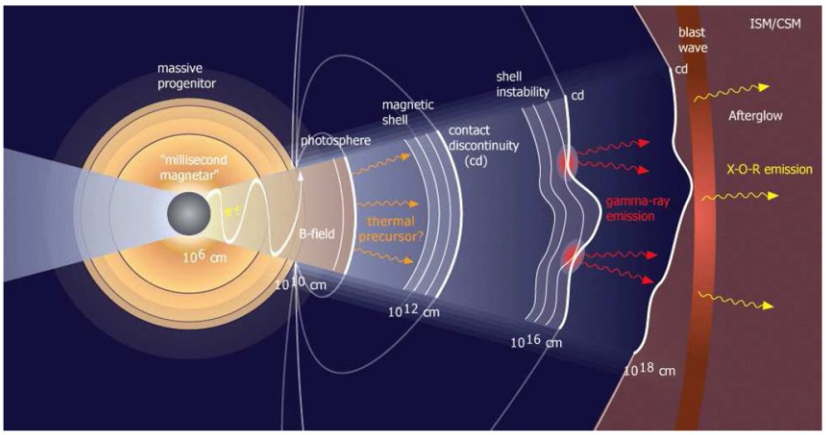

Figura 1.9: The magnetic (Poynting flux) energy-dominated fireball for GRB emission: the matter begins to radiate where the magnetic field reconnects (Lyutikov & Blandford, 2003).

1.2 Models for GRB emission and open issues

1.2.1 Physical scenarios

Many models have been proposed in order to explain the physics underlying in GRB phenomena. However, the physics of prompt emission is not settled yet. GRB lightcurves show a variability up to the order of ms, so this feature, together with their huge release of energy (some photons up to GeV energy have been detected), let us point out that probably we are observing a non-thermal radiation coming from a compact stationary source which should be very opaque; as such, we should not observe any radiation. Thus, a second hypothesis was pointed out, i.e. most likely we are observing an ultrarelativistic expanding plasma, hypothesis later confirmed by the direct calculation of the Lorentz factor Γ of the afterglow (about ~ 100), reducing the true variability with respect to the apparent one, thanks to the observations of scintillations at the radio wavelenghts. Then this expanding fireball becomes more and more transparent and it starts emitting soft photons when it reaches the so called photospheric radius; thus we observe the typical spectrum of a non-thermal emission process.
The basic scenario proposed for explaining the mechanism of prompt emission is the so called "fireball kinetic energy dominated model (Fig. 1.8), which advances the hypothesis that this plasma is polluted by a small fraction of baryons containing most of the kinetic energy, later converted, through the synchrotron emission, into radiation by internal shocks between different shells with different velocities. Then the fireball expands and collects interstellar matter (ISM). Once the relativistic energy of the collected matter becomes comparable to the relativistic energy of the shell itself, the fireball is decelerated (at about $\sim 10^{16}$ cm from the central explosion). Therefore a forward shock is produced, which propagates in the interstellar medium, always through synchrotron emission, the so-called external shock. The electrons accelerated in the internal shocks emit the photons responsible for the GRB prompt emission, observed from visible to gamma-rays. The emission coming from the electrons in the external shock produces the slowly fading transient visible for hours or even months from radio-band to X-rays, i.e. the afterglow.
We have two problems with this model: the first one is related to the low-

energy power-law index α, whose predictions deviate from the typical value $\alpha \sim -1$ revealed by the observations [87], [114], [81]. The traditional fast-cooling synchrotron model predicts an α value of -1.5 [95]. This has been regarded as a strong drawback of the traditional fast-cooling synchrotron model to interpret GRB prompt emission [46]. The second one is related to the low efficiency of conversion of kinetic energy into radiation by internal shocks, because the central engine should emit an extremely huge amount of energy, difficult to justify.
An explanation of the low observed value of α could be a different mechanism of emission, i.e. IC between electrons belonging to the forward shell and the photons emitted when the plasma becomes transparent.
Otherwise a second scenario was pointed out, involving the magnetic field; it is the so called "Poynting flux dominated model (Fig. 1.10) [118], according to which electrons are accelerated where the magnetic field is reconnected, so they still emit per synchrotron process. More specifically, highly magnetised spinning compact objects, e.g. millisecond pulsars or tori around black holes, are sources of Poynting flux that can power GRBs. They produce a plasma-loaded electromagnetic wind travelling outward and are fed by the rotational energy of the central object. In the wind of an aligned rotator the magnetic field is ordered and stationary. If ideal MHD applies, and the wind is radial in the poloidal plane, a large fraction of the total luminosity is bound to stay in form of Poynting flux. The picture changes in the case of an inclined rotator or any other source producing a non-axisymmetric rotating magnetic field. If the emitted Poynting flux contains modulations of the field it also carries along free magnetic energy, which can be extracted by reconnection processes. In these processes the field rearranges itself to a energetically preferred configuration while the energy released is transferred to the matter. Because perfect alignment of magnetic and rotation axis is a special case it is likely that most astrophysical objects produce modulated Poynting fluxes containing free magnetic energy. A necessary condition for the existence of free magnetic energy in the flow is the field variation on small scales. For reconnection processes differently oriented field lines must come close to each other. Therefore the length scale on which the orientation of magnetic field lines change controls the speed of the field dissipation. The smaller the length scale is the faster the field can decay.
Other models suggest that the non-thermal spectrum observed is the result of the sum of many thermal spectra or of a their deformation. These models are the so called innermost models.

Finally, we expect a thermal component in the spectrum of the prompt although it has not been observed yet.

1.2.2 Open issues in the GRB research field

There are a lot of open issues related to the understanding and the explanation of GRB physics and their geometry, which have to be still settled. The main open issues are:

- **GRB prompt physics emission**: the fireball scenario (baryon kinetic energy or Poynting flux dominated) and bulk Lorentz factor Γ are still to be firmly established; indeed we have already said that internal shocks in fireball scenario cannot be so efficient in converting the kinetic energy into radiation and often we obtain value of α different from that one expected.

- **Swift's discovery related to the so called flares**: X-ray fluxes, of duration of minutes to hours [11], [14], [74], are maybe due to the inhomogeneity in the circumstellar medium. Probably the central engine works in a period much longer than the burst duration [11], [112], [23], [62].

- **GRB-SN connection**: it is still unknown if all long GRBs are produced by SN Ic/b and especially what are the properties and peculiarities of these kind of SN.

- **The early afterglow phenomenology**: we have not settled yet the physical mechanisms underlying afterglow emission.

- **The classification and understanding of particular subclasses of GRBs**: e.g., sub-energetic GRBs have to be still well understood; the most common explanations for the apparent sub-energetic nature assume that they are normal events seen very off-axis [106], [90]. Another subcategory of massive stars GRBs is formed by the so called ultralong GRBs [36], [64]. Probably they are associated with a blue supergiant progenitor, and they have a duration of about $10^3 - 10^4 s$. Moreover it has been pointed out that these objects are the tail of normal GRBs.

- **The lack of jet breaks or to the observation of a chromatic break**: indeed if we assume an emission collimated in an opening angle jet, we have seen a chromatic break in several Swift X-ray afterglow lightcurves of some GRBs, or even no achromatic break at all; we expect to see a dropout of the brightness in the lightcurve of the afterglow as geometrical effect of the collimated emission. Thus, we cannot well estimate the value of the assumed opening jet angle. Probably the cause may be that we are observing poorly collimated GRBs or with a very high energy budget.

- **Polarization**: indeed until 2010, no secure detection of polarization of prompt emission has been detected and very recently measurements of $10 - 30\%$ of polarization has been observed by GAP (Gamma ray burst polarimeter) for few GRBs; radiation from synchrotron and IC is polarized, but a high degree of polarization can be detected only if magnetic field is uniform and perpendicular to the line of sight, instead small degree of polarization is detectable if magnetic field is random, emission is collimated (jet) and we are observing only a (particular) portion of the jet or its edge. Recently a high degree ($\sim 30\%$) of polarization with stable angle of early optical afterglow of GRB120308A has been reported and this could be an evidence of magnetized baryonic jets with large-scale uniform fields that can survive long after the initial explosion.

- **Central engine involved in GRB phenomenon**: not only the nature and the physics of prompt emission are still unresolved, but also the emission mechanism of energy extraction and its efficiency.
  There are two main models for explaining the central engine question: the first one involves a BH (about with mass $\sim 1 M_{\odot}$) accreting matter, which converts its gravitational energy into neutrinos decaying into electrons and pair of electrons and positrons; this mechanism of extraction could be explained by the so called "Blandford-Znajek process [9].
  The second model involves a supermassive rapidly spinning neutron star, which converts rotational energy into radiation through the magnetic field [117].

1.2.3 Classification of GRBs

By defining the hardness ratio (HR) of a burst as the fluence in the energy range 100 – 300 keV divided by the fluence in the energy range 50 – 100 keV, we can say that in the duration-hardness T_{90} - HR plane (where T_{90} is the time over which a burst emits about 90% of its total measured counts), two different classes of GRBs have been identified: long/soft vs short/hard [56]. The distinction is not very sharp, but the separation limit considered is about 2 seconds in the BATSE band (30 keV-2 MeV). Long and short GRBs stand respectively for 3/4 and 1/4 of the total collection of BATSE sample of these objects. A little note has to be clearified: the definition of T_{90} depends on the energy band and sensitivity of the detector, indeed a same burst may have a longer T_{90} if the detector is more sensitive or has a softer energy band.
Thanks to the follow up of some telescopes, e.g. BeppoSAX, Swift, HETE2, it has been pointed out that the main two categories of GRBs must be originated from different objects.
Indeed, long GRBs are associated with Supernovae Type Ic produced by the core collapse of a massive star, whose hydrogen and helium envelopes have been removed before the explosion (Fig. 1.10)(e.g. [34]; [52]; [97]; [12]; [86]). It is not consequent that all SNe Ic have a GRB associated (only 3% are

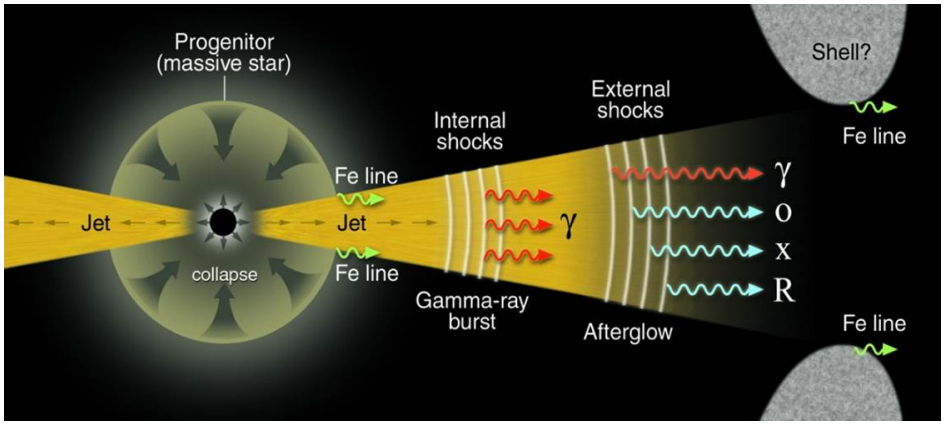

Figura 1.10: Standard scenario for the origin of long GRBs. As we can see, long GRBs may been generated by a supermassive star collapsing into a black hole. We can notice the formation of the internal shocks producing the prompt emission detectable in Gamma energy band, and the external ones generating the afterglow radiation detectable from X-ray to radio energy band.

associated with a GRB), but those associated are broad-lined SNe (i.e. SN

showing broad absorption lines) and they appear to represent the brightest end of the normal Ic population. The exact type of massive star is not yet clear, probably it is a star with mass larger than $10M_{\odot}$, collapsing to a black hole, i.e. the so called "collapsar model [105], [73]. Also alternative candidates are probable, such as binary stars or magnetar central engine. They generally lie in blue, regular and high star forming galaxies, and this fact confirms the link between long GRBs and dead massive stars [105]. Moreover, they are located especially in star forming regions, with a metal rich circumburst environment. Their age is estimated to be < 0.2 Gyr, significantly younger than the minimum age estimated for the short early type host galaxies of SGRBs (short ones). As we have already said, an open issue is related to the connection of long GRBs with SN; indeed we do not know if all long GRBs are produced by a type Ibc SN progenitor, or which fraction of type Ibc SN produces a GRB, and what are their peculiarities and what are the properties (e.g., energetics) of the GRB linked to those of the SN and, finally, the existence of long GRBs with no (or very faint) associated SNe.
Short GRBs, conversely, have no association with a SN, no preferred type of host galaxy and a clean circumburst environment. For a long time it has been thought that these objects arise from compact object binary mergers of compact objects in binary sistems (merger of two neutron stars or a neutron star and a black hole, see Fig. 1.11), being less energetic ($\leq 10^{52}$ erg), with lower redshifts ($z \leq 1$), and being generally placed in regions of old stellar population.
The study of short GRBs is more challenging, however, because their explicit progenitors type have not been identifed yet. Short GRBs are observed in the whole electromagnetic spectrum. Moreover, they have relatively more high energy γ rays than long bursts have [63]. Their peak photon energies E_p are generally found in a range spread from 500 keV to several MeV, with E_p which softens and decreases with time. As the long ones, SGRBs have a wide range of profiles, from smooth to variable profiles with many peaks.
As we have already said, SGRBs are associated with an older and lower redshift galactic population than the long ones, with large projected offsets from the centre of their host galaxies. The absence of Hα and [OII] emission in their host galaxies constrains the star formation rate to $< 0.2M_{\odot}yr^{-1}$, while for long GRBs the star formation rate is $\sim 1 - 10M_{\odot}yr^{-1}$. Also the lack of Balmer absorption lines demonstrates that the last significant star formation event happened $> 1Gyr$. SGRBs sources involve energies larger than $\sim 10^{50}erg$, and the size of the engine of this activity is extremely compact, as

we can argue by its rapid variability of the radiation flux. Probably the mass can be converted into energy with a few percent of efficiency, in this way SGRBs must process with a mass up to $10^{-3}M_{\odot}$ through a region smaller or equal to a neutron star or a black hole.
Finally we have also the so called X-Ray Flashes, about which we have already discussed. The challenge is now how to distinguish types of GRBs based on data.
Zhang et al., 2009 [113] proposed a list of multiwavelenght observational criteria, related to the physical nature of GRB, e.g. its position in the host galaxy, SN association. However, multiwavelength data cannot be immediately provided, so it is necessary to analyze GRBs data directly from the Gamma ray ones.

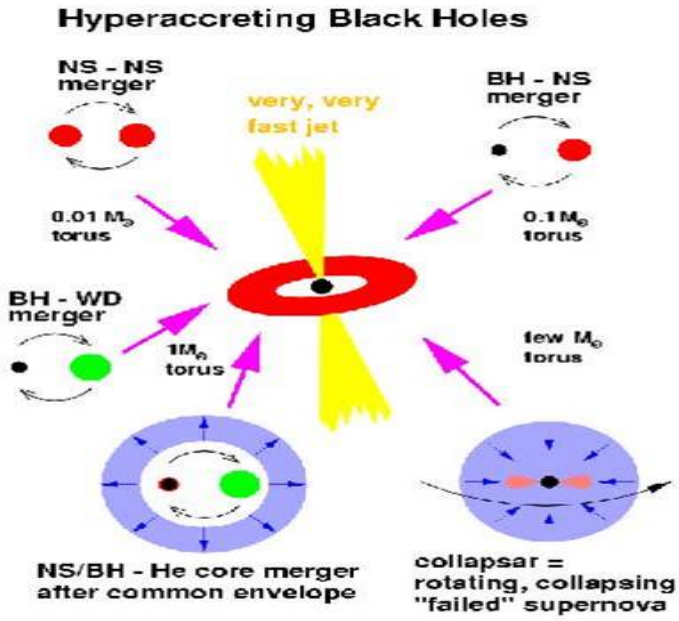

Figura 1.11: Standard scenario for the origin of short GRBs. They may have been generated by the merging of two neutron stars or a neutron star and a black hole.

1.3 GRB in the cosmological context

There are many of probes that support the hypothesis that the present Universe is flat and it is in undergoing accelerated expansion, for example the Hubble diagram of Type Ia supernovae, observed at the end of '90s.
In this scenario the baryonic matter constitutes only a limited part of the total matter density (only 4-5%); the 28% is constituted by the so called Dark Matter which does not emit in the electromagnetic spectrum, but it causes gravitational effects. The remaining part, i.e. about 70%, the dominant part of the Universe matter, is composed by the so called Dark Energy, that propels the acceleration.

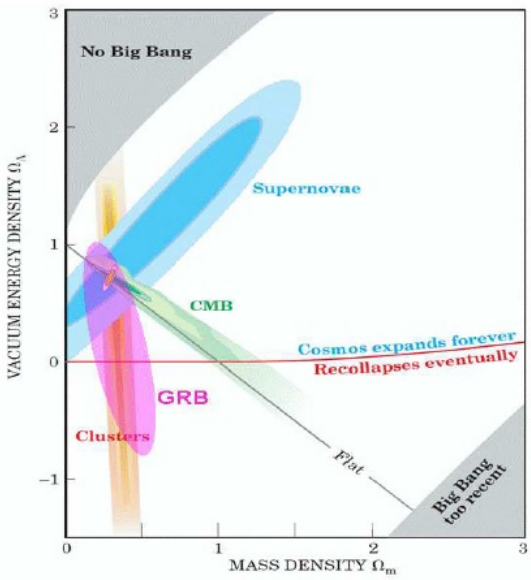

Figura 1.12: Data from different cosmological probes (SNe–Ia, BAO, clusters) in sinergy with CMB measurements provide us with evidence that the Universe is flat and the matter (ordinary plus dark) plus ordinary energy density is 30% of the total [4].

This picture is the result of combined observations of Supernovae Ia (SNe Ia) at high redshift, CMB (*Cosmic Microwave Background*), galaxy clusters and baryonic acoustic oscillations (BAO). Anyway, each of these probes is affected by different systematics, that can bias the value of cosmological parameters.
In order to improve the constraints on the cosmological parameters, it is possible to cross check the different results, thus minimizing the effect of the

systematics of each probe. As we can see in Fig. 1.12, GRBs can constrain cosmological parameters consistently with the others probes.
Some results have identified the Dark Energy with the so called Cosmological Constant, but there are mainly three different groups which involve Dark Energy: 1) the aforementioned "Non zero cosmological constant if $w = -1$, 2) a potential energy of some not yet discovered scalar field, 3) effects connected with inhomogeneous distribution of matter.
It is of relevant importance noting that the sensitivity of Equation of State (EoS) of dark energy increases significantly with the redshift, and it becomes very high since $z \geq 2$, having fixed a flat Λ cold dark matter model. So it is important to investigate, especially at high redshift, the presence of dark energy.
In this scenario GRBs can be of great importance, thanks to their higher redshifts than SN Ia. Indeed, given their redshift distribution extending at least to $z \sim 9$ and high luminosity (mostly emitted in the X-ray and Gamma-rays) and their association with explosive death of massive stars and star forming regions, GRBs are unique and powerful tools for investigating the early Universe, up to the re-ionization era (the first billion years of the Universe), by shedding light on reionization, first stars (stars of POP III), and by tracing the cosmic chemical evolution at early times (see Fig. 1.13).

In fact, since it has been pointed out that long GRBs are produced by massive stars, they can track star fomation, and in particular the population of UV-bright stars, responsible for the bulk of ionizing radiation production. By counting the distribution of GRBs N(z) and accounting for the observational selection function, we can trace the global star formation rate density as a function of cosmic time. This value can be extrapolated also thanks to observation of galaxies with $z > 7$ found in Hubble Space Telescope (HST) deep fields, even with some uncertainties such as completeness and cleaness of photometric redshift samples at those redshifts and the poorly constrained form of the galaxy luminosity function at stellar masses $< 10^8\ M_{\odot}$. It is a problem because star formation could result in fainter galaxies too, as simulations suggest [68].
Moreover, GRBs can provide a valid alternative to find the Lyman continuum escape fraction, whose question remains still to be solved, since it cannot be determined directly at high redshifts, especially for small galaxies, responsible for the bulk of star formation; lower redshifts studies have found too low values of f_{esc} unable to drive reionization. Indeed, GRBs have a high S/N of afterglow, which reveals the neutral hydrogen column along our line-of-sight

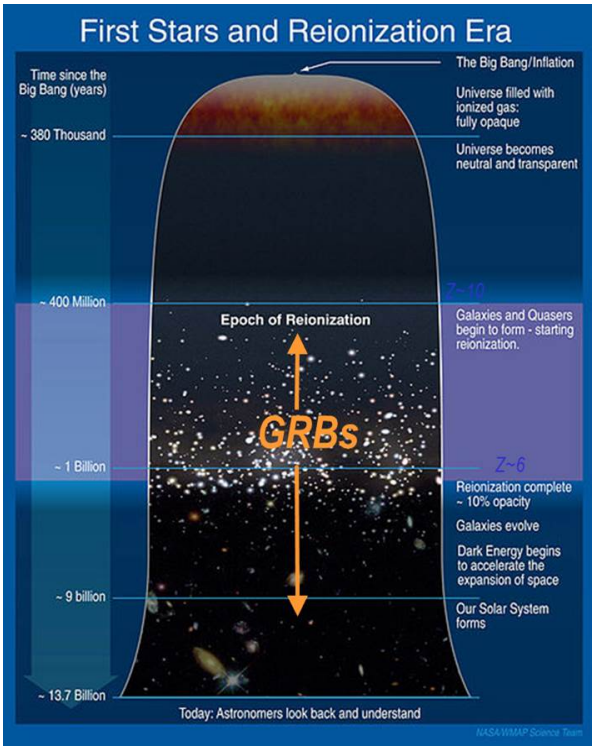

Figura 1.13: GRBs in the cosmological context. They are linked to the so called "dark ages, as we can see in this figure.

to the GRBs, so we can infer the opacity of the medium and a sizeable sample of afterglows can be used to infer the average escape fraction over many lines of sight. Moreover, besides the quantity of hydrogen column, we can observe also the quantity of H_2 molecular absorption, thus we can monitor the cosmic metal enrichment and chemical evolution up to early times.
Furthermore, it has been argued that the POP-III stars may produce collapsar-like jetted explosions, which are of longer duration than typical long GRBs. However, this link with this type of stars is just a supposition and it has to be confirmed.
In this context, thanks to GRBs and their host galaxies, we can find alternative paths for solving these key-questions.
There is also an other approach to use GRBs for cosmological studies, which involves the use of GRBs correlations in order to constrain some cosmological parameters such as Ω_M and Ω_Λ indipendently of other methods, like the Cosmic Microwave Background, SNIa or BAO, and in this way it is possible to study the properties and the evolution of dark energy.
This work have been done in this thesis.

However, GRBs are not standard candles, because of their wide range of luminosities. Recently, several attempts to standardize them have been made in order to use them as cosmological probes, by using some correlations such as, for example, the so called "Amati relation.
Unfortunately, the use of these correlations is limited, due to the lack of low-redshift GRBs, so they cannot be directly calibrated. Particular statistical methodologies need to be adopted in order to avoid the circularity problem in the construction of GRB Hubble diagram.

1.4 E_p - Intensity correlations

The use of correlations (such as the Amati relation) is useful to constrain some cosmological parameters, by contributing in this way to reinforce the settlement of cosmology.
GRBs spectra are non-thermal type, and they can be empirically fit with the so called Band model, i.e. a smoothly broken power law, whose parameters are the low-energy spectral index α, the high-energy one β, and the break energy E_0.
Their νFν spectra show a peak which corresponds to E_p=$(2 + \alpha)$, whose

intrinsic value is $E_{p,i} = (1+z)E_p$, measured thanks to the discovery of the optical counterpart of GRBs. The distribution of $E_{p,i}$ for GRBs with measured redshift is approximately a Gaussian centered at few hundreds keV, with a low energy tail, corresponding to the so called X-ray Flashes.

We can also define the isotropic equivalent radiated energy obtained integrating the spectrum in the range 10 keV–10 MeV

$$E_{iso} = 4\pi d_L^2(z, \Omega_M, \Omega_\Lambda)(1+z)^{-1} \int_{1/(1+z)}^{10^4/(1+z)} EN(E)dE \tag{1.1}$$

where N(E) is the Band function:

$$N(E) = \begin{cases} A(\frac{E}{100keV})^\alpha exp(\frac{-E}{E_0}), & (\alpha-\beta)E_0 \geq 0 \\ A(\frac{E(\alpha-\beta)}{100keV})^{(\alpha-\beta)} exp(\alpha-\beta)(\frac{E}{100keV})^\beta, & (\alpha-\beta)E_0 \leq E \end{cases} \tag{1.2}$$

The distribution of E_{iso} has an energy range starting from 10^{51-54} erg, with a peak at 10^{53} erg.
In this work we try to constrain the cosmological parameters from the E_p - E_{iso} correlation, known as Amati correlation.
In 2002 thanks to BeppoSAX data about a small quantify of GRBs (about 12 GRBs) with known redshift and spectral parameters, it was discovered that these two parameters are correlated. This correlation is called "Amati relation (Fig. 1.14) and it has the form

$$logE_{p,i}(keV) = m \cdot log(\frac{E_{iso}}{10^{52}erg}) + q \tag{1.3}$$

with $m \sim 0.5$ and $q \sim 2$. Moreover, they have extended the sample of GRBs by including also other GRBs detected by different satellites with different sensitivities, and they noticed that the normalization varies only marginally in this case, as we can see in Fig. 1.15.
Moreover, this correlation can be used for distinguishing different classes of GRBs, thus shedding light on their different physical nature. In fact, the long ones follow very well the correlation, while the short ones do not follow it, so they may have a different emission mechanism than the long ones.
The correlation is also characterized by another parameter, i.e. an extra Poissonian scatter, the so called "extrinsic scatter, distributed around the value of ~ 0.2 dex around the best fit law, usually quantified by performing a maximum likelihood analysis. This scatter quantifies the dispersion of the

correlation and is due to the uncertainty on the cosmology and the distribution of the values of the jet opening angle.
There are many different intensity indicators that we can use instead of E_{iso}. Indeed, the correlation holds also when substituting E_{iso} with L_{iso} (e.g., [59])

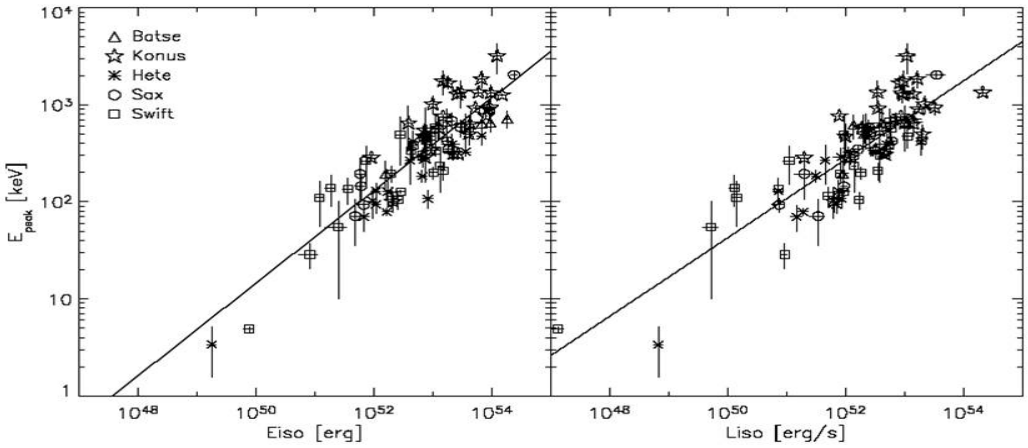

Figura 1.14: The "Amati relation, or, more in general, the $E_{p,i}$ – "intensity correlation holds also when substituting the radiated energy with the L_{iso} [80].

or L_{peak}, which is the luminosity related to the peak of the GRB spectrum [108], [40].
This is expected because L_{iso} and L_{peak} are strongly correlated with E_{iso}; compared to E_{iso}, $L_{peak,iso}$ is subject to more uncertainties (e.g., light curves peak at different times in different energy bands; spectral parameters at peak are difficult to estimate).
All these quantities can be computed either in a range of energies (usually 10 keV - 10 MeV) in the source restframe, or at a monochromatic range (e.g., at the peak of the spectrum).
The correlation $E_{p,i}$ - E_{iso} remains the least scattered, maybe due to the fact that it accounts for the brightest part of GRBs which mainly contribute to the E_p of the time averaged spectrum. It does not occur with $L_{iso,T90}$ (the isotropic luminosity averaged over the T_{90} duration), which is affected by the assumption that all the time bins of GRBs contribute equally to the average $E_{p,i}$.
Hence, we can use GRBs as distance indicators, indeed the total radiated

energy can be calculated from the bolometric fluence S_{bol}, in this way:

$$E_{iso} = 4\pi d_L^2(z, \Omega_M, \Omega_\Lambda) S_{bol}(1+z)^{-1} \tag{1.4}$$

where d_L is the luminosity distance and S_{bol} is the bolometric fluence. In order to use GRBs as standard candles, it is necessary to calibrate the correlation.
$E_{p,i}$ is the key parameter in GRB models; indeed if we consider valid the simple synchrotron model emission of fast cooling, we can relate $E_{p,i}$ with the frequency at which electrons have the minimum Lorentz factor; alternatively, if we keep in consideration the Tavani's synchrotron model [98], we can link $E_{p,i}$ to kT_e, where T_e is the electrons temperature, similarly in the case if IC is the emission process which occurs in GRB prompt emission, or if we consider valid the innermost models [118].
The most surprising thing is that the Amati correlation, as well as in the whole burst duration, holds strongly in each interval of the same burst. This is referred to as time-resolved analysis, and this thesis work is focused on the investigation of the aforementioned correlation in GRBs physics. One

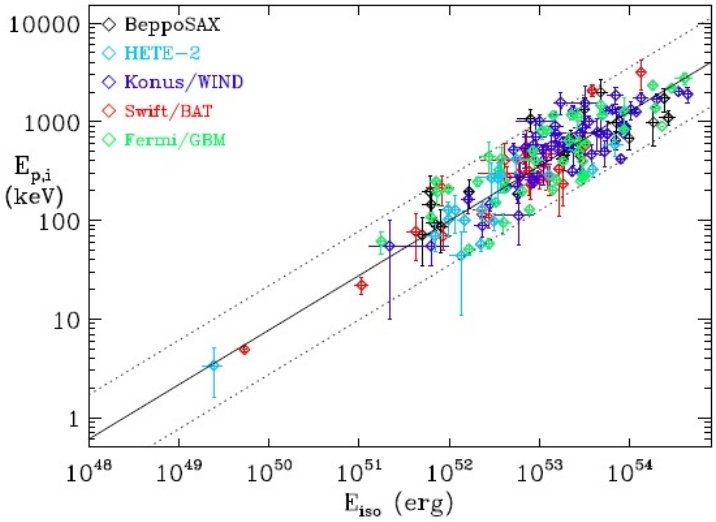

Figura 1.15: $E_{p,i}$ - E_{iso} correlation in long GRBs obtained by the telescopes reported in the top-left part of the figure [4].

of the main problems of these correlations is the lack of low-redshift GRBs (i.e. with $z \ll 1$), in order to make a cosmology indipendent calibration,

such as with SNIa. Nonetheless, this question can be resolved by analyzing a subsample of GRBs with similar redshifts.

1.5 Standardizing GRBs through E_p-Intensity correlations

The idea to use GRBs as standard candles came out in 2004, when it was found that, by substituting E_{iso} with the collimation-corrected radiated energy $E_\gamma = E_{iso}(1 - cos\theta_{jet})$, i.e. by assuming an emission collimated in a jet with an opening jet angle θ_{jet}, the relation steepens. This result was pointed

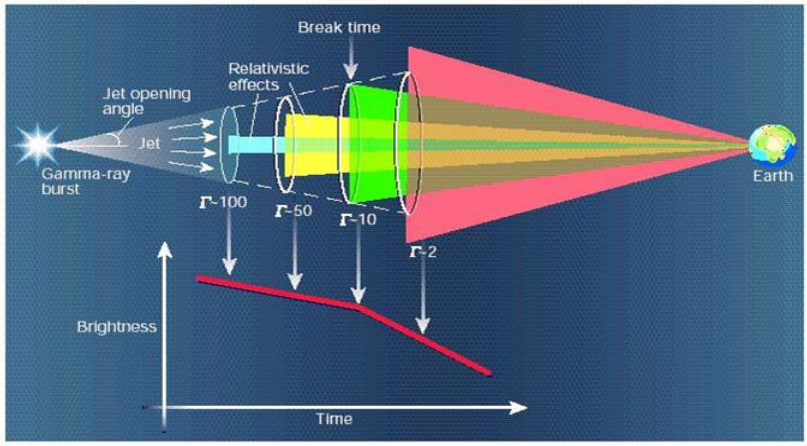

Figura 1.16: Inferring GRB jet opening angle from the late break in the optical light curve: as the plasma decelerates, the relativistic beaming angle to the observer increases; when it exceeds the physical jet opening angle, a sudden decrease of the emission is observed.

out only for a small sample of GRBs with known $E_{p,i}$ and E_{iso}, for which it was possible to infer the jet opening angle from the break time t_b, at which the decay of the light curve of the optical afterglow becomes steeper (Fig. 1.16).
Thus, by using the low scatter of this correlation and appropriate statistical methods accounting for the lack of calibration, within the standard Friedman-Lemaitre-Robertson-Walker (FLRW) cosmological method, it was possible to infer estimates of Ω_M and Ω_Λ, consistent with to those derived

from SNIa and the CMB. However, in many cases, the time-break decay is not detected, so in the last years the use of this correlation was questioned, because model dependent.
The use of $E_{p,i}$-E_{iso} correlation is preferable for two main reasons: firstly, this correlation is model independent, because we do not have to assume any jet or afterglow model, or any density profile of circumburst environment, or efficiency of conversion of fireball kinetic energy into radiated energy; secondly, we can exploit a larger sample of GRBs, because we need only two parameters, directly observable.

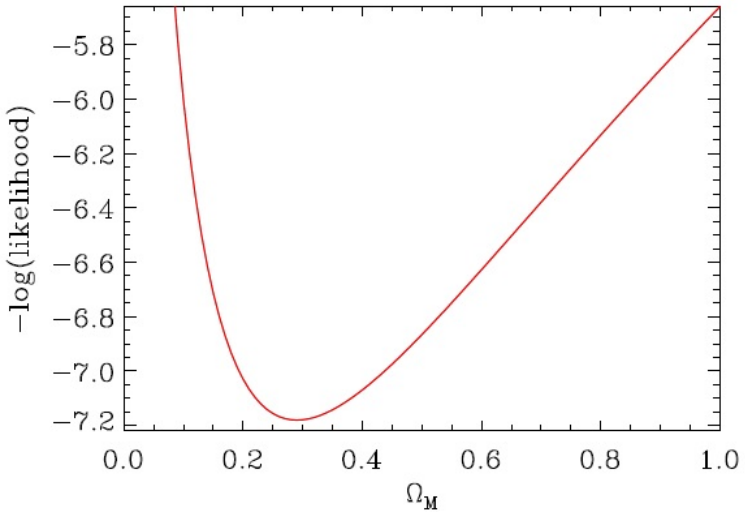

Figura 1.17: Normalized -log(likelihood) of $E_{p,i}$-E_{iso} correlation, in function of Ω_M used to compute the E_{iso} values in a FLRW Universe from Ama ti et al. 2013. We can see that the "best value of Ω_M is that one which minimizes the $-log(likelihood)$ function, i.e. 0.3.

However, there is another problem, the so called, "circularity problem. In order to estimate Ω_M, we need to know the Ω_M value for inferring the luminosity distance value, and then E_{iso}. Thus we can circumvent this problem in this way: we can fit simultaneosuly both the parameters of the correlation with the cosmological ones and by assuming that the dispersion of $E_{p,i}$-E_{iso} relation will minimize for the "correct value of Ω_M, by making it float between 1 and 0 and by assuming a flat universe; so the χ^2 value obtained by fitting the Amati correlation with a power law is function of Ω_M assumed in the computation of E_{iso}.
Since the extra Poissonian scatter of the relation, the χ^2 statistics is not

reliable, because it does not assure confidence levels for both the parameters of the fit (slope and normalization). So, Amati et al. (2008) [3] decided to adopt a maximum likelihood statistical method, which accounts for both the X and Y parameters uncertainties and for the extra variance σ_{ext}. The value of the likelihood is provided by the so called Reichardt function, a linear function, which can provide also the value of the dispersion of the correlation (besides the slope and the normalization of the correlation). Its expression is:

$$L(m, c, \sigma_{ext}, x, y) = \frac{1}{2}\sum log(\sigma_v^2 + \sigma_{y_i}^2 + m^2\sigma_{x_i}^2) + \frac{1}{2}\sum \frac{(y_i - mx_i - c)^2}{\sigma_v^2 + \sigma_{y_i}^2 + m^2\sigma_{x_i}^2} \tag{1.5}$$

where m is the slope and c the constant of normalization.
Thus, for a time-integrated analysis, the $-log(likelihood)$ graph shows a parabolic shape whose minimum is for $\Omega_M = 0.3$ (Fig. 1.17). This result is very reassuring, because we can say that GRBs provide evidence, indipendently of SNIa, that Ω_M is smaller than 1 and about 0.3.
Thanks to Amati et al. who used the Reichardt likelihood function, which has the advantage of not requiring the choice of an arbitrary variable between $E_{p,i}$ and E_{iso}, we can note that, by increasing the number of GRBs samples, the accuracy of Ω_M improves, although the latter one is still lower than that obtained thanks to SNIa.
Thus it is clear that the contribution of X-ray telescopes such as Konus-WIND, Swift and Fermi/GBM and other future missions, joint together, could enlarge GRB samples, up to 15-20 GRBs/year. Indeed thanks to some simulations, made via Monte Carlo techniques, taking account for such missions as Chinese-French mission SVOM, or e.g. the Japanese-CALET/GBM experiment for the ISS, we know that with a sample of 250 GRBs we can reach the same level of accuracy for Ω_M of SNIa.
Finally, there are many different approaches in order to extent GRBs samples and to calibrate the Amati relation up to lower redshifts, e.g. by using the correlation luminosity distance vs redshift inferred from SNIa, or by crossing different correlations, or by self-calibrating the correlation with a large number of GRBs lying within a narrow range of z.

My thesis project is focused on the investigation of the time-resolved E_p–Flux correlation, whose goal is to use a larger sample of GRBs (by including also those with unknown redshifts), in order to perform a model and

cosmology-independent calibration of the slope and the scatter of this correlation, thus improving the estimates of cosmological parameters. These results could provide relevant inputs for models of prompt emission physics and for cosmology.

Capitolo 2

Investigating the time resolved E_p - "Intensity correlation

2.1 Time resolved E_p - Intensity correlation in GRBs

GRBs show a clear spectral evolution even at time scale much lower than one second, i.e. their parameters change as a function of the time. In particular, in most GRBs we can observe a correlation between E_p and the flux (detected by BATSE in the energy range 20 keV – 2000 keV by Liang et al. (2004) [66], and detected by KONUS WIND in the energy range of 15 keV – 1500 keV by Golenetsky et al. (1983) [48]). Recently, this evidence has gained more and more importance in the correlations context, on the basis of averaged (E_p – L_p correlation) or time integrated spectra (E_p – E_{iso} correlation). Thanks to time resolved analysis of BeppoSAX and Fermi GRBs with known redshift, it has been found that different time intervals of different GRBs follow the same E_p – luminosity correlation (e.g., [72], [32]). This discovery has provided further support to the reliability of E_p - "Intensity (e.g., E_{iso}, L_p) correlation based on averaged spectra, and also an explanation about its physical origin.
Since these intervals are quite similar to emission timescales, the analysis of these types of correlations allows us to obtain better constraints on the physics underlying prompt emission; as it will be discussed in this thesis work, this GRB study can allow an improvement of the cosmological parameters estimates. Fig. 2.1 shows an example of time-resolved analysis, where each

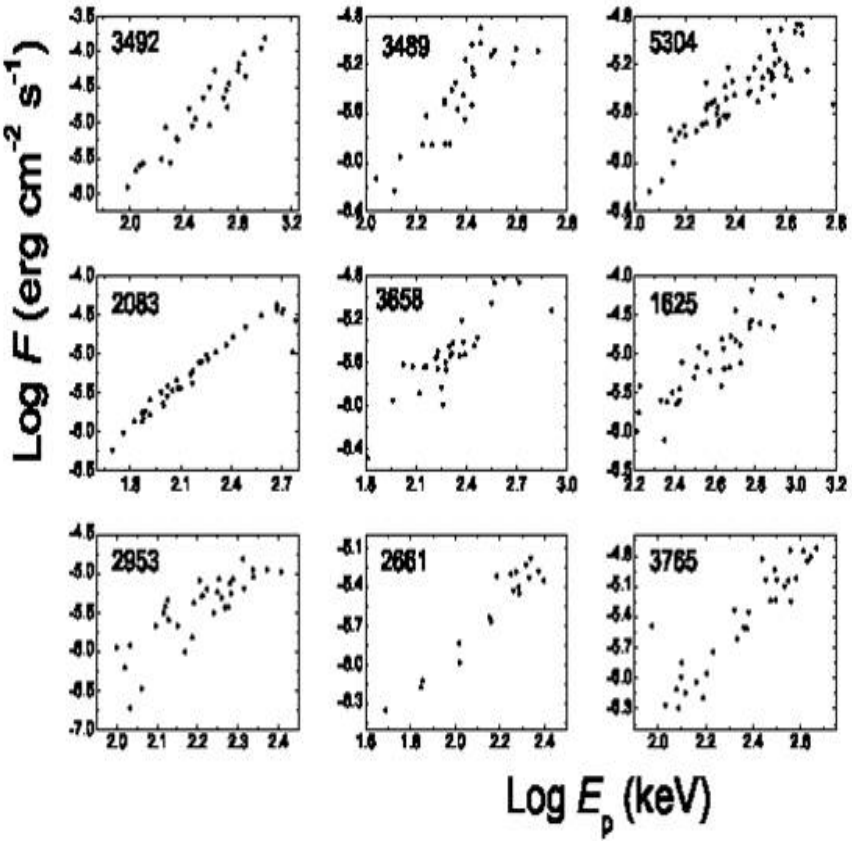

Figura 2.1: E_p – Flux correlation for BATSE GRBs, as investigated by Liang et al. (2004) [66]. Each plot refers to a single time interval in the burst of the same GRB.

figure is related to a different GRB, and each point represents a single time interval in the same GRB. Currently, time resolved spectra have been fitted using semi-empirical functions, with no direct physical motivation.

The most adopted models to fit GRBs spectra are the so called Band function (see section 1.1), a smoothly broken power law and a cut off power law. The BAND function is a model in which a power law with high-energy exponential cutoff and a high-energy power law are joined together by a smooth transition (see Fig. 1.2). It is an empirical function proposed by Band et al. (1993) [6], which fits most of the observed GRB spectra. It is only empirical, so it has not a direct physical motivation; there have been many attempts to give it a physical meaning, e.g. by incorporating fast-cooling synchrotron radiation in the fit of real GRB data [115]. Parametrized by the peak energy E_p, in the observed νFν spectrum, the photon model of BAND is defined as

$$f_{BAND} = A \begin{cases} (\frac{E}{100keV})^{\alpha} exp[\frac{-(2+\alpha)E}{E_p}], & E < E_c \\ (\frac{E}{100keV})^{\beta} exp(\beta-\alpha)(\frac{E_c}{100keV})^{(\alpha-\beta)}, & E \geq E_c \end{cases} \tag{2.1}$$

where $E_c = (\frac{\alpha-\beta}{\alpha+2})E_p$, A is the normalization factor at 100 keV in units of ph $s^{-1}cm^{-2}keV^{-1}$, α is the low-energy power-law photon index, β is the high-energy power-law photon index, E_p is the peak energy in the νFν space in units of keV, and E_c is the characteristic energy in units of keV. We note that the peak energy E_p represents the position of the peak in the model curve in the νFν space, and the characteristic energy E_c represents the position where the low-energy power law with an exponential cutoff ends and the pure high energy power law starts. These two energies should be distinguished from the smooth broken power law break energy E_b, which represents the position where the low-energy power law joins the high-energy power law. Therefore, we should not compare the Band function E_p or E_c to the smoothly broken power law's E_b.
We compute the break energy where the two power laws join together for the Band function to facilitate a fair comparison of the parameters. It results as $E_b = (\frac{\alpha-\beta}{\alpha+2})\frac{E_P}{2} + 4$, but in the asymptotic limit E_b is proportional to E_p.

The smoothly broken power law (SBPL) is a model of two power laws joined by a smooth transition. It was first parameterized by Ryde (1999) and then

parameterized by Kaneko et al. (2006) as follows:

$$f_{SBPL}(E) = A(\frac{E}{100keV})^b 10^{(a-a_{piv})} \tag{2.2}$$

where

$$\begin{cases} a = m\Delta ln(\frac{e^q+e^{-q}}{2}), a_{piv} = m\Delta ln(\frac{e^{q_{piv}}+e^{-q_{piv}}}{2}) \\ m = \frac{\beta-\alpha}{2}, b = \frac{\alpha+\beta}{2} \\ q = \frac{ln(E/E_b)}{2}, q_{piv} = \frac{log(100keV/E_b)}{2} \end{cases} \tag{2.3}$$

where A is the normalization factor at 100 keV in units of ph $s^{-1}cm^{-2}keV^{-1}$, α and β are the low and high-energy power-law photon indices, respectively, E_b is the break energy in units of keV, and Δ is the break scale. Unlike the Band function, the break scale is not coupled to the power-law indices, so SBPL is a five-parameter model if we let Δ free to vary.

The cutoff power law, the so-called Comptonized model (COMP), is a power-law model with a high-energy exponential cutoff. We note that when $\beta \longrightarrow \infty$, BAND reduces to COMP, as E_c tends to infinity, written as

$$f_{COMP}(E) = A(\frac{E}{100keV})^\alpha exp[\frac{-(2+\alpha)E}{E_p}] \tag{2.4}$$

where A is the normalization factor at 100 keV in units of ph $s^{-1}cm^{-2}keV^{-1}$, α is the power-law photon index, and E_p is the peak energy in the νFν space in units of keV.
We conclude this section by mentioning an additional new model for GRB prompt emission; recent observations with the Fermi Gamma-Ray Space Telescope revealed deviations from the Band function, sometimes in the form of an additional black-body component, while in other cases in the form of an additional power law component extending to high energies [51].

2.2 Data and instruments

In this work we used data coming from two of the main official catalogs presenting results of time-resolved analysis, i.e. the catalog of Yu et al. (2016) [109], which contains 1491 spectra from 81 bursts detected by Fermi/GBM satellite from 14 July 2008 to 13 July 2012, and the catalog of Preece et al. (2000) [87] containing 156 GRBs detected by BATSE. These are currently official catalogs presenting results of time-resolved analysis.

2.2.1 Fermi/GBM

The first dataset here analyzed has been collected by the Gamma-ray Burst Monitor (GBM) of Fermi Gamma-ray Space Telescope, properly used for studying GRBs.

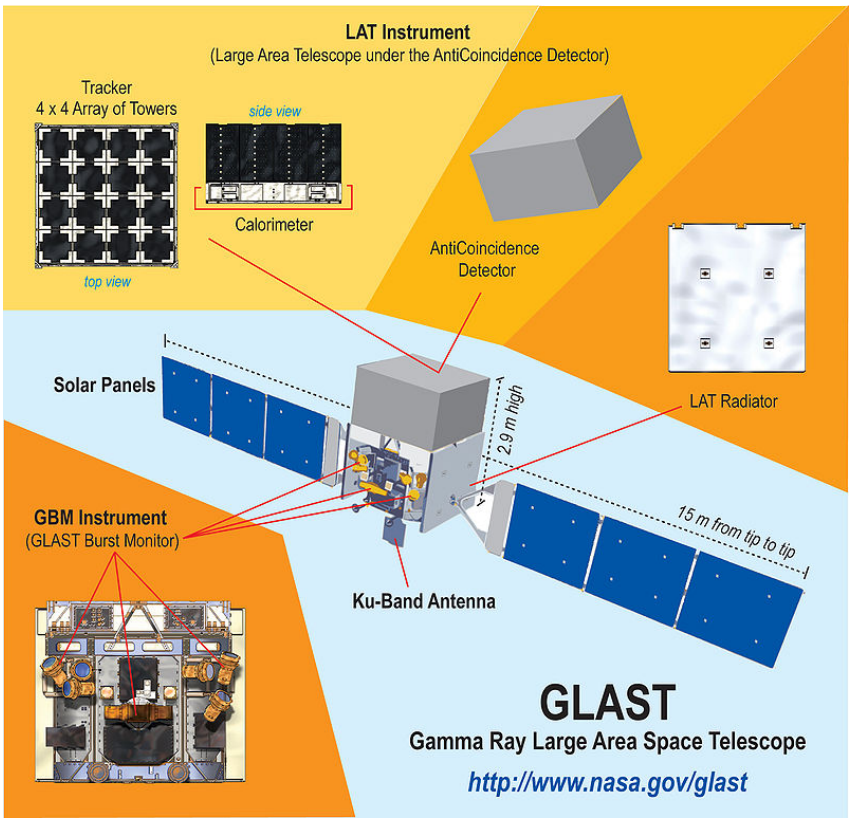

Figura 2.2: Schematic view of the GLAST satellite, named after Enrico Fermi after launch.

Fermi Telescope is a space observatory launched on 11 June 2008 aboard a Delta II 7920-H rocket. A sketch of Fermi satellite is shown in Fig. 2.2.
The mission is a joint venture of NASA, the United States Department of Energy, and government agencies in France, Germany, Italy, Japan, and Sweden. The main goals of Fermi are: a deeper knowledge of our own Galaxy, by improving existing theoretical models of Milky Way, a better comprehension of the mechanisms of particle acceleration in active galactic nuclei, pulsars, and supernova remnants, the resolution of the gamma-ray sky, the study of

the early Universe by analyzing how concentrations of visible and ultraviolet light change over time.
Fermi is used to perform Gamma-ray astronomy observations from low Earth orbit, and is constituted by two instruments on board: the LAT, Large Area Telescope, which detects the brightest, most energetic GRBs, about $\sim$ 10/year, with spectral coverage 30 MeV - 300 GeV, and a field of view comprising $\sim$ 20% of the sky. The resolution of its images is modest by astronomical standards, a few arcmins for the highest-energy photons and about 3 degrees at 100 MeV. It moreover detected bursts not only exceptionally energetic, but also with bright broadband afterglows and extraordinarily fast ejecta.
The other instrument on board of Fermi is the GBM. It consists of 12 thallium activated sodium iodide detectors, NaI detectors, whose energy range goes from 8 keV to $\sim$ 900 keV and 2 bismuth germanate detectors, BGO detectors, which detect harder photons of the energy range 200 keV - 40 MeV. Each detector views a different portion of the sky so that, for a particular burst, there will be varying amounts of signal in the different detectors; indeed its scintillators are on the sides of the spacecraft to view all of the sky which is not blocked by the Earth. Moreover, it provides real-time locations for GRB triggers. These real-time locations are circulated via the Gamma ray Coordination Network (GCN), which permits ground-based follow-up observations. The wide spectral coverage of over 3 orders of magnitude is the key to detailed spectral analysis for the GRB prompt emission phase.
For every spectrum, a maximum of two NaIs with one BGO are used in the analysis.
GBM generates three types of data; the first one includes CTIME data, which provide rough spectral resolution of 8 energy channels and fine temporal resolution of 0.256 s during the nominal time period, i.e., before the trigger and 600 s after the trigger; during the trigger period, the resolution is increased to 64 ms. The second type of data are the CSPEC ones, which provide coarse temporal resolution at nominal (4.096 s) and trigger (1.024 s) period, and high spectral resolution of 128 energy channels. The third type is the so called "time tagged event (TTE) data, which store individual photon events tagged with arrival time (resolution of 2μ s), photon energy channel (128 pseudo-logarithmic energy channels), and detector number (NaI 0-11 and BGO 0-1). The TTE data were stored on board GBM in a recycling buffer. After 26 November 2012 this data type became continuous. When GBM is triggered, the spacecraft transmits pre- and post-trigger TTE data

(about 300 s in duration) to the ground as science data. Since only TTE data from $\sim$ 30 s pre-trigger until $\sim$ 300 s post-trigger are available, for the bursts with evident precursor or emission longer than 300 s, CSPEC data (about 8000 s in duration) are used.
The data of GBM can be downloaded from the HEASARC BROWSE GBM Burst Catalog freely.

2.2.2 CGRO/BATSE

The second dataset here analyzed is that one obtained using BATSE, on board of the CGRO (Fig. 2.3). It was launched from Space Shuttle Atlantis

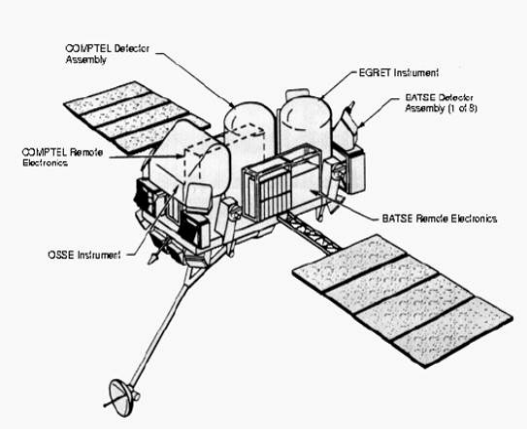

Figura 2.3: Schematic view of the CGRO satellite, composed by BATSE, OSSE, EGRET and COMPTEL.

during STS-37 on April 5 1991, and operated until its deorbit on June 4 2000. It was deployed in low earth orbit at 450 km to avoid the Van Allen radiation belt. It was the heaviest astrophysical payload ever flown at that time at 17,000 kilograms. It consists of eight separate NaI-based detector modules located on all corners of the Compton Gamma Ray Observatory spacecraft; four are on the top, the others four are on the bottom. The Large Area Detectors (LADs), made up of 128 pseudo logarithmically channels covering the 20 keV to $\sim$ 2 MeV range, are constructed as a large, thin, flat collection area (2000 $cm^2 \times 1.27$ cm) with roughly a cosine angular response. To ensure maximal sky coverage for all eight detectors, the flat faces of the detectors are oriented parallel to the faces of a octahedron. We have already said that its accuracy is $\sim$ 2 deg, thanks to the independent detectors response. The

LADs are most useful if the energy range they observe is constant over time. This conforms to their design for longterm monitoring of transient gamma-ray sources. The on-board trigger can consist of any combination of four channels, respectively 25-50, 50-100, 100-300 and > 300 keV, in three timescales, 64, 256, and 1024 ms, but for the majority of the mission, the triggers 50-300 keV have been used, since this combination is empirically found to be optimal for GRBs.
BATSE is also made up by another instrument, i.e. Spectroscopic Detectors (SDs). They are smaller and thicker ($127cm^2 \times 7.2$ cm) than the LADs to maximize photon capture and energy resolution and thus have a more uniform angular response. The principal axis of each SD is offset in angle from the normal vector to the face of the associated LAD by 18.5 deg.
Each of the eight BATSE modules consists of one LAD and one SD. In view of the fact that the LAD collecting area is almost 16 times that of the SDs, data from the LADs are preferred. The time resolution of the two BATSE detector types is identical until the LADs fill up the on-board memory, at which time the electronics again determine whether it should change the accumulation criteria for the remaining SD memory.
The LADs provided various types of data used for various purposes. The data were collected in either burst mode or non-burst mode.
The burst mode data accumulation starts when a burst is triggered, whereas the non-burst-mode data were usually continuous, except for possible telemetry gaps. The burst mode data generally provide higher resolution either in energy or in time than the non-burst-mode data. The three LAD data types used, in order of priority, are High Energy Resolution Burst data (HERB), Medium Energy Resolution data (MER), and Continuous data (CONT).
The HERB and MER data are burst-mode data, for which the acquisition begins at the time of a burst trigger, whereas CONT are continuous, non-burst-mode data. HERB provides the highest energy resolution consisting of ~ 120 usable energy channels in energy range of $\sim 30 - 2000$ keV with modest subsecond time resolution and thus is used as the primary data type. The coarser time resolution (~ 300 s) High Energy Resolution data (HER) are used as background data for the HERB, covering several thousand seconds before the trigger and after the HERB accumulation is finished.
However, especially for long, bright bursts, the HERB data can often be incomplete since HERB had a fixed memory space that could fill up before the burst was over. HERB data are considered incomplete when they do not cover the burst duration (T_{90}) or when the data do not include the main peak

episodes (this could occur if a burst data accumulation is triggered by weak precursor). In such cases, or if HERB was not available, 16-energy-channel MER data are used instead. Although MER provides medium energy resolution, it has much finer time resolution (16 and 64 ms) than HERB, making it possible to recreate the time resolution of the missing HERB. In the MER data, the CONT data are used as background.
The downside of using MER is that the data are summed over multiple sets of detectors (usually two to four) and, therefore, systematic errors tend to dominate over statistic errors, especially for bright bursts. Systematic errors cannot be modeled into the analysis and can contribute to large χ^2 especially at lower energies due to the high counts.
Data from the GRB spectral catalog compiled by Adam Goldstein are available for download in the BATSE Spectral Catalog.

2.3 Analysis of Fermi/GBM spectral catalog by Yu et al. 2016

The first part of my work is based on the analysis of GRBs contained in the Yu et al. catalog, through a systematic analysis of the temporal evolution of E_p and its correlation with the flux. Indeed, the slope and the scatter of E_p – Flux are the same of the correlation E_p – L, but unbiased by cosmological effects and uncertainties related to the opening jet angle. Thus, a systematic analysis of the slope and the scatter in the E_p – Flux correlation allows a cosmology-independent calibration in E_p – "Intensity (i.e. Luminosity or radiated energy) correlation. This has relevant implications in cosmology and in the physics prompt emission understanding of GRBs. I have also focused my attention on a small sample of GRBs, whose behavior was not so ordinary in terms of the correlation, in order to deepen my analysis and to shed some light on the physics of the prompt emission of GRBs.

Yu et al. have considered all the bursts detected by GBM in the first four years (i.e. from 14 July 2008 to 13 July 2012), which is the same GRB subset as used in the four-year GBM GRB time-integrated spectral catalog [50], [103]. In their catalog (Fig. 2.4) they used CSPEC data for 15 GRBs, and TTE data for all other bursts. The GBM triggered on 954 GRBs in this period of time (one of them triggered GBM twice (see [103]).

GRB name	spectrum	T_{start}:T_{stop} (s)	BEST model	A (ph s^{-1} cm^{-2} keV^{-1})	α	β	E_p (keV)	E_b (keV)	CSTAT/dof	photon flux (ph s^{-1} cm^{-2})	energy flux (erg s^{-1} cm^{-2})
(1)	(2)	(3)	(4)	(5)	(6)	(7)	(8)	(9)	(10)	(11)	(12)
080817161	1	−6.144:4.344	COMP	0.0067 ± 0.0010	−0.835 ± 0.060	–	637.80 ± 96.70	–	570.4/480	2.1682±0.24	5.7087E-07±5.5E-08
080817161	2	4.344:5.885	COMP	0.0313 ± 0.0034	−0.829 ± 0.047	–	668.50 ± 79.10	–	492.51/480	10.172±0.82	2.7450E-06±1.8E-07
080817161	3	5.885:7.150	COMP	0.0444 ± 0.0053	−0.827 ± 0.048	–	512.90 ± 53.90	–	529.13/480	13.263±1.1	3.1743E-06±2.2E-07
080817161	4	7.150:8.200	SBPL	0.0439 ± 0.0048	−0.863 ± 0.056	−2.121 ± 0.122	388.69 ± 137.52	191.10 ± 30.90	517.04/479	15.266±1.4	3.3723E-06±2.6E-07
080817161	5	8.200:10.956	COMP	0.0303 ± 0.0049	−0.871 ± 0.057	–	348.20 ± 36.10	–	522.13/480	8.1164±0.93	1.5151E-06±1.4E-07
080817161	6	10.956:12.591	COMP	0.0288 ± 0.0041	−0.865 ± 0.052	–	479.60 ± 56.60	–	497.74/480	8.5970±0.92	1.9294E-06±1.7E-07

Figura 2.4: Schematic view of the Yu et al. catalog, presenting the name of GRBs, their time at which detection of their burst respectively starts and ends, the best model fitting their spectrum, normalization, the low-energy photon index, the high-energy photon index, E_p, the break energy E_b, CSTAT value and degrees of freedom, photon flux and finally their energy flux.

Time-resolved spectral analysis requires bright bursts with sufficiently high signal-to-noise spectra. This bright subsample, drawn from Yu et al. catalog, is selected by applying the following criteria: 10 keV - 1 MeV energy fluence f$> 4 \times 10^{-5}$ erg cm^{-2} and/or 10 keV - 1 MeV peak photon flux $F_p > 20$ ph $s^{-1}cm^{-2}$ (in either 64, 256, or 1024 ms binning timescales). These criteria are satisfied by 134 bursts out of the 954; among these, 16 belong to the short burst class. In order to alleviate the problem related to the incidence of the brightest burst to the statistics, they further required each event to have at least five time bins in the light curves when binned with signal-to-noise ratio (S/N) = 30. As a result, 81 bursts satisfy these criteria; among these, there is only one short burst (GRB 120323A).
In total, 1802 time-resolved spectra were obtained. For every spectrum, a maximum of three NaIs with one BGO are used in the analysis, by adopting the following method for background subtraction. For each burst, a polynomial with order 2-4 is fit to every energy channel according to two user-defined background intervals, before and after the emission period. The background model is then interpolated across the emission period. This has been carried out by varying the selected intervals and order of polynomial until the χ^2 statistics [1] is minimized over all energy channels. The resulting background intervals have been then loaded to all detectors, generating the background model to be used in the spectral analysis.
Four different empirical models (Band function, cut off power law model, smoothed broken power law and a simple power law) were fit to each spectrum by adopting the C–statistics (CSTAT, [13]), which is well suited for

[1]The value of χ^2 is $\chi^2 = \sum \frac{(o_i - e_i)^2}{e_i}$, where o_i is the observed value and e_i the expected one, given a possible probability distribution generating the sample.

low-photon statistics spectra, resulting in a compilation of $1802 \times 4 = 7208$ spectral fits. Compared to the four-year GBM GRB time-integrated spectral catalog [50], [103], the catalog presented by Yu includes a lower number of GRBs (81 vs. 943). However, the number of high-resolution spectra is higher (1491 BEST model fits vs. 943). Most of the intervals of GRBs presented in Yu et al. catalog have been fit with the COMP model, meanwhile a significant percentage has been fit with the BAND model and just a small fraction with the SBPL model.
In the catalog, Yu et al. report for each interval of each GRB its name using the Fermi GBM trigger designation, the spectrum number within individual burst, the time T_{start} when burst begins to be triggered and the time T_{end}, i.e. when the detection ends, the best–fitting model (BEST), the best-fit parameters of the BEST models, i.e. normalization for all, α, β and E_p for the Band function (BAND), α and E_p for the cut–off power–law model (COMP), α, β, E_p and E_b for the smoothed broken power–law model (SBPL), α for the simple power-law model, the values of CSTAT per degrees of freedom (DOF) and the 10 keV - 1 MeV photon and energy fluxes, respectively. We have to mention that where there is a higher statistics, Yu et al. have provided values of E_p even in time intervals lasting $< 1s$. All these parameters are reported with their own errors.

Firstly, through an IDL script, we have divided GRBs of this catalog into different subgroups on the basis of the model used for fitting the spectra, the goodness-of–fit (i.e., the value of CSTAT/DOF), the relative error on E_p and the fraction of time intervals selected. Indeed, we have conceived three different working schemes to divide GRBs into subgroups. In the first one, which we term A, we have decided to regroup GRBs in a subsample as large as possible, thus we have chosen all GRBs having their spectra fit, independently on the model used, with a value of $CSTAT/DOF < 10$, a value of $\Delta_{E_p}/E_p < 1$ and considering their whole burst duration. Thereafter, in the scheme that we call B, we have applied the same criteria of the scheme A, but here we have considered only the second part of the burst duration of GRBs in order to exclude the points at the beginning of the observation, which often do not follow the correlation, and in order to obtain more refined plots. Finally, in the scheme C, we have included GRBs fits independently on the model used, a value of $CSTAT/DOF < 1.3$, a value of $\Delta_{E_p}/E_p < 0.5$ and by considering only the second part of the burst duration. In this last scheme we have applied the most restrictive criteria in order to "clean" the

plots and exclude some outliers, which could spoil the results. Actually, we have divided GRBs into different subgroups because one of the goals of our analysis is to understand how the correlation depends on various criteria, e.g. on the fraction of intervals selected or any instrumental effect. In this way we will use GRB correlations with much more confidence. In Tab. 2.1 we sum up the working schemes used in this section.

Tabella 2.1: Summarizing scheme for our analysis.

	Scheme A	Scheme B	Scheme C
Model	All	All	All
CSTAT/DOF	< 10	< 10	< 1.3
Δ_{E_p}/E_p	< 1	< 1	< 0.5
Duration of the burst	100%	50%	50%

Then, for every GRB of each sample we have extracted the temporal evolution of the flux (lightcurve) and of E_p (renormalized in arbitrary units, in order to show both the trends of flux and E_p in the same plot) and produced a plot of the E_p–Flux correlation, by fitting the correlation between these two quantities with two different linear functions taking into consideration the errors on both X and Y; the first one is the so called Fitexy function, which provides the normalization and the slope (with their own errors) which minimize the χ^2 of the fit, and the value of χ^2; the second one is the so called Reichardt function, that provides further the so called "extrinsic scatter" σ_{ext}, the likelihood function and the normalization and the slope (without errors) which minimize it.
For each subsample of GRBs, we have obtained the histograms of the distributions of the slope obtained through both Fitexy and Reichardt functions and also the distribution of the extrinsic scatter obtained through the Reichardt function alone; all these distributions have been fit with a Gaussian function, in order to check if these distribution could be considered stochastic.
The mean values of the slopes and of the scatter are arithmetic means and the errors associated have been calculated through the propagation of errors.

2.3.1 Results

Firstly, we have used the scheme A. In this scheme we have found that most of the GRBs follow quite well the correlation, i.e. in their lightcurves there is a good tracking between E_p and the flux, although a not-negligible extra-statistical scatter is still present, as we can see, for example, in the lightcurve and E_p – Flux plot of GRB 090902. The scatter of data points of this GRB in this fit, with respect to the relation, is $\sigma_{ext} = 0.24 \pm 0.02$, the coefficient of correlation (i.e. the so called coefficient of Spearman [2]) is 0.74, the number of time intervals considered is 93 and its chance probability (i.e. the probability that the correlation is not casual, the lower the better is the correlation) is 1.99×10^{-17} (see Fig. 2.5).

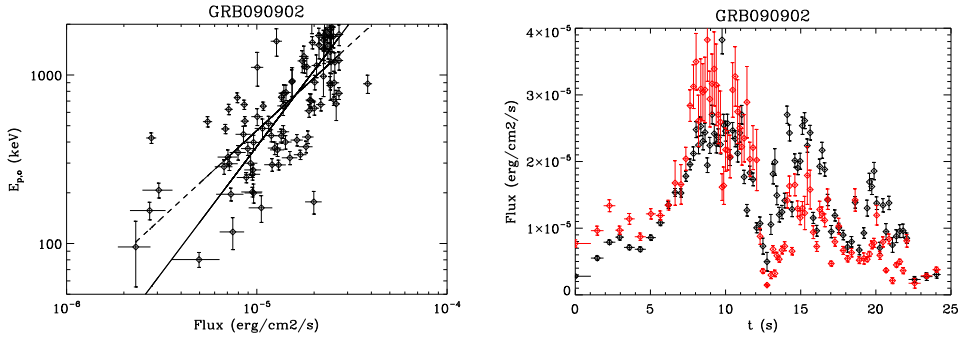

Figura 2.5: Left panel: the E_p–Flux correlation of GRB 090902 by selecting the scheme A. Solid line is the fit through Fitexy function, the dotted one through Reichardt function. Right panel: the corresponding temporal evolution of E_p and Flux of GRB 090902. Black points represent the Flux, red ones the E_p.

Conversely, we have found some GRBs in which some points do not follow the correlation, in particular at the beginning and at the end, as we can see in Fig. 2.6 for GRB 080817; indeed, we can note that in the first pulse and at the end of the tail the flux does not track E_p. This plot has a scatter $\sigma_{ext} = 0.08 \pm 0.02$, a coefficient of correlation equal to 0.54, number of time intervals considered 15 and a chance probability equal to 0.03.

[2]The coefficient of correlation of Spearman is a statistical not-parametric measure of correlations. It assesses how well the relationship between two variables can be described using a monotonic function (whether linear or not). A monotonic relationship is a relationship that does one of the following: (1) as the value of one variable increases, so does the value of the other variable; or (2) as the value of one variable increases, the other variable value decreases. If the value $r = 1$ means a perfect positive correlation and the

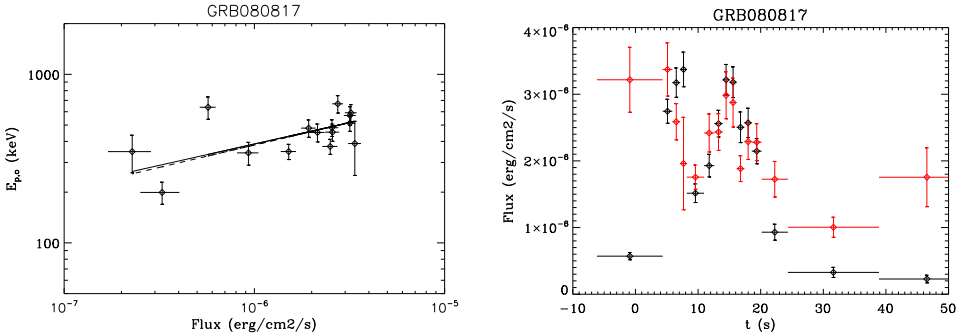

Figura 2.6: Left panel: the E_p–Flux correlation of GRB 080817 by selecting the scheme A; right panel: the corresponding temporal evolution of E_p and Flux. The legend is the same of the Fig. 2.5. We can note that at the beginning and at the end some points do not follow the correlation.

In order to further investigate this issue, we have decided to take into consideration only the second part of the time intervals in each GRB (scheme B); indeed we have noticed that generally the first intervals do not follow very well the correlation, and this fact could be due to the existence of two possible phases of the emission, where the emission mechanism generating the correlation is dominant only in the decay phase. Thus, we have noticed that the scatter has been quite reduced, with respect to the corresponding plots in scheme A, as we can see in both Fig. 2.7 and Fig. 2.8 for GRB 090902 and GRB 080817, respectively; indeed the dispersion of the first GRB in this scheme is $\sigma_{ext} = 0.11 \pm 0.01$, the coefficient of correlation is 0.80 (higher than that found in the scheme A), the number of time intervals considered is 46 and the chance probability is 10^{-11}. Moreover, the dispersion of the second GRB in this scheme is lower than 0.06, the coefficient of correlation is 0.85 (higher than that found in the scheme A), the number of time intervals considered is 7 and the chance probability is 0.01. Thus, we can say that by excluding the second part of the burst observation we have improved both the fits, finding higher values of both the coefficients of correlation and lower values of both the chance probability.

Consequently, we have further refined the other selection criteria by choosing the working scheme C; we have achieved an evident improvement of the fits, i.e. the extra-Poissonian scatter was further reduced with respect to the scatter obtained in scheme A, as we can notice in Fig. 2.9 and in Fig. 2.10 for

value $r = -1$ means a perfect negative correlation.

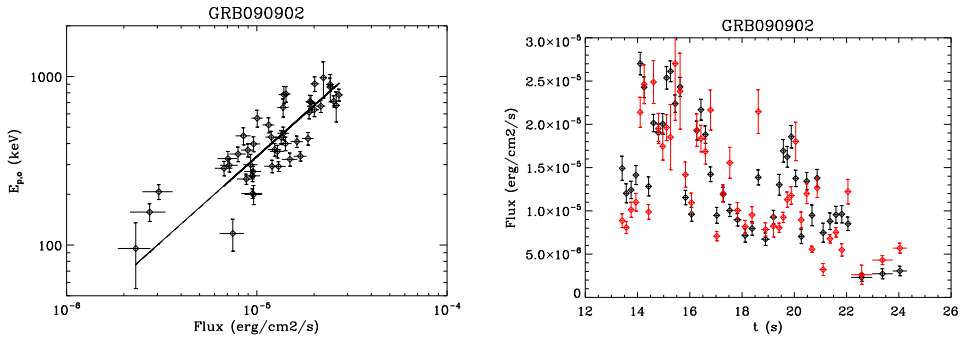

Figura 2.7: Left panel: the E_p–Flux correlation of GRB 090902 by selecting the scheme B; right panel: the corresponding temporal evolution of E_p and Flux. The legend is the same of the Fig. 2.5. We can notice that in the plot the scatter has been reduced, while in the lightcurve there is a better tracking between E_p and flux.

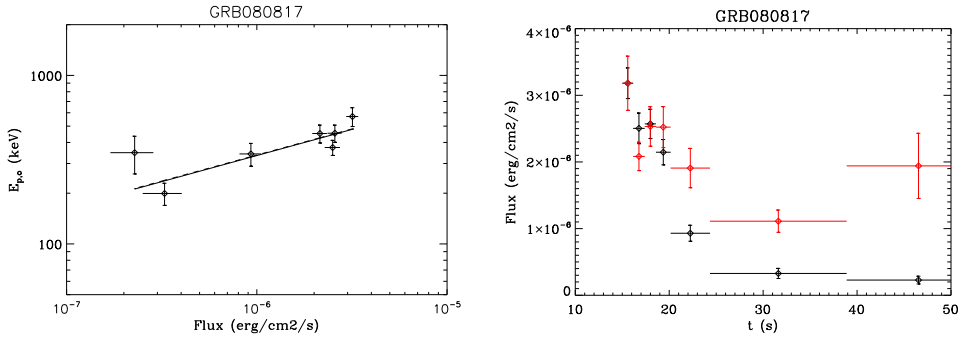

Figura 2.8: Left panel: the E_p–Flux correlation of GRB 080817 by selecting the scheme B; right panel: the corresponding temporal evolution of E_p and Flux. The legend is the same of the Fig. 2.5. We can notice that in the plot the scatter has been reduced, while in the lighcurve there is a better tracking between E_p and flux.

GRB 090902 and GRB 080817, respectively; indeed the scatter of data points of the first GRB in this fit, with respect to the relation, is $\sigma_{ext} = 0.12 \pm 0.01$, the coefficient of correlation is 0.82 (higher than both values found previously), the number of time intervals considered is 39 and the chance probability is 1.08×10^{-10}. Similarly, the scatter of data points of the second GRB is still lower than 0.06, the coefficient of correlation is 0.85 (higher than both values found previously), the number of time intervals considered is 7 and the chance probability is 0.01. The results of these fits are summed up in Tab. 2.2.

Tabella 2.2: Values of the scatter, chance probability, coefficient of correlation and number of time intervals considered obtained for GRB 080817 and 090902 for scheme A, B and C.

GRB080817	Scheme A	Scheme B	Scheme C
$N°$ of time intervals	15	7	7
σ_{ext}	0.08 ± 0.02	< 0.06	< 0.06
Coefficient of correlation	0.54	0.85	0.85
Chance probability	0.03	0.01	0.01
GRB090902			
$N°$ of time intervals	93	46	39
σ_{ext}	0.24 ± 0.02	0.11 ± 0.01	0.12 ± 0.01
Coefficient of correlation	0.74	0.80	0.82
Chance probability	1.99×10^{-17}	10^{-11}	1.08×10^{-10}

Finally, we can conclude that in the scheme C we have obtained an improvement of the fits by applying more restrictive criteria of selection; we have reduced significantly the measure of the dispersion of the correlation, with respect to the previous schemes, and obtained higher values of coefficient of correlation and, then, lower values of chance probability (indeed these two parameters are linked each other).

Then, for each subgroup of GRBs, we have obtained the distributions of the best–fit parameters, in which some outliers are present, whose nature needs still to be investigated.
Tab 2.3 summarizes the results of the distributions, showing the arithmetic mean values and their errors, calculated through the propagation of the errors, for both the slopes and the scatter achieved through the two different fits. The histograms for the slopes of the correlation obtained through Fitexy

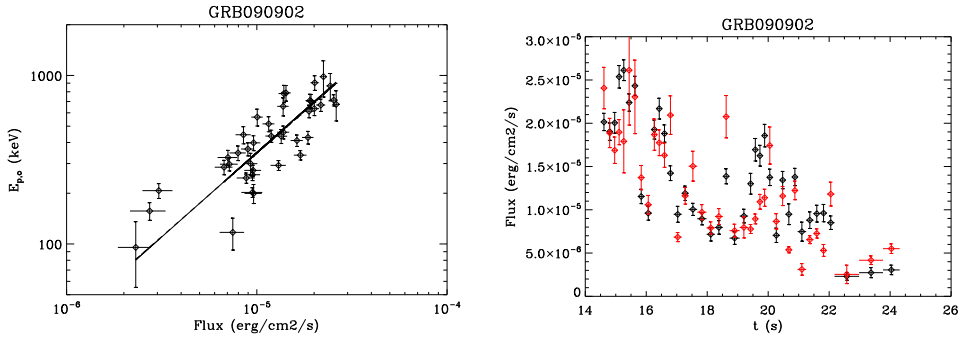

Figura 2.9: Left panel: the E_p–Flux correlation of GRB 090902 by selecting the scheme C; right panel: the corresponding temporal evolution of E_p and Flux. The legend is the same of the Fig. 2.5. We can notice that in the plot the scatter has been further reduced with respect to scheme A, and that the tracking between E_p and the Flux has been improved after the selection on all the parameters.

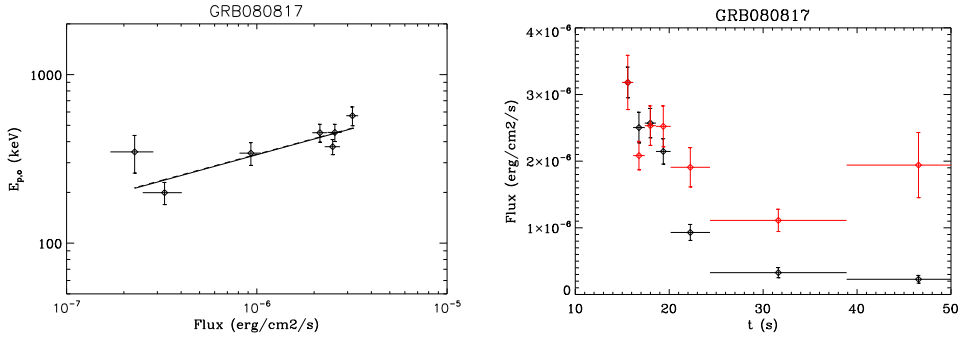

Figura 2.10: Left panel: the E_p–Flux correlation of GRB 080817 by selecting the scheme C; right panel: the corresponding temporal evolution of E_p and Flux. The legend is the same of the Fig. 2.5. We can notice that in the plot the scatter has been further reduced with respect to scheme A, and that the tracking between E_p and the Flux has been improved after the selection on all the parameters.

Tabella 2.3: Mean values of the slopes and of the scatter obtained through Fitexy and Reichardt functions for scheme A, B and C.

	Scheme A	Scheme B	Scheme C
m_{fit}	0.31±0.04	0.49±0.12	0.48±0.13
m_{Reich}	0.37±0.01	0.43±0.02	0.42±0.02
σ_{ext}	0.12±0.01	0.07±0.02	0.06±0.01

function are shown in Fig. 2.11.

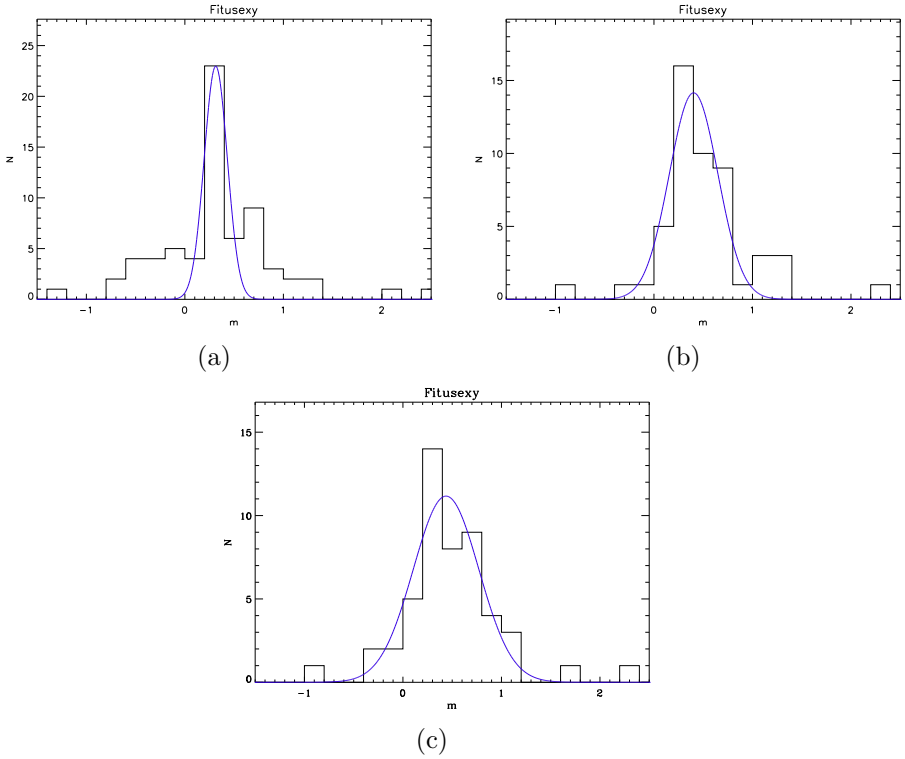

Figura 2.11: Distribution of the slope of the correlation obtained through Fitexy function fit using a Gaussian for the scheme (a) A, (b) B and (c) C.

The histograms of the slopes of the correlation obtained through Reichardt function for each scheme are shown in Fig. 2.12.

The histograms related to the dispersion obtained through Reichardt function are shown in Fig. 2.13. For these histograms we have considered only the values of the dispersion higher than their own errors; indeed, among the values of the dispersion, there is a fraction of values consistent with zero (initially they had appeared in the histograms as an excess around zero, its minimum value). We have excluded them. However, we have decided to fit the histograms of the dispersion with a Gaussian in order to show that there could be a small fraction of values consistent with zero.

Interestingly, we can note that, by refining the selection criteria (see also Fig. 2.11, Fig. 2.12 and Fig. 2.13), both the values of the slope obtained through this time resolved analysis become closer to that one estimated for

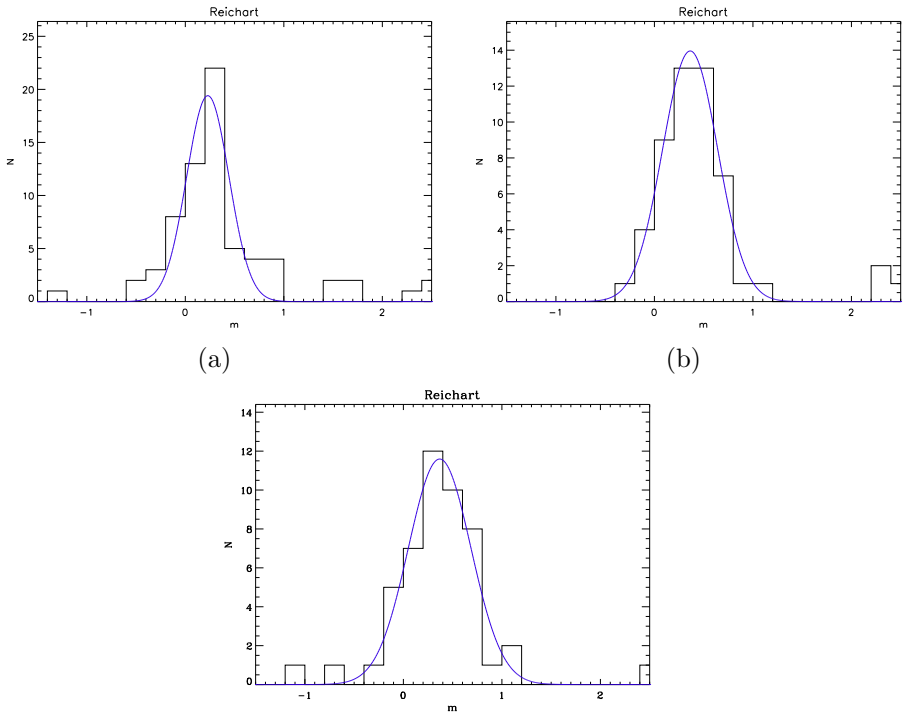

Figura 2.12: Distribution of the slope of the correlation obtained through Reichardt function fit using a Gaussian for the scheme (a) A, (b) B and (c) C.

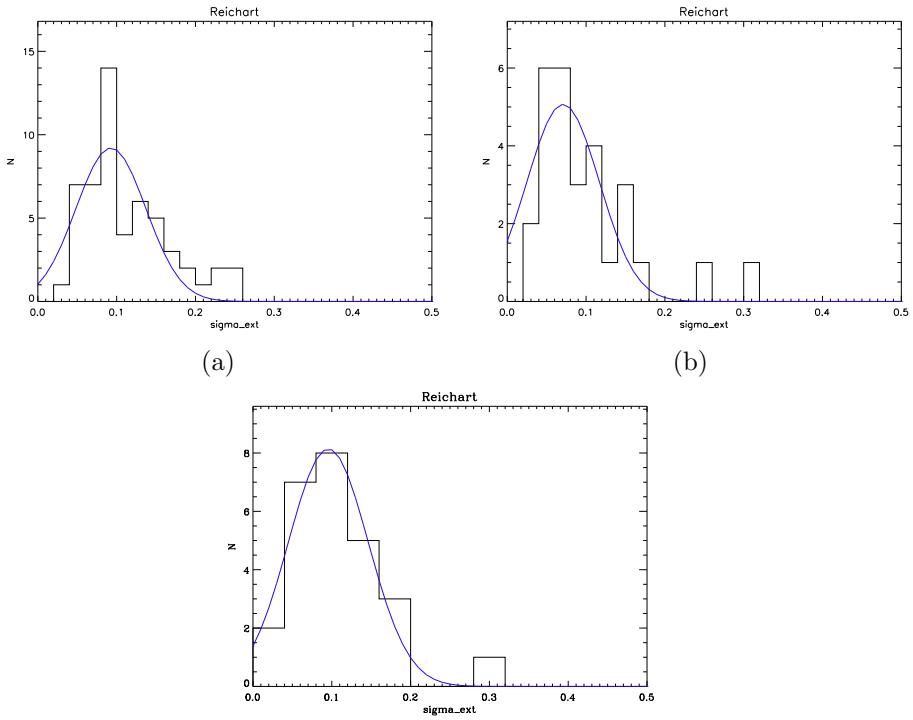

Figura 2.13: Distribution of the dispersion obtained through Reichardt function fit using a Gaussian for the scheme (a) A, (b) B and (c) C.

the correlations based on time integrated (averaged) analysis, whose value is $m \sim 0.5$, although the corresponding errors increase, probably because the number of the points has been reduced by applying more restrictive criteria of selection. However, the difference of the results of schemes B and C is not so relevant.
Instead, the value of σ_{ext} that we have found is always lower than the one characterizing the Amati relation in time–integrated analysis, $\sigma_{ext} = 0.2$; in fact we have obtained $\sigma_{ext} \sim 0.1$. This result shows the true dispersion of the $E_{p,i}$ – "intensity" correlation, because Reichardt function provides the extra-dispersion (i.e. not-statistical), unbiased by any cosmological effect or uncertainty related to the jet opening angle.

The results of this statistical analysis allow us to point out that, although there is a not-negligible dispersion of the $E_{p,i}$ – "intensity" correlation, both the slope and the scatter would basically converge to precise values, i.e. $m \sim 0.5$ and $\sigma_{ext} \sim 0.1$, as already said. This result has been already confirmed by other authors in other works (see e.g. [72] [32]), although they had used a different method. Thus we could assume that the $E_{p,i}$ – "intensity" correlation is a sort of universal correlation, i.e. valid for all GRBs.
In this work we have also performed an innovative method to statistically estimate the mean values of slope and dispersion, with the believe that all GRBs follow the same correlation; we have calculated the slope and the dispersion of such universal correlation by fitting simultaneously, only with the Reichardt function, the $E_{p,i}$ – flux for all the GRBs present in Yu et al. catalog; finally, the slope and the scatter that minimize the sum of the $-log(likelihood)$ of all GRBs are intended as the "best values". This kind of approach has never been used. The results of this procedure are shown in Tab. 2.4 (where errors are at 1σ).

Tabella 2.4: Mean results of slope and dispersion obtained through the simultaneous fit of the correlation with the Reichardt function for scheme A, B and C.

	Scheme A	Scheme B	Scheme C
m_{Reich}	0.45±0.02	0.42±0.02	0.42±0.02
σ_{ext}	0.154±0.004	0.096±0.005	0.088±0.005

We have to mention that the normalization is different for each GRB, but we have overcome this issue by calculating it through the values of m and

σ_{ext} of each GRB, through the following equation:

$$k_{TOT} = \sum \frac{(E_p - mE_{iso})}{\sigma^2 + \sigma^2_{E_p} + (m\sigma_{E_{iso}})^2} / \sum \frac{1}{\sigma^2 \sigma^2_{E_p} + (m\sigma_{E_{iso}})^2} \qquad (2.5)$$

where the summation is on all the data. The results of the simultaneous fit are consistent with those found previuosly (see Tab. 2.3); by applying more restrictive criteria, the scatter has been reduced as well as the corresponding error, while the value of the slope does not change significantly.
We can conclude that the results of the slope converge on the value $m \sim 0.5$ and a value of the scatter $\sigma_{ext} \sim 0.1$.

2.4 Complementary spectral analysis of Fermi/GBM data

In order to investigate what can be the possible causes of the bad tracking of some points in few cases (about 1/3 of the total number of GRBs in Yu et al. catalog), we have decided to independently reduce and analyze the Fermi spectra of some GRBs, through two different tools, i.e. the GBM official spectral analysis software RMFIT 1 v4.3BA (the Fermi Science Tools) and the X-Ray Spectral Fitting Package XSPEC [5].
The main aim of this analysis was to check if spectra, for example, at the beginning and at the end of the burst (i.e. when the points do not follow the E_p – flux correlation) were affected by any background subtraction problems, or if they need any additional spectral components, or a different fitting method.
I have focused my analysis on a sample of three GRBs, i.e. 080817, 080916C and 080825, all showing this kind of "outliers" especially at the very beginning or ending phases of the burst.
Firstly, we have retrieved the data from the the public Fermi GBM Burst Catalog (https://heasarc.gsfc.nasa.gov/W3Browse/fermi/fermigbrst.html). In this work, for extracting the spectra we have used TTE data and CSPEC data, which provide high temporal and spectral resolution. Then, through the tool GTBIN we have obtained the lightcurves of these GRBs by choosing a linear binning. The subtraction of the background was performed by choosing a time range after the burst in which the signal was quite flat. Secondly, we have created PHA-II FITS files, which contain an energy spectrum for

each time bin. We have selected, for each GRB, the two most illuminated NaI scintillators detectors triggered by the burst and one BGO detector. For the first ones the first 5 channels and those above 128 have been removed because they could be beyond the instrument response function reliable energy range, or affected by non-linearities, or be overflow channels (all counts above a certain energy end up in that channel), resulting in an effective energy band of $\sim$ 8–1000 keV. Similarly to Sec. 2.3, for the BGO detectors the first 200 channels and those ones above 2000 have been removed, giving an energy band of $\sim$250–3800 keV. The matrix response for each detector was provided in the archive itself.

In order to further investigate the influence of background subtraction and fitting methods on the results of spectral analysis, I analyzed the same spectra also through the tool RMFIT. We used the same data retrieved from the public Fermi GBM Burst Catalog; in this case RMFIT allowed me to subtract the background in a different and more sophisticate way, i.e. we had the chance to select two time intervals, respectively about 20 s before the burst and a time range, after the burst, where the signal was quite flat. Then, we have chosen the order 2 of the polynomial to interpolate the background for the NaI detectors, while the order 1 for BGOs. In this way we have obtained a more sophisticated subtraction of the background, in comparison with that one performed in XSPEC. The fits with RMFIT were performed by using both the CSTAT and χ^2 statistics and testing the COMP and BAND models.

Thus, it was possible to obtain a spectrum for each of the GRB time intervals considered by Yu et al. 2007 and fit with the BAND and COMP models, by adopting two different statistics, i.e. χ^2 and CSTAT. Three examples of reduced spectra are shown in Fig. 2.14, 2.15 and 2.16 that we call (1), (2) and (3), respectively, fitting the second interval of the GRB080817 with different softwares and statistics. The fit parameters are summarized in Tab. 2.5. Although the models used are different, the fits are quite good, i.e. consistent with each other; the only difference is related to the subtraction of the background of XSPEC with respect to RMFIT.

We have also fit these GRBs spectra with another model, the so called GRB-COMP model (Fig. 2.17), proposed by Titarchuk et al. (2012) [99] and tested on BeppoSAX and BATSE spectra by Frontera et al. (2013) [33].

This is essentially a photospheric two-phase model for the prompt emission: up to the peak energy E_p of the spectrum we can describe the physics mechanism of the emission with soft thermal blackbody-like photons Comptonized

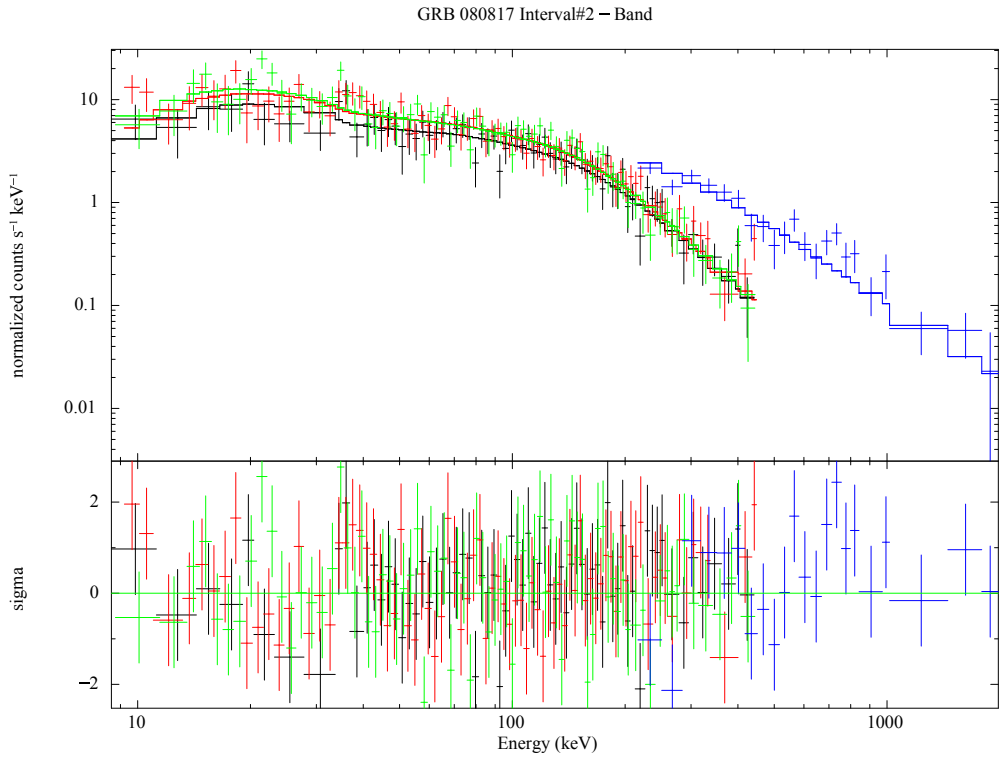

Figura 2.14: Spectrum of the second interval of GRB 080817, fit through XSPEC with BAND function using χ^2 statistics. Green and red points represent NaI detectors, while the blue ones BGOs detectors. The bottom panel shows the distribution of the residuals in terms of σ.

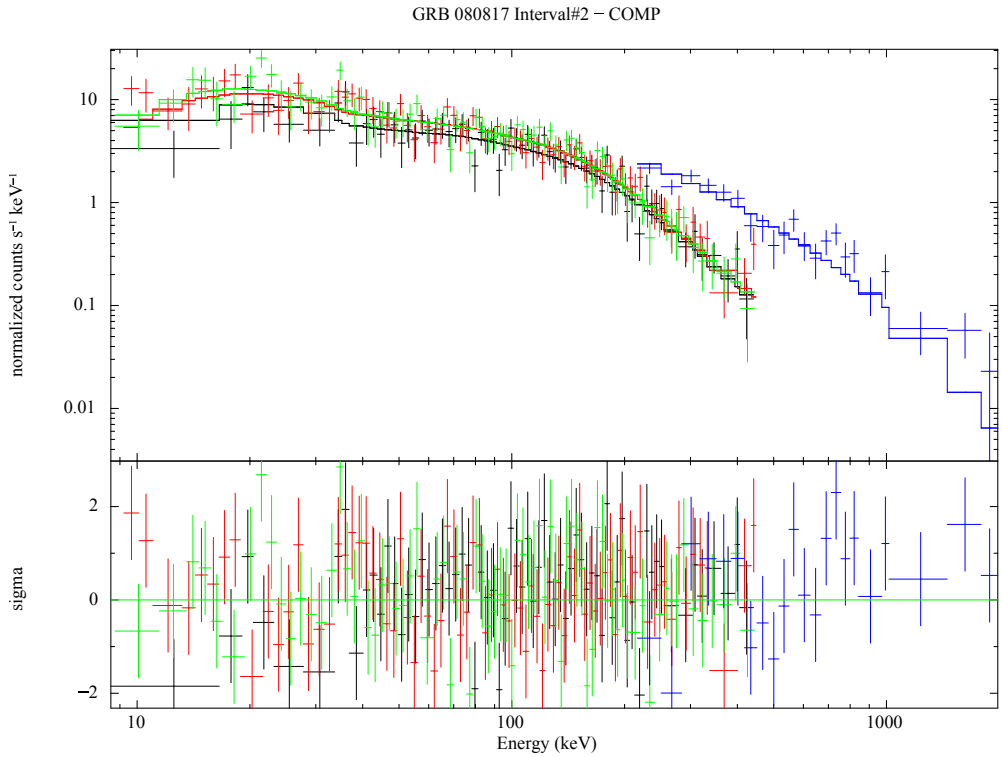

Figura 2.15: Spectrum of the second interval of GRB 080817, fit through XSPEC with COMP model using χ^2 statistics. Colors are the same of Fig. 2.15. The bottom panel shows the distribution of the residuals.

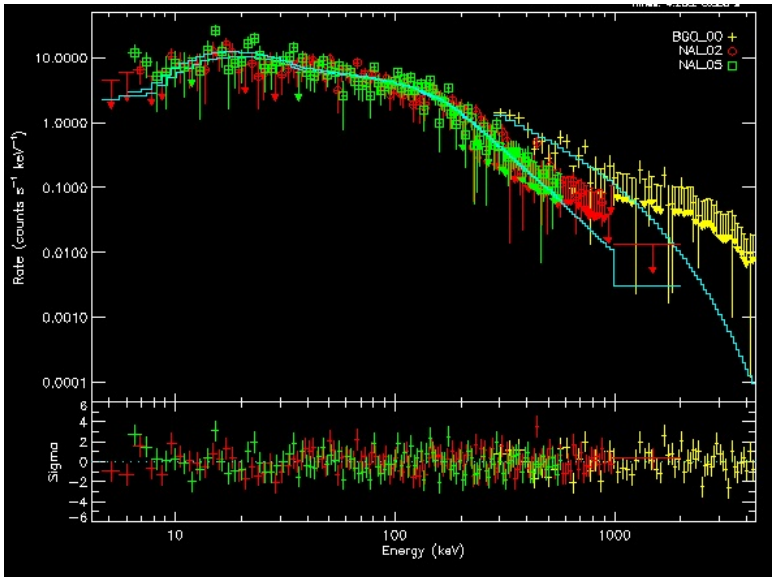

Figura 2.16: Spectrum of the second interval of GRB 080817, fit through RMFIT with COMP model using CSTAT statistics. Colors are the same of Fig. 2.15. The yellow arrows at high energies indicate upper limits. The bottom panel shows the distribution of the residuals.

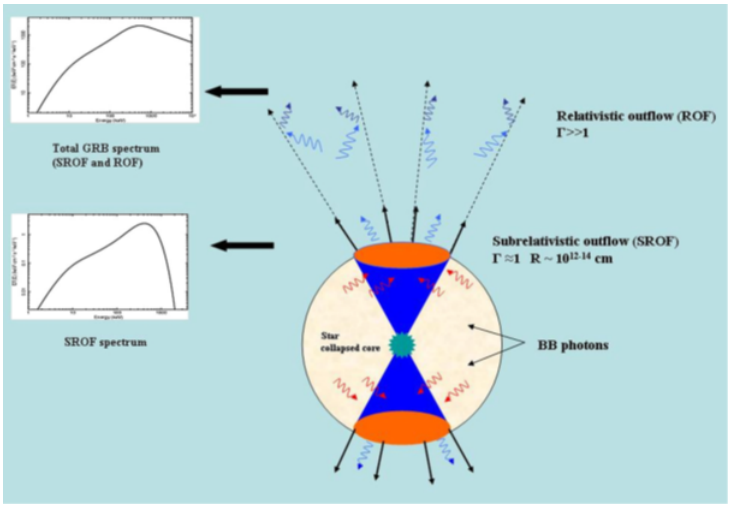

Figura 2.17: A sketch explaining the so called GRBCOMP model, in which we can see the Comptonization Cloud subrelativistically moving which up-scatters firstly the black-body photons of the photospheric phase and then these photons are up-scattered by the electrons of the relativistic jet [99].

Tabella 2.5: Results of the fit related to the second interval of GRB 080817 (the model used, the statistics adopted, DOF and software used).

	Model	Statistics	DOF	Software
(1)	BAND	$\chi^2_{red} = 1.05$	313	XSPEC
(2)	COMP	$\chi^2_{red} = 1.07$	313	XSPEC
(3)	COMP	$CSTAT/DOF = 1.04$	313	RMFIT

by a subrelativistic bulk outflow of thermal electrons, while the high-energy power-law tail above the energy peak of the model is obtained by photons up-scattered by relativistic jet electrons. In this case we need a relativistic treatment. This model was developed having in mind the "pair–instability" supernova as a possible progenitor of GRBs, but it is general enough to be applied to other scenarios. The basic idea behind these additional fits with GRBCOMP is to pass from the E_p – flux correlation to the correlation of flux with the physical parameters that determine the spectral peak energy. The fact that E_p may be determined by a combination of physical parameters and conditions may, in principle, explain both the dispersion of the correlation and the outliers found. In the GRBCOMP model, the peak energy E_p of the spectrum mostly depends on the electron temperature of the subrelativistic outflow of kT_e, a real physical parameter; it also involves other physical parameters such as the temperature of the seed blackbody spectrum kT_s, the radial optical depth of the subrelativistic outflow τ and the bulk outflow velocity of the thermal electrons β.

2.4.1 Results

In Tab. 2.6 and Tab. 2.7 we present a comparison of the values of E_p in specific intervals of two GRBs (i.e. GRB080817 and GRB 080916C) measured by Yu et al. with those estimated with my own analysis through XSPEC and RMFIT; the intervals here analyzed are the first ones and the last one; generally these intervals do not follow the correlation, as already said.
As we can see from the plot E_p–Flux in Fig. 2.18, in which we compare the results for GRB 080817 obtained through RMFIT and XSPEC with those achieved by Yu, we have added two points at the end of the burst, by extending the time interval of the burst up to 80 s; in fact, Yu et al. could constrain only the points up to 50 s. The extrinsic scatter of the fit

Tabella 2.6: Examples of values of E_p for some intervals of two GRBs (GRB 080817 and GRB 080916C) of Yu et al. catalog obtained by Yu et al. (2016) and those obtained through my analysis with XSPEC, with their own errors ("Int#" indicates the number of the interval as reported in [109]). In MOD1 we have fit the interval with Band function and χ^2 statistics adopted, in MOD2 with Band function and CSTAT statistics, in MOD3 with COMP model and χ^2 statistics, MOD4 refers to COMP model and CSTAT statistics. E_p is expressed in keV.

	Yu	MOD1	MOD2	MOD3	MOD4
GRB 080916C Int#3	594±89	316±41	364±7	399±52	454±7
GRB 080916C Int#23	312±74	242±66	321±24	316±91	427±37
GRB 080817 Int#2	668±79	444±60	618±18	527±12	646±12
GRB 080817 Int#3	512±23	323±40	442±36	372±29	622±29
GRB 080817 Int#15	347±87	168±49	132±25	200±30	189±30
GRB 080817 Int#16	-	127±62	132±41	134±45	139±32

realized by using data provided by Yu et al. is 0.08 ± 0.02, its coefficient of correlation is 0.54 with a chance probability equal to 0.03 (see Sec. 2.3), while the dispersion of the fit performed in this work through RMFIT and XSPEC (by adopting a χ^2 statistics in both cases) is < 0.03 and < 0.11, respectively, the coefficient of correlation is 0.69 and 0.73, respectively, and the chance probability is 0.002 and 0.001, respectively. Tab. 2.8 summarizes all these results.

So we have actually obtained an improvement of the fit: with respect to the analysis by Yu et al. 2016, the scatter of the E_p – flux correlation based on the results of my spectral analysis with RMFIT has been quite reduced, while the coefficient of correlation found with both XSPEC and RMFIT is better than that obtained with Yu et al. data.
Moreover, as we can note from the lightcurves for GRB 080817 (Fig. 2.19), we have achieved, with both RMFIT and XSPEC, a better tracking (with respect to that one obtained by Yu et al.) between the flux and the E_p in the first part of the observation, where the initial "jump" of the flux is better reproduced by E_p from my analysis (i.e. it has been increased); moreover, in (a) and (c) there is a sort of anticorrelation between E_p and flux in the first part of the burst, conversely in (b) we have actually obtained a good tracking; however, at the centre a bad tracking persists.
Finally, I have also extended the duration of the burst up to 80 s (Yu et al. arrived up to 50 s), because I was able to constrain the parameters of the

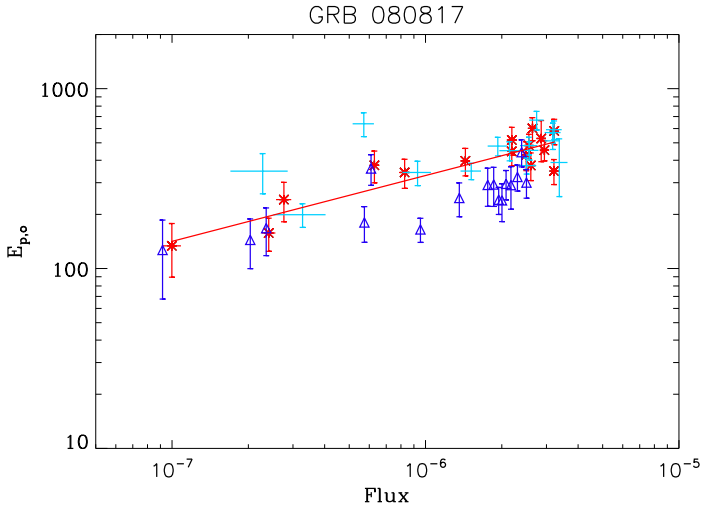

Figura 2.18: E_p–Flux correlation performed by Yu et al. and in my work with XSPEC and RMFIT for GRB 080817, by fitting the spectra with BAND model and by adopting the χ^2 statistics in both cases. The red points are obtained through RMFIT, the blue ones through XSPEC and the light blue ones by Yu et al. The red line is the fit of the correlation through Reichardt function only for RMFIT data. The points obtained through my analysis with RMFIT have a reduced scatter with respect to those obtained by Yu et al.

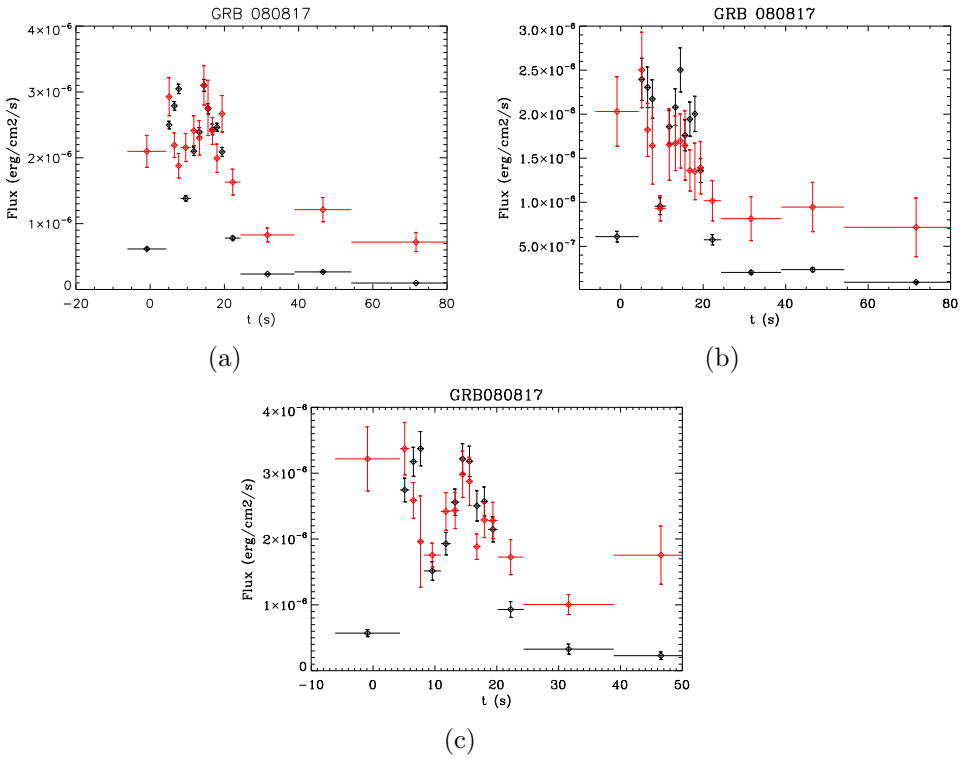

Figura 2.19: Temporal evolution of E_p and flux of GRB 080817. Black points represent the flux, red ones the E_p. We have obtained lightcurve (a) by fitting the spectra with BAND model and adopting the CSTAT statistics, (b) by fitting the spectra with BAND model and adopting a χ^2 statistics and (c) by using the spectral measurements provided by Yu et al. (2016).

Tabella 2.7: Examples of values of E_p for two GRBs (GRB 080817 and GRB 080916C) of Yu et al. catalog obtained by Yu et al. and those obtained through my analysis with RMFIT, with their own errors. The legend is the same of Tab. 2.6. E_p is expressed in keV.

	Yu	MOD1	MOD2	MOD3	MOD4
GRB 080916C Int#2	477±63	482±65	404±43	596±78	532±46
GRB 080916C Int#3	594±89	622±93	548±55	709±99	649±62
GRB 080916C Int#23	312±74	243±78	271±48	304±64	278±37
GRB 080817 Int#2	668±79	601±88	542±53	757±90	684±54
GRB 080817 Int#3	512±23	455±58	405±34	6432±69	568±39
GRB 080817 Int#15	347±87	241±59	224±34	279±62	261±35
GRB 080817 Int#16	-	133±44	133±26	138±33	133±18

Tabella 2.8: Comparison of results in terms of scatter, coefficient of Spearman and chance probability of the fits obtained for GRB 080817. MOD1 refers to the fit performed with Band function, χ^2 statistics and RMFIT software, while MOD2 refers to Band function, χ^2 statistics and XSPEC software.

	Yu	MOD1	MOD2
σ_{ext}	0.08 ± 0.02	< 0.03	< 0.11
Coefficient of correlation	0.54	0.69	0.73
Chance of probability	0.036	0.002	0.001

two last intervals. Noticeably, this extended analysis allowed us to find that the E_p-flux tracking holds also in the last part of the burst decay phase.
Finally, by using GRBCOMP model, we have plotted the kT_e – Flux correlation (see Fig. 2.20 related to the GRB 080916C). There is an evident correlation between the temperature of electrons and the detected flux, although there are less points (i.e. number of intervals considered) than those expected because we could not constrain many points. Because of the not-negligible dispersion of the data points, the two different lines indicating two different fit functions differ significantly: indeed, we can note that it is more reliable to fit the E_p – Flux correlation using the Reichardt function which accounts for the dispersion of the data (with respect to the Fitexy function); in this way the value of the slope is not biased by outlier points. Just to make a comparison, in Fig. 2.21 we show for GRB 080916C the E_p – Flux plot, obtained by Yu et al, whose spectra have been fitted with COMP model. We can sum up the results of these fits in the Tab. 2.9. We can note that

Tabella 2.9: Results of the fit of GRB 080916C with GRBCOMP model compared with those obtained by using Yu et al. data, in terms of σ_{ext}, chance probability and coefficient of correlation.

	Yu	Our analysis
σ_{ext}	0.17 ± 0.06	0.16 ± 0.05
Coefficient of correlation	0.26	0.32
Chance probability	0.27	0.27

by using GRBCOMP model the coefficient of correlation obtained is higher than that found with COMP model, although, actually, the dispersion of the kT_e – Flux correlation is not significantly lower than that of the E_p – Flux correlation: we have not significantly improved the estimate of the dispersion of the E_p – Flux correlation for GRB 080916C.

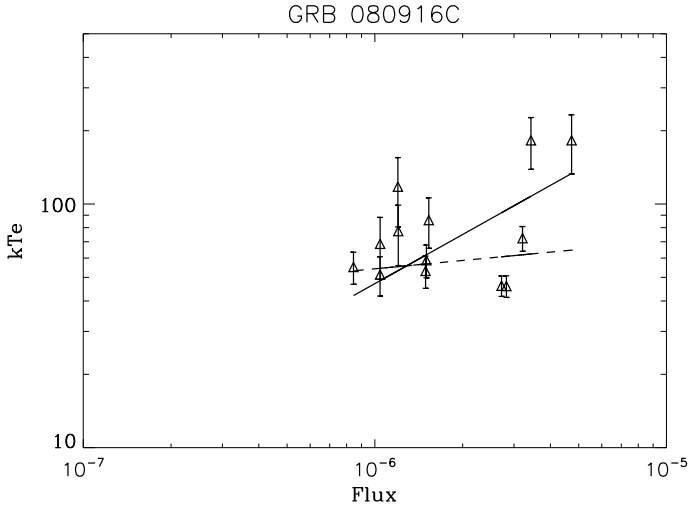

Figura 2.20: kT_e – Flux correlation of GRB 080916C performed in my work with XSPEC by fitting the spectra with GRBCOMP model and by adopting a χ^2 statistics. Solid line is the fit through Fitexy function, the dotted one through Reichardt function.

In summary, all the above analysis of Fermi/GBM data confirm that the time–resolved E_p – flux correlation holds for most GRBs and for a large fraction of their duration. However, due to sensitivity limitations of this instrument (despite the large energy band, the effective area is as small as $< 150\ cm^2$), no convincing conclusions, i.e., real or biased by background

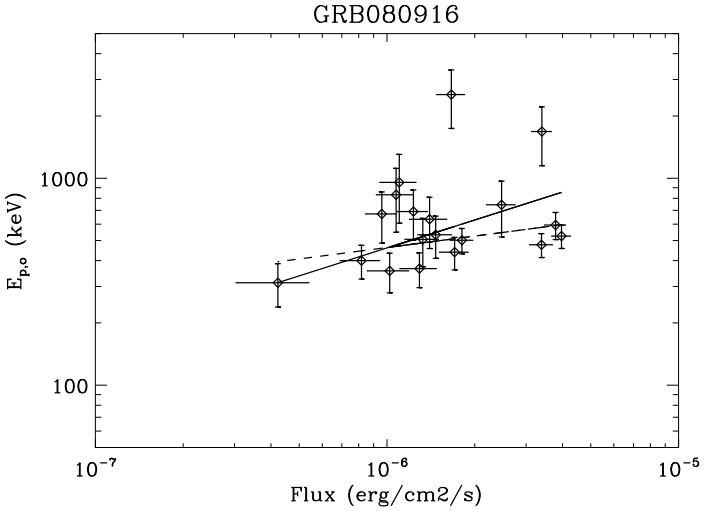

Figura 2.21: E_p–Flux correlation of GRB 080916C by selecting all the fits independently on the model used, a CSTAT/DOF<10, Δ_{E_p}/E_p=1 and the whole burst duration. Solid line is the fit through Fitexy function, the dotted one through Reichardt function.

subtraction and data analysis method, about the lack E_p – flux tracking especially during the rising phase of some GRBs can be drawn.

2.5 Analysis of CGRO/BATSE spectral catalog by Preece et al. 2000

As discussed in Section 2.2, compared to the Fermi/GBM, the CGRO/BATSE instrument had a much larger effective area (of the order of $\sim$2000 cm^2, thus allowing a sensitive spectral analysis for weaker GRBs and weaker (rise, decay, inter–pulse) emission phases within single GRBs. The drawback of using BATSE data is that the instrument was mostly operating before the "afterglow" era, thus there are only a very few BATSE GRBs with measured redshift. This is why BATSE data are not used to investigate E_p – "intensity" correlations like E_p – L_p or E_p – E_{iso} correlations. However, the aim of my work is to calibrate the slope and intrinsic dispersion of these correlaitons by using the internal E_p – flux correlation of GRBs, without the need of the redshift and in a way unbiased by cosmology or jet opening angle. Thus, in order to further investigate both the firmness and the characteristics of the correlation and the possible deviations especially diring the rising phase, as

resulting form the analysis of Fermi 7GBM data, we considered the time–resolved spectral analysis of bright BATSE GRBs performed by Preece et al. (2000).

They presented a spectroscopy catalog, completed on 1998 September 23^{rd}, describing the high time resolution spectral behavior of bright bursts as observed with BATSE on board the CGRO.

In order to obtain a reasonable time-resolved picture of the spectral evolution in individual bursts, they considered bright bursts. They chose bursts to analyze using peak flux and total fluence limits, where these were determined by the methods described in the BATSE burst catalogs [26], [75], [83]. For example, bursts with large peak flux may not have a large enough total fluence to be included in the sample by that criterion alone but may still have a considerable number of spectra with sufficient counts to be useful for spectroscopic analysis. The total fluence selection criterion is $4 \times 10^{-5} erg$ s cm^{-2} integrated over all energies (25–1800 keV).

For peak flux, the catalog value must exceed 10 photons $cm^{-2}s^{-1}$ on the 1024 ms integration timescale in the BATSE trigger energy band (50-300 keV). To avoid any bias, only bursts that had at least one of these catalog values available were selected.

The total duration of burst emission is selected by human judgement, usually starting with the first spectrum after the trigger.

Once the selection has been made, the spectra have been rebinned in time according to a signal-to-noise ratio (S/N) criterion, in order to have a sufficient count rate in each spectrum so that the spectral model parameters could be determined with reasonable accuracy.

To determine the S/N, the integrated background-subtracted count spectrum was compared with the total uncertainty, so the resulting measure is in units of standard uncertainty (σ). For LAD spectra over their total usable energy range, their minimum acceptable S/N was chosen to be 45, or roughly 2σ per energy resolution element in a hypothetical flat LAD count spectrum. For most bright bursts, the peak spectra have count rates that were well in excess of 45 σ, so it was typically the quiescent periods between peaks where spectra are binned together in this way. SD data were used in some unusual cases where the LAD data were missing or unacceptable because of the presence of electronic distortions from overly high count rates. For these data, the S/N used to rebin the spectra in time was 15. Any bin at the end of the burst selection interval is likely to have less than 45 σ, so it is dropped. For background modeling, low-order (about 4) polynomial behavior have been

assumed.
They rejected bursts that had less than eight spectra in total after the rebinning to ensure that enough spectra were available to track spectral evolution through each burst. After all the criteria have been applied to the entire BATSE data set from the beginning of the mission until 1998 September 23^{rd}, 156 bursts are available for this catalog (see Fig. 2.22).

General Characteristics of Catalog Bursts

Burst Name[a] (1)	Trigger Number (2)	Data Type (3)	Detector Number[b] (4)	Model Used[c] (5)	Number of Spectra (6)	Time Interval Start (s) (7)	Time Interval Stop (s) (8)	Peak Flux[d] (photons cm^{-2} s^{-1}) (9)	Fluence[d] (ergs cm^{-2}) (10)
3B 910421.....	105	HERB	7	GRB	14	0.064	10.304	27.6	8.2E−6
3B 910425.....	109	CONT	4	GRB	14	−16.384	53.248	4.7	4.8E−5
3B 910503.....	143	HERB	6	GRB	27	0.704	4.800	142.7	7.9E−5
3B 910522.....	219	MER	456	BPL	51	105.499	135.963	33.1	3.5E−5
3B 910601.....	249	HERB	2	GRB	15	0.0	17.856	28.1	2.1E−5
3B 910619.....	394	HERB	1	GRB	34	0.0	44.480	7.6	4.1E−5
3B 910627.....	451	HERB	4	GRB	16	0.0	11.968	21.9	1.5E−5

Figura 2.22: A schematic view of the Preece et al. catalog.

The fluences have been calculated by integrating the individual spectral model fits over the total fitted energy range (typically 25-1800 keV for LAD data) and summing over all spectra (as binned) in the time interval selected, which generally differs from the interval chosen for the BATSE burst catalog fluences. By using the best-fit model for each spectrum, this value represents a fair estimate of the fluence.

We have performed the same analysis made in Sec. 2.3; firstly (scheme A), we have found that most of the GRBs follow quite well the correlation, i.e. there is a good tracking between E_p and the flux, although a not-negligible extra-statistical scatter was still present. Nevertheless, we have found some GRBs in which some points do not follow the correlation, in particular at the beginning and at the end, as for the Fermi/GBM. Thus, in order to get an improvement, we have decided to further refine the selection of GRBs by applying the scheme B and thereafter the scheme C in which, differently from the Sec. 2.3, we have considered only the fits with model Band, $CSTAT/DOF < 1.3$, $\Delta_{E_p}/E_p < 0.5$ and the whole burst duration. Actually, in this way the scatter has been quite reduced with respect to the first scheme. Moreover, here we have added another scheme that we call scheme D, in which we have selected only the fits with Band model, with a value of $CSTAT/DOF < 1.3$, a value of $\Delta_{E_p}/E_p < 0.5$ and by considering only the

second part of the burst duration. Tab. 2.10 summarizes the schemes used in this section.

Tabella 2.10: Summarizing scheme for our analysis.

	Scheme A	Scheme B	Scheme C	Scheme D
Model	All	All	Band	Band
CSTAT/DOF	< 10	< 10	< 1.3	< 1.3
Δ_{E_p}/E_p	< 1	< 1	< 0.5	< 0.5
Duration of the burst	100%	50%	100%	50%

Similarly to Sec. 2.3, for each subgroup of GRBs we have plotted the histograms of the distribution of the extra-statistical scatter, obtained through the Reichardt function alone, and both the distributions of the slope, obtained through both Fitexy and Reichardt functions, all fitted with a Gaussian function.
As previously stated (Sec. 2.3), the mean value of the slopes and the scatter obtained through Fitexy and Reichardt functions are arithmetic means and the errors associated have been calculated through the propagation of errors.

2.5.1 Results

As for Yu et al. catalog, firstly, we have applied the scheme A, and we have found that most of the GRBs follow quite well the correlation, i.e. in their lightcurves there is a good tracking between E_p and the flux, although a not-negligible extra-statistical scatter is still present, as we can see, e.g., for GRB 940302, in Fig. 2.23 ($\sigma_{ext} = 0.18 \pm 0.13$); we have found also a coefficient of correlation of 0.67 and a chance probability of 1.10×10^{-6} (by considering 42 time intervals). By considering, instead, only the second half of the burst duration (scheme B), we have obtained an improvement in the plot because the scatter is further reduced with respect to the previous scheme, and the behavior of the flux is similar to that one of E_p, as we can see, e.g. for GRB 940302 in Fig. 2.24. Here we have found a scatter of 0.04 ± 0.01, a coefficient of correlation of 0.83 (higher than that found in scheme A) and a chance probability of 2.31×10^{-6} (by considering 21 time intervals). So in this scheme we have actually improved the fit with respect to the previous scheme A.
Moreover, if we apply the scheme C, we can notice that the scatter has been

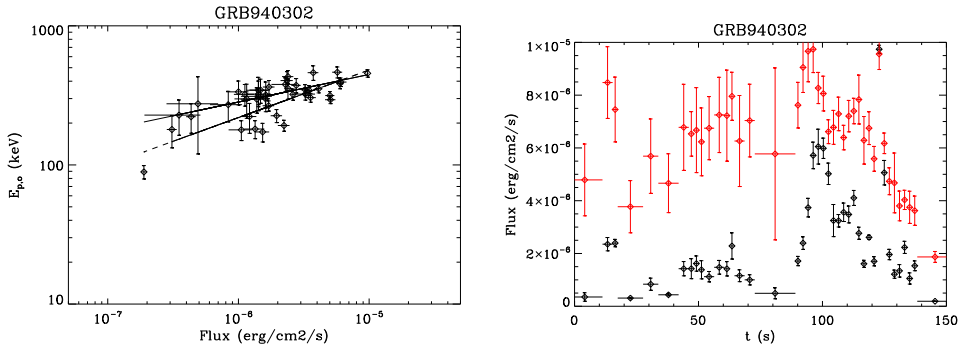

Figura 2.23: Left panel: the E_p–Flux correlation of GRB 940302 by selecting the scheme A; right panel: the corresponding temporal evolution of E_p and Flux. The legend is the same of the Fig. 2.5. We can note that there is a not-negligible dispersion in the correlation.

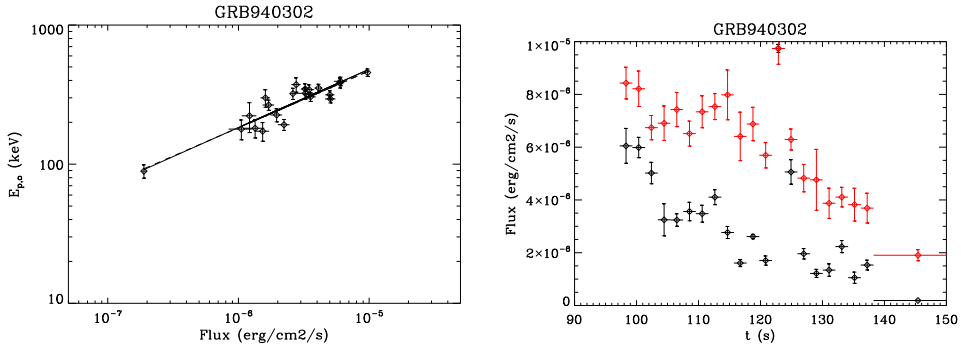

Figura 2.24: Left panel: the E_p–Flux correlation of GRB 940302 by selecting the scheme B; right panel: the corresponding temporal evolution of E_p and Flux. The legend is the same of the Fig. 2.5. We can note that the scatter has been reduced.

considerably reduced (with respect to the results obtained in the scheme A), as we can see, e.g. for GRB 940302 (see Fig. 2.25). For this fit we have found a scatter of 0.07 ± 0.01, a coefficient of correlation of 0.72 and a chance probability of 5.72×10^{-5} (by considering 24 time intervals).

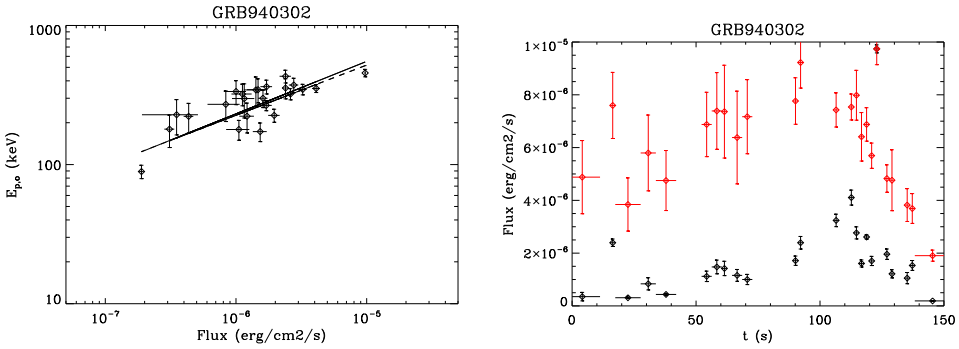

Figura 2.25: Left panel: the E_p–Flux correlation of GRB 940302 by selecting the scheme C; right panel: the corresponding temporal evolution of E_p and Flux. The legend is the same of the Fig. 2.5. We can note that the scatter has been reduced with respect to scheme A.

Finally, if we apply the scheme D, we can notice a further improvement of the results obtained (e.g., with respect to those obtained in the scheme A), as we can see, e.g. for GRB 940302, in Fig. 3.2. For this fit we found a scatter < 0.27 (here we can derive just an upper limit because of the lower number of time intervals considered), a coefficient of correlation of 0.93 (the highest one with respect to those found in all the previous schemes) and a chance probability of 1.17×10^{-5} (by considering 12 time intervals). All these results are shown in Tab. 2.11. Then we have investigated the distributions of the

Tabella 2.11: Values of the scatter, coefficient of correlation, number of time intervals considered and chance probability obtained through the fit of the correlation for scheme A, B, C and D for GRB 940302.

GRB940302	Scheme A	Scheme B	Scheme C	Scheme D
Coefficient of correlation	0.67	0.83	0.72	0.93
σ_{ext}	0.18 ± 0.13	0.04 ± 0.01	0.07 ± 0.01	< 0.27
N° of time intervals	42	21	24	12
Chance probability	1.10×10^{-6}	2.31×10^{-6}	5.72×10^{-5}	1.17×10^{-5}

slope of the correlation, obtained through Fitexy and Reichardt function fits

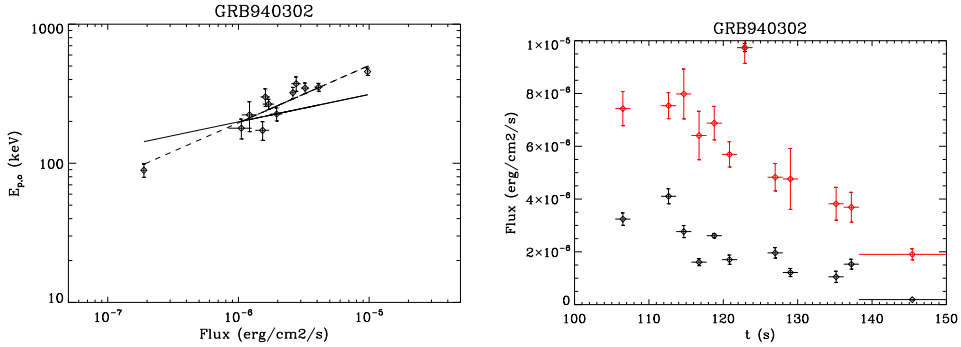

Figura 2.26: Left panel: the E_p–Flux correlation of GRB 940302 by selecting the scheme D; right panel: the corresponding temporal evolution of E_p and Flux. The legend is the same of the Fig. 2.5. We can note that the scatter has been reduced with respect to the scheme A.

(Fig. 2.27 and Fig. 2.28, respectively) and of the scatter of the correlation obtained through Reichardt function fits (Fig. 2.29), for each subgroup of GRBs. In these histograms, as in Sec. 2.3, some "outliers" are present, whose nature needs to be still investigated.

Tab. 2.12 summarizes the results of the distributions, showing the mean arithmetic values and their errors, obtained through the propagation of the errors, of both the slopes achieved through the two different fits and the scatter obtained through Reichardt function.

The behavior of the slope and the extra-Poissonian scatter distributions are the same of those found with Yu et al. catalog analysis, i.e. the value of the slope (in both cases) is close to that one obtained through the time-integrated (averaged) analysis, i.e. ~ 0.5, and the value of the extrinsic scatter is always lower than 0.2. Moreover, we can notice that the dispersion has been quite reduced by considering, for example, only the second part of the burst (see also Tab. 2.11). We can state that the results obtained by

Tabella 2.12: Mean arithmetic values of the slopes and of the scatter, with their errors, obtained through Fitexy and Reichardt functions for scheme A, B, C and D.

	Scheme A	Scheme B	Scheme C	Scheme D
m_{fitexy}	0.47±0.01	0.49±0.02	0.47±0.01	0.47±0.01
m_{Reich}	0.56±0.02	0.66±0.13	0.450±0.007	0.53±0.01
σ_{ext}	0.072±0.008	0.06±0.01	0.081±0.009	0.05±0.001

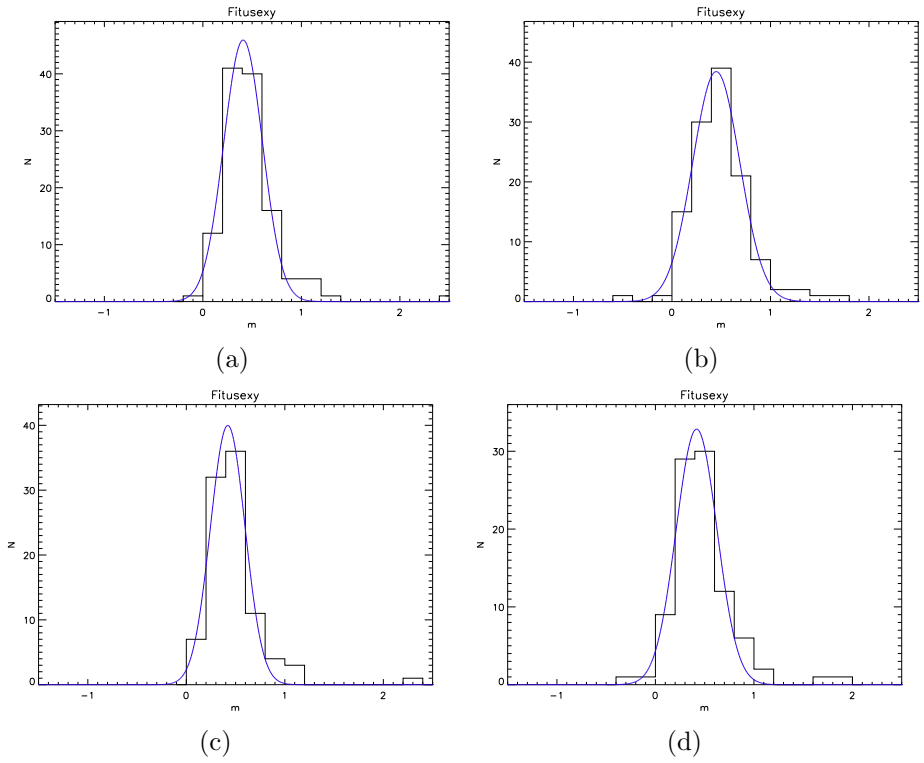

Figura 2.27: Distribution of the slope of the correlation obtained through Fitexy function fit using a Gaussian for the scheme (a) A, (b) B, (c) C and (d) D.

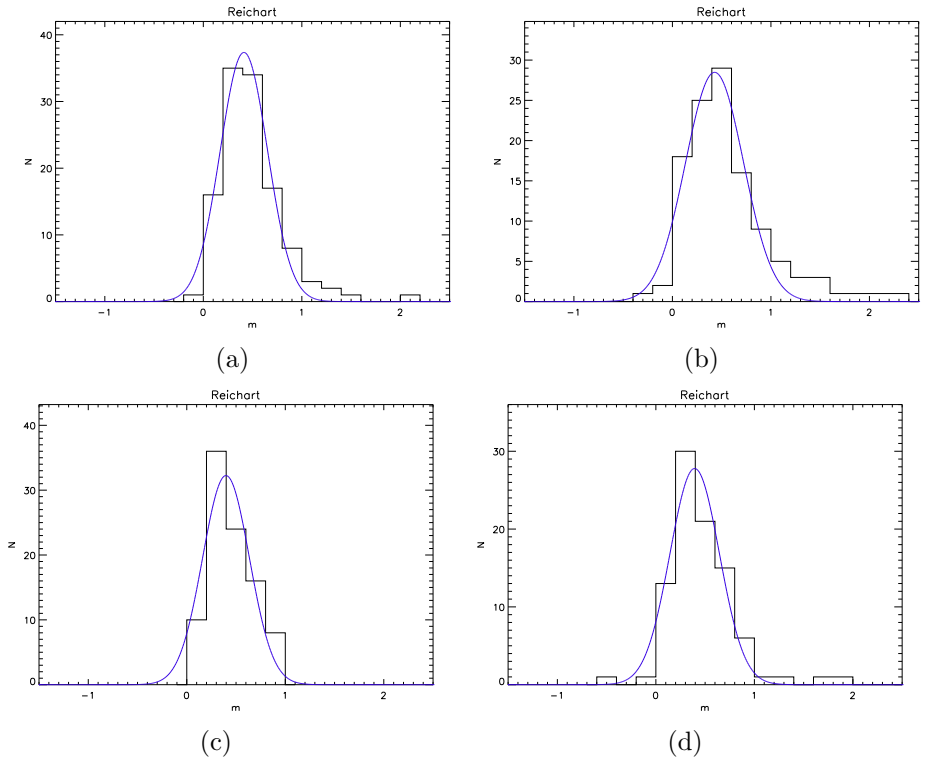

Figura 2.28: Distribution of the slope of the correlation obtained through Reichardt function fit using a Gaussian for the scheme (a) A, (b) B, (c) C and (d) D.

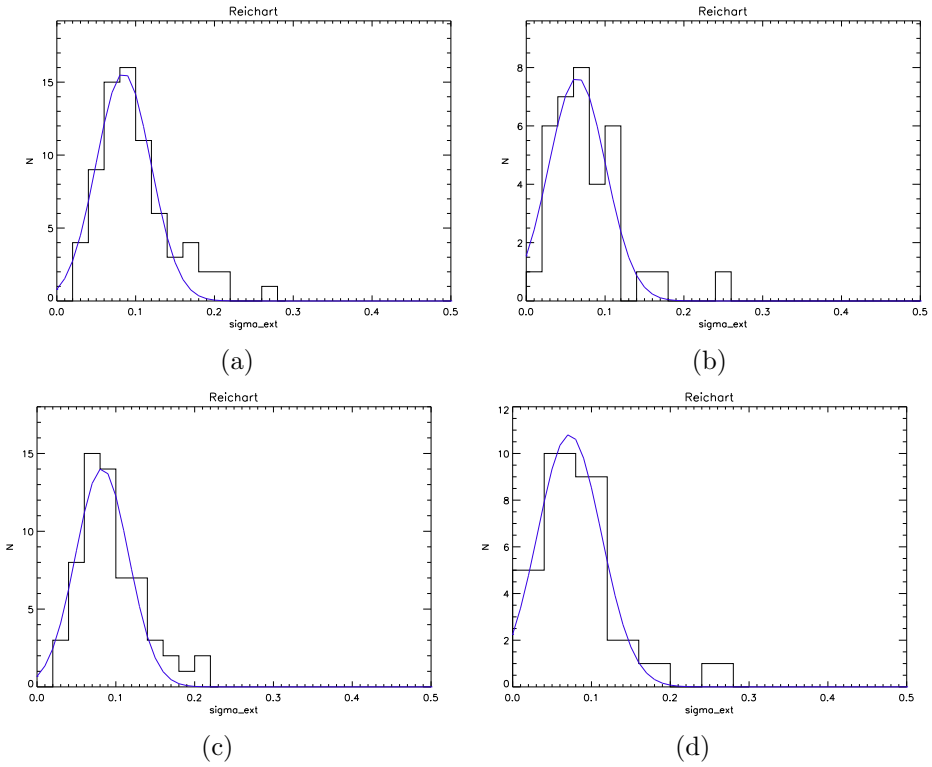

Figura 2.29: Distribution of the dispersion of the correlation obtained through Reichardt function fit using a Gaussian for the scheme (a) A, (b) B, (c) C and (d) D.

using spectral measurements by CGRO/BATSE are even more refined with respect to those obtained in Sec. 2.3; indeed, the distributions of the slopes are narrower than those obtained in Yu et al. GRBs analysis (see also Tab. 2.2).
The results found in this section are actually confirmed by those obtained in the previous section (see Sec. 2.3), that is, although there is a not-negligible dispersion of the $E_{p,i}$ – "Intensity" correlation, both the slope and the scatter would basically converge to precise values, i.e. $m \sim 0.5$ and $\sigma_{ext} \sim 0.1$, by confirming again that the $E_{p,i}$ – "Intensity" is valid for all GRBs.
Then, we have performed the same analysis made for the Yu et al. catalog by fitting simultaneously, with the Reichardt function, the $E_{p,i}$ – Flux for all the GRBs present in Preece et al. catalog (see sec. 2.3). The results of this procedure are shown in Tab. 2.13 (errors are shown at 1 σ).

Tabella 2.13: Mean results of slope and dispersion obtained through the simultaneous fit of the correlation with the Reichardt function for scheme A, B, C and D.

	Scheme A	Scheme B	Scheme C	Scheme D
m_{Reich}	0.479±0.009	0.490±0.009	0.477±0.009	0.48±0.01
σ_{ext}	0.093±0.005	0.070±0.005	0.100±0.005	0.07±0.05

We have decided to use the results obtained in this section for our cosmological analysis (see Sec. 3.3). The main reason of our decision concerns the higher accuracy of the spectral measurements made by the BATSE instrument with respect to those obtained by GBM having a lower sensitivity and affected by a more critical background subtraction. Thus, on the one side the highest accuracy and largest number of BATSE spectra allow a reliable characterization of the E_p – flux and, thus, of the E_p – "intensity", correlation, providing strong evidence of a slope of ∼0.5 and intrinsic scatter lower than 0.1. These are very important inputs for both models of GRB physics and for the use of GRBs for measuring cosmological parameters (as will be discussed in next chapter). On the other side, it could be pointed out that the lack of tracking during the rising phase of some GRBs may be only partly ascribed to background subtraction or data analysis issues, and has to be explained by GRB models.

Capitolo 3

Discussion and implications

The results of our analysis provide an important characterization of the E_p – "Intensity" correlation for GRBs through time-resolved spectroscopy.
We have provided unbiased estimates of the slope and the scatter, i.e. values not affected by the cosmology or any other problem related to the jet opening angle. Moreover, the present analysis has confirmed that in some GRBs and in some phases (in particular at the beginning and at the end of the burst) there is no tracking between the flux detected and E_p, i.e. there is no correlation between these two parameters, beyond any background subtraction problems (see also [88]).
Time-resolved analysis results have an important impact for the understanding the prompt emission physics, the distribution of the jet opening angles and can be used for GRB cosmology. In this chapter we will discuss some of these implications that have to be investigated further.

3.1 Physics of the prompt emission

3.1.1 The slope of the E_p – Intensity correlation

As we have already said, the physics of the prompt emission is still an unresolved issue. There are many physical models which can explain its emission physics, such as the standard fireball scenario or the Poynting flux scenario, and each of them involves different emission mechanisms, e.g., SSM (synchrotron shock model), internal shocks, inverse-Compton dominated internal shocks, SSM external shocks and photospheric emission dominated models;

moreover, we do not know in detail about the degree of magnetization of the jet and about the regions where such emission mechanisms could occur. For all these models, E_p is a key parameter, as we can see in the table Fig. 3.1 presented by Zhang et al. (2002) [110], in which E_p assumes different values for different models. The existence of Amati relation can be a fundamental input for further investigating on these open issues.

MODEL PREDICTIONS FOR E_p

Models	Subcategories	E_p	Comments
Internal models	Low σ: internal shocks	$\propto \epsilon_{e,3} L^{1/2} \Gamma^{-2} t_v^{-1} (1+z)^{-1}$	$\gamma_e^{(1)}$ relevant
	High σ: magnetic dissipation	$\propto \epsilon_{e,5} \Gamma (1+z)^{-1}$	$\gamma_e^{(2)}$ relevant
	Pair photosphere	$\propto \Gamma T'_{\pm} / r_{\pm}^{\prime 2} (1+z)^{-1}$	Comptonized spectrum
External models	Low σ: external shocks	$\propto \epsilon_{e,6} \Gamma^4 n_{\rm ext}^{1/2} (1+z)^{-1}$	B generated in situ
	High σ: plasma-barrier interaction	$\propto \epsilon_{e,7} \Gamma^{8/3} L^{1/2} E^{-1/3} n_{\rm ext}^{1/3} (1+z)^{-1}$	B carried from the wind
Innermost models	$\eta < \eta_{c1} \sim 250(1+\sigma)^{-1/5}$	$\propto L^{-5/12} t_{v,m}^{1/6} \Gamma^{8/3} (1+z)^{-1}$	Wind coasting regime
	$\eta_{c1} < \eta < \eta_{c2}$	$\propto L^{-1/12} t_{v,m}^{1/6} \Gamma (1+z)^{-1}$	Shell coasting regime
	$\eta > \eta_{c2} \sim 10^4 (1+\sigma)^{-1/3}$	$\propto L^{1/4} t_{v,m}^{-1/2} (1+z)^{-1}$	Shell acceleration regime

Figura 3.1: Model predictions for E_p for different physics models proposed [118].

Now we discuss what the value of the slope ~ 0.5 would predict.
Both $E_{p,i}$ and E_{iso} are linked to the fireball bulk Lorentz factor, Γ, in a way that it varies in each scenario, and the existence and properties of the $E_{p,i}$ – E_{iso} correlation allow us to constrain the range of values of the parameters (see e.g. [118]; [96]). As shown by e.g. [118], [93] and [91], for a power-law electron distribution generated in an internal shock within a fireball with bulk Lorentz factor Γ, it is possible to derive the relation $E_{p,i} \propto \Gamma^{-2} L^{1/2} t_\nu^{-1}$, where L is the bolometric GRB luminosity and t_ν is the typical variability time-scale. In order to produce the observed $E_{p,i}$ – E_{iso} correlation, the above formula would require that Γ and t_ν are approximately the same for all GRBs, an assumption which is difficult to justify. The situation becomes even more complicated if one takes into account that the models generally assume $L \propto \Gamma^\beta$, with the value of β (the high-energy spectral index) varying in each scenario and typically being $\sim 2-3$ [118], [96], [90], [93].
An interesting possibility, which is currently the subject of many theoretical works, is that a substantial contribution to prompt radiation of GRBs comes from direct or Comptonized thermal emission from the photosphere of the fireball [118], [90], [91]. This could explain the very hard spectra observed at the beginning of several events [31], [87], [38]), inconsistent with SSM models, and the smooth curvature characterizing GRBs average spectra. In this scenarios, $E_{p,i}$ is mainly determined by the peak temperature T_p of blackbody-

distributed photons and thus naturally linked to the luminosity or radiated energy. For instance, for Comptonized emission from the photosphere one can derive the relations $E_{p,i} \propto \Gamma T_p \propto \Gamma^2 L^{-1/4}$ or $E_{p,i} \propto \Gamma T_p \propto r_0^{-1/2} L^{1/4}$ (where r_0 is the radius at which the emission begins), depending on the assumptions [91]. Also in this case the $L \propto \Gamma^\beta$ relation plays a decisive role. As shown by Rees and Meszaros (2005) [91], in this scenario the correct $E_{p,i}$ – E_{iso} relation can be obtained for some specific physical conditions just below the photosphere.

Instead, according to Ghirlanda et al. (2009), if the emission is due to synchrotron process, the energy at the peak should be $E_p \propto B\Gamma\gamma_p^2$, where γ_p^2 is the Lorentz factor of the electrons emitting at the peak and $L \propto NB^2\gamma_p^2$, with N being the number of electrons having γ_p. Therefore, a change of the quantity ΓB, maintaining the same γ_p and N, would give $E_p \propto L^{1/2}$. The prompt emission almost surely occurs in the fast cooling regime, implying that the resulting synchrotron spectrum cannot be harder than $L(E) \propto E^{-1/2}$ (Ghisellini et al., 2000), while Ghirlanda et al. (2009) [42] (see also [87], [44]) observe also in Fermi GRBs much harder spectra. In particular, Ghirlanda et al. (2009) [42] found that there is the same E_p – L_{iso} correlation during the rise and the decay phase of different intervals in the same GRB. Also quasi-thermal Comptonization could well explain that E_0 correlates with L. Moreover, we have to mention the work of Nava et al. 2006 [79], in which they corrected the E_p – L_{iso} correlation for the jet angle and found a value of the slope $\sim 0.7-1$. Our result (slope ~ 0.5), not affected by any uncertainty related to the opening jet angle, confirms that correction for the angle made by Nava et al. is not so reliable.

We have to consider also the work of Preece et al. 2013, in which they analyzed the extremely bright GRB 130427A and derived from the data a value of the slope ~ 0.7. This result could be explained by a model based on an expanding fluid element rather than a colliding shell, in which synchrotron emission occurs, and naively assuming that the magnetic flux is frozen in the flow, they derive this correlation $E \propto L^{2/3}$, not consistent with our results based on a statistical analysis of many GRBs, thus we can conclude that the scenario presented by Preece et al. may work for specific cases but not for the majority of GRBs.

3.1.2 The "Rising" phase of a GRB lightcurve

Each of the models used to explain the prompt emission of GRBs makes different predictions regarding E_p evolution within a burst. The data can be used to constrain each different model. In all of the models, E_p is a function of luminosity and Lorentz factor Γ.
One common feature found in each models is that when an emission stops abruptly, the observed emission is the high-latitude emission from the jet, due to the curvature of the conical jet (e.g., [24]; [58]; [19]; [67]; [89]; [113]). During this "curvature effect" [1], an "intensity-tracking" behavior is expected (i.e. there is good tracking between E_p and the flux). Observationally, both "hard-to-soft" evolution (i.e. there is no good tracking between E_p and the flux) and intensity-tracking show decreasing E_p with decaying flux, generally consistent with the "curvature-effect" explanation.
In our analysis we have found that some GRBs do not follow the correlation in the rising phase (see GRB 080817); a possible deviation at the end of the burst is more uncertain and needs further investigation. This result confirms what Lu et al. (2012) [72] have found; they pointed out that the E_p – Flux correlation is tighter in the decay phase of the GRBs, suggesting that the correlation in the decaying phase may be the main source of the global internal E_p – Flux correlation reported by Liang et al. (2004) (see also [25], [32]). More specifically, during the decay phase, one has the typical frequency $E_p = DE'_p/(1+z)$ and the bolometric luminosity $L_{iso} = D^{\varepsilon} L'_{iso}$, where D is the Doppler factor, the prime values are measured in the comoving frame, and the value of ε takes 3 for a continuous jet and 4 for an impulsive blob. The expected E_p – Flux relation slope would be roughly between 1/2 and 1/3.
The E_p evolution during the rising phase of a pulse carries further key information needed to diagnose different prompt emission models. In the standard synchrotron model (valid for internal shocks and internal magnetic dissipation models), one can write $E_p \propto \gamma_e^2 L^{1/2} R^{-1} (1+z)^{-1}$, where L is the bolometric "wind" luminosity of the ejecta, γ_e is the typical electron Lorentz factor in the emitting region, and R is the radius at which emission begins [72]. Naively, this would give a intensity-tracking behavior, since $E_p \propto L^{1/2}$.

[1] The curvature effect is a sudden decrease of jet emissivity; indeed we perceive very fast drops of X-ray flux a few hundred seconds after the trigger time because the simultaneous drop of emissivity at different angles from the line of sight is detected at different times [21].

Conversely, in order to explain an hard-to-soft behavior in the rising phase, Zhang and Yan (2011) [116] proposed a GRB prompt emission model invoking a sudden discharge of magnetic energy through turbulent magnetic reconnection, triggered by multiple internal collisions among magnetically dominated shells, the so called ICMART model. It also attributes GRB prompt emission to the synchrotron emission of electrons. However, an additional dependence of γ_e on the magnetization factor σ is invoked. Since σ is expected to drop with time during an ICMART event, the dissipated magnetic energy is expected to be shared by an increasing number of electrons, such that the γ_e drops with time as the number of electrons increases. As a result, a hard-to-soft evolution during the pulse-rising phase is expected, although detailed numerical calculations are needed to validate this prediction.
Finally, the dissipative photosphere model [91], [84], [37],[7], [61], [53], [101], [94] attributes E_p to the temperature of the photosphere. Naively, a quasi-thermal nature of emission generally calls for an intensity-tracking behavior, since hot temperature tends to be brighter. However, the temporal evolution of the Lorentz factor, the optical depth, and the radius of the photosphere may complicate the picture, requiring detailed modeling (e.g., [18], in preparation).
In conclusion, radiation models can account for both hard-to-soft evolution (ICMART model) and intensity tracking (internal shocks and probably photosphere), although detailed theoretical modeling in all these cases is desirable. The difficulty for each of these models is that both evolutionary trends can coexist in different pulses of the same burst. Therefore, one has to invoke multiple models to interpret different pulses in the same burst. This may happen if the composition of a jet varies with time in the same burst, i.e., the magnetization parameter σ can switch from > 1 to < 1 within the same burst. This is not impossible (Zhang 2011) since, given the same magnetic field strength at the central engine, a variation in baryon loading can cause a large fluctuation of the σ value.

3.1.3 The dispersion of the E_p – Intensity correlation

In addition to the existence and slope, also the extra-Poissonian dispersion of the $E_{p,i}$ – "Intensity" correlation is an important source of information. While the correlation is very highly significant, the scatter of the data around the best-fitting power law exceeds that expected by statistical fluctuations alone.

Amati et al. (2006) [2], by fitting with a Gaussian the dispersion of the central values of $\log(E_{p,i})$ around the best-fitting model, found $\sigma_{E_{p,i}} \sim 0.2$, while by fitting the whole data with the method by D'Agostini (2005) [16], which includes sample variance directly in the model, they obtained $\sigma_{E_{p,i}} = 0.15-0.2$. A similar scatter is found for the $E_{p,i}$ – L_{iso} and $E_{p,i}$ – $L_{p,iso}$ correlations (see e.g. [40]).

The result of our analysis of the E_p – Flux correlation within single GRBs is that the intrinsic E_p – L correlation has a dispersion ~ 0.1, i.e. half of that obtained by putting all together GRBs with measured redshift in the E_p – L or E_p – E_{iso} plane [2], [3], [108], [72]. By omitting the uncertainties coming from cosmology, we can say that almost the half of the measured dispersion of the E_p – E_{iso} or E_p – L correlation is due to jet opening angles (see section 3.2).

Other contribution to the scatter of the $E_{p,i}$ – E_{iso} correlation may come from viewing angle effects (e.g. [65]), the dispersion of the parameters of the fireball and/or of the time-scales, the inhomogeneous structure of the jet (e.g. [100]), the possible presence of significant amount of material in the circumburst region, that would affect the estimates of both E_{iso} and $E_{p,i}$ with a global qualitative effect of steepening the correlation and increasing its dispersion. When investigating the above physical interpretations and implications, it is important to take into account that at least part of the dispersion of the $E_{p,i}$ – E_{iso} correlation could arise from instrumental and other systematic effects in the estimates of $E_{p,i}$ and E_{iso} and their uncertainties. As discussed by Lloyd, Petrosian and Mallozzi (2000) [70] and Lloyd and Petrosian (2002) [69], data truncation effects, i.e. the systematics introduced by the limited energy band of the detector, may affect significantly the estimate of $E_{p,obs}$. Unless the energy band extends from a few keV to a few MeV, only a portion of the spectrum can be detected by a single instrument, which may cause a bias in the estimate of the spectral parameters. Concerning E_{iso}, the main source of possible systematics is the extrapolation to the 1-10000 keV cosmological rest-frame energy band of the spectral model obtained by fitting data in the observed energy band. In addition, the typical choice of computing E_{iso} in this rest-frame energy band may not be optimal for very soft events with values of $E_{p,i}$ below a few tens of keV, for which this method can likely lead to an underestimate of E_{iso}.

The dispersion ~ 0.1 is a very challenging observational evidence for the models, specially for the internal shocks models. For instance, Mochovitch et al. (2015) [78] developed a toy model where internal shocks are limited to

the collision of only two shells, and they found a value of the dispersion equal to ~ 0.3. In all cases, the dispersion of the intrinsic $E_{p,i}$ – E_{iso} correlation (i.e. by excluding instrument threshold), predicted by the internal shocks models, is higher than observed. A value of the dispersion ~ 0.1 could be better explained by Poynting flux dominated models in which synchrotron emission occurs because of effects of magnetic reconnection.

3.2 Jet opening angles

As discussed in the previous section, the dispersion of E_p – flux correlation (~ 0.1) indicates that almost half of the dispersion of E_p – E_{iso} correlation is due to the distribution of the jet opening angles. In this way, we can obtain information on the distribution of these angles by exploiting GRBs correlations.
Intriguingly, the $E_{p,i}$ – E_γ correlation shows a dispersion of the order of $\sigma_{E_{p,i}} \sim 0.1$ [39], [79], even if this correlation is based on a low number of events; moreover, it requires an estimate of t_b (time break) in addition to $E_{p,obs}$ and z, and it depends on jet model and circumburst environment properties (density, distribution).
The existence of both the $E_{p,i}$ – E_{iso} and $E_{p,i}$ – E_γ correlations is due to the fact that the collimation angles of GRBs are distributed over a relatively narrow range of values; the lower dispersion of the $E_{p,i}$ – E_γ correlation indicates that, at least, part of the scatter of the $E_{p,i}$ – E_{iso} correlation is due to the dispersion of jet opening angles. The comparison of the properties of the two correlations has been used, in addition to the study of the relation between jet opening angle and radiated energy, to infer the distribution of jet opening angles, as done by Ghirlanda, Ghisellini and Firmani (2005c) [45], Bosnjak et al. (2006a) [10] and Donaghy (2006) [20]. The validity of the $E_{p,i}$ – E_{iso} correlation from the most energetic GRBs to XRFs confirms that these two phenomena have the same origin and is a very challenging observable for GRB jet models. These models need to explain not only how E_{iso} and $E_{p,i}$ are linked to the jet opening angle, θ_{jet}, and/or to the viewing angle with respect to the jet axis, θ_ν, but also how E_{iso} can span over several orders of magnitudes. In the simple scenario of the uniform jet model [30], [60] jet opening angles are variable and the observer measures the same value of E_{iso} independently of θ_ν. In the other popular scenario, the universal structured jet model (e.g. Rossi, [92]), E_{iso} depends on θ_ν. In the hypothesis

that achromatic breaks found in the afterglow light curves of some GRBs with known redshift are due to collimated emission, it was originally found ([30], [8]) that the collimation corrected radiated energy, E_γ , is of the same order ($\sim 10^{51}$ erg) for most GRBs and that $E_{iso} \propto \theta_{jet}^{-2}$, assuming a uniform jet. In the case of structured jet models, which assume that θ_{jet} is similar for all GRBs (hence this scenario is also called universal jet model) the same observations imply that $E_{iso} \propto \theta_\nu^{-2}$. Thus, under the assumption of a nearly constant E_γ, the found $E_{p,i}$ – E_{iso} correlation implies $E_{iso} \propto \theta_{jet}^{-1}$ and $E_{iso} \propto \theta_\nu^{-1}$ for the uniform and structured jet models, respectively. Lamb et al. (2005) [60] argued that the universal structured jet model, in order to explain the validity of the $E_{p,i}$ – E_{iso} correlation from XRFs to energetic GRBs, predicts a number of detected XRFs several orders of magnitude higher than the observed one ($\sim 1/3$ than that of GRBs). In their view, the uniform jet model can overcome these problems by assuming a distribution of jet opening angles $N(\theta_{jet}) \propto \theta_{jet}^{-2}$. This implies that the great majority of GRBs have opening angles smaller than ~ 1 deg and that the true rate of GRBs is several orders of magnitude higher than observed and comparable to that of SN Ic.

Zhang et al. (2004) [111] show that the requirement that most GRBs have jet opening angles less than ~ 1 deg, needed in the uniform jet scenario in order to explain the $E_{p,i}$ – E_{iso} correlation, implies values of the fireball kinetic energy and/or of the interstellar medium density much higher than those inferred from the afterglow decay lightcurves. Similarly to other authors (e.g. [71]; [17]), they propose a modification of the universal structured jet model, the quasi-universal Gaussian structured jet. In this model, the measured E_{iso} undergoes a mild variation for values of θ_ν inside a typical angle, which has a quasi-universal value for all GRBs/XRFs, whereas it decreases very rapidly (e.g. exponentially) for values outside the typical angle. In this way, the universal structured jet scenario can reproduce the $E_{p,i}$ – E_{iso} correlation and predict the observed ratio between the number of XRFs and that of GRBs.

Of particular interest are the off-axis scenarios, in which the jet is typically assumed to be uniform but, due to relativistic beaming and Doppler effects, for $\theta_\nu > \theta_{jet}$ the measured emissivity does not sharply go to zero and the event is detected by the observer with E_{iso} and $E_{p,i}$ dropping rapidly as θ_ν increases [49], [107], [22], [20]. In these models, XRFs are those events observed off-axis and the XRFs rate with respect to GRBs and the $E_{p,i}$ – E_{iso} correlation can be correctly predicted.

Ghirlanda et al. (2012) [43] measured directly θ_{jet} through the jet break ti-

me observed in the optical lightcurves and found that $\theta_{jet} \sim 5$ deg; however, the limited number of events with a direct estimate of θ_{jet} and the possible selection effects prevent them from assuming it as representative of the GRB population. So in their work they used a population synthesis code to simulate GRBs with different assigned distributions of θ_{jet}, each one with a set of free parameters that they left free to vary within certain ranges. They did not assume the observed distributions of θ_{jet} as constraints to avoid circularity. They assumed that GRBs have a unique comoving frame peak energy E'_p and collimation-corrected energy E'_γ which are transformed into their corresponding rest-frame E_p and E_γ respectively. The assigned θ_{jet} and Γ_0 allow them to derive the isotropic equivalent energy of the simulated bursts according to the relative value of θ_{jet}. They found that $E_{iso} \sim E_\gamma/\theta^2_{jet}$ if $sin\theta_{jet} > 1/\Gamma_0$, while $E_{iso} \sim E_\gamma\Gamma^2_0$ in the opposite case. This introduces a "natural bias" in the distribution of E_{iso}: those bursts with a small enough Γ_0 will have an isotropic energy which is smaller than that one would calculate using the value of θ_{jet}. Their simulation also predicts that there are bursts with no jet break, those with $1/\Gamma_0 > sin\theta_{jet}$. Their afterglows will never have a jet break since the condition $1/\Gamma_0 \sim sin\theta_{jet}$ is never met but their afterglow lightcurve should have a characteristic post-jet break intermediate/steep decay slope. These should be $\sim 6\%$ of the bursts pointing to us and $\sim 2\%$ of the bursts detected by Swift.

They considered two types of distributions for θ_{jet} and Γ_0: a power law distribution, i.e. θ_{jet} and Γ_0 do not assume any preferential value, or both θ_{jet} and Γ_0 have peaked distributions (either broken power law or a log-normal distributions). In order to test these two hypotheses they compared the results of their simulations with three GRB samples. Their main result is that they cannot reproduce all our observational constraints if the Γ_0 and θ_{jet} distributions are power laws. Instead, if θ_{jet} and Γ_0 have broken power law distributions (with peak values $\theta_{jet} \sim 4.5$ deg and $\Gamma_0 \sim 70$) or log-normal distributions (with peak values $\theta_{jet} \sim 4.5$ deg and $\Gamma_0 \sim 85$) a better agreement between the simulations and the observational constraints is found. An immediate consequence of their results is that the large scatter of the $E_{p,i}$ – E_{iso} correlation can be interpreted as due to the jet opening angle distribution of GRBs, as we have obtained. The found inverse relation between θ_{jet} and Γ_0 implies that bursts with the largest bulk Lorentz factors should have a smaller average θ_{jet}. Bursts with relatively low average Γ_0 factors should also have, on average, large θ_{jet}.

Thanks to our time resolved analysis which provided a value of dispersion

~ 0.1 due to the jet opening angles, we can extract more direct and model independent information on the distribution of these angles. Indeed, this result implies that the distribution of log(1-cosθ) is about 0.2, thus we could infer information on the shape of the distribution of jet opening angles.

3.3 Implications for cosmology

One of the main goals of this time-resolved analysis is to place some constraints on cosmological parameters through the use of GRBs. We have pursued this goal by following the same procedure made by Amati et al. (2008) [3]; in order to avoid the so called "circularity problem" we have fit simultaneously through Reichardt function all the parameters of the correlation with the cosmological ones (see section 1.5), with the exception that we have used as prior the slope obtained through our work. To note the contribution of our "calibration" work, we have used a sample of 193 GRBs, with measured E_p and E_{iso}, known redshift and accurate spectral measurements, updated to 2017 (Amati and Sawant 2017, in preparation).
Firstly, in the scheme that we call scheme 1, we have assumed a ΛCDM model of the Universe by fixing $w_0 = -1$ and $w_a = 0$ (we do not consider now any evolution in time of dark energy) in the equation of State of the dark energy, expressed as $P = w(z)\rho$, where $w(z) = w_0 + w_a z/(1+z)$; thus, we have fit the correlation by considering the slope free; secondly, in scheme 2, we have fit the correlation by using as prior the value of m obtained through the simultaneous fit (see section 2.5) performed with Preece et al. data, i.e. $m = 0.50 \pm 0.02$. We have decided to use these data because Preece et al. catalog provides more accurate measurements than those of Yu et al. catalog, as already said. This value for slope has been confirmed by the simultaneous fit made with Yu et al. data (see section 2.3); similarly, in scheme 3, we have repeated the fit by fixing the value of $m = 0.5$, i.e. the mean value obtained in the analysis with both catalogs (see sections 2.3 and 2.5). Finally, in scheme 3 we have obtained a lower value of Ω_M with respect to what found with other probes [104]. Even though this finding may be due to a statistics effect, we have performed the analysis also by assuming that the dark energy has evolved in time, i.e. we have fixed $w_a = -1$ and m = 0.5. This scheme is called 4. In this way, Ω_M value has increased with respect to to scheme 3. The results are shown in the Tab. 3.1, where we present the errors of Ω_M at 1 σ and 2 σ. In Fig. 3.2 we show the goodness–of–fit of the $E_{p,i}$ – E_{iso}

correlation, in terms of normalized $-log(likelihood)$, of 193 long GRBs as a function of the value of Ω_M, of three different fits, i.e. scheme 1, 2, and 3. The cosmology and jet opening angle independent calibration of the slo-

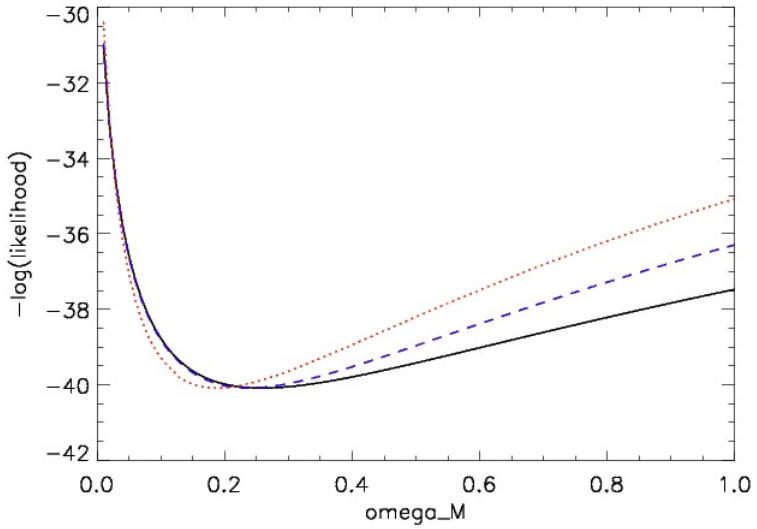

Figura 3.2: The graph illustrates three different -log(likelihood) as a function of Ω_M obtained in scheme 1 (black line), in scheme 2 (violet line) and in scheme 3 (red line).

pe of the E_p - Intensity correlation obtained with our analysis provides a significant improvement in the accuracy of the estimate of Ω_M with GRBs (see Tab. 3.1). This confirms the relevance, also in perspective of the advent of more sensitive GRB detectors (HXMT-HE, see next chapter; SVOM, THESEUS), of the time-resolved E_p-L correlation for the reliability and full exploitation of GRBs as tools for measuring the expansion rate and geometry of the Universe. Indeed, beyond a further and independent confirmation of $\Omega_M \sim 0.25 - 0.3$, as resulting from several other cosmological probes (e.g. SNe-Ia, BAO), our results strengthen the perspective of using GRBs to investigate a possible evolution of "Dark Energy" and alternative scenarios. The substantial increase of GRBs with measured redshift and accurate estimates of E_p expected in the next years will allow an improvement of the accuracy of the calibration of the E_p-L correlation through our method. As demonstrated by different simulations (e.g., [41], [4]), in combination with a better statistical quality of the analysis due to the enlargement of the sample, this will make the E_p-L correlation of GRBs sensitive to the equation of State of

Dark Energy and to its possible evolution (e.g., constraints on w_0 and w_a; see chapter 1).

Tabella 3.1: Comparison of the 68% and 90% confidence intervals (c.l.) on Ω_M obtained with the sample of 193 GRBs, for a flat FLRW universe, with m free, with m as result of the simultaneous fit (see Sec. 2.5) and with a fixed valued of m=0.5, respectively. Only the last line refers to a Universe in which dark energy evolves in time.

	Ω_M (68% c.l.)	Ω_M (90% c.l.)
Scheme 1 $\Longrightarrow m_{free}$	$0.26^{+0.23}_{-0.13}$	$0.26^{+0.46}_{-0.17}$
Scheme 2$\Longrightarrow m_{simultaneous fit}$	$0.24^{+0.18}_{-0.11}$	$0.24^{+0.36}_{-0.16}$
Scheme 3$\Longrightarrow m = 0.5$	$0.18^{+0.14}_{-0.07}$	$0.18^{+0.28}_{-0.10}$
Scheme 4$\Longrightarrow m = 0.5$ ($w_0 = -1$ and $w_a = -1$)	$0.21^{+0.15}_{-0.08}$	$0.21^{+0.29}_{-0.12}$

Capitolo 4

Expected contribution from next-generation experiments: the case of HXMT

The Hard X-ray Modulation Telescope (HXMT) is the first Chinese satellite devoted to X-ray astrophysics, launched on June 14^{th} 2017 from Juquan in the Gobi desert. HXMT will allow a high sensitive study of the X-ray sky in 1-250 keV band, thanks to a smart combination of collimated detectors operating in different energy bands and providing a source location accuracy of ~ 1 arcmin. In addition to these features in standard configuration, the HXMT High-Energy (HE) instrument will be operated also in a modality that will allow to detect and characterize GRB prompt emission from 200 keV to 3 MeV with an effective area as high as $\sim 2000\ cm^2$, thus filling the sensitivity gap of presently flying main GRB detectors in this energy range. More specifically, its payload consists of three collimated instruments covering a total energy band of 1-250 keV [115]: the Low-Energy instrument (LE) is based on Swept Charge Devices (SCD), operating in the 1-15 keV energy band, with a total geometrical area of 384 cm^2, 1 ms time resolution and an energy resolution of 7.5% at 6 keV; the Medium-Energy instrument (ME) will use SI-PIN detectors to cover the 5-30 keV energy band with a total geometrical area of 952 cm^2, 15% energy resolution at 20 keV and a time resolution similar to the LE; lastly, an extension to the hard X-rays will be provided by the High-Energy instrument (HE), made of 18 phoswich detection units (NaI(Tl)+ CsI(NaI)) operating in the 20-250 keV, with a total geometric area of $\sim 5000\ cm^2$, a time resolution of $25\mu s$ and an energy

resolution of 19% at 60 keV (Fig. 4.1). Moreover, the different orientations of the collimators of the HE instrument will allow to pinpoint sources with $\sim$ 1 arcmin accuracy through the direct demodulation technique (Li & Wu 1993).
The satellite, featuring a total weight of $\sim$ 2500 kg, has been launched into a circular orbit with an altitude of 550 km and an inclination of 43 deg.

These properties will allow HXMT to perform broad-band and high-accuracy spectral and temporal studies of several classes of X-ray sources through pointed observations (including very bright sources, given that the LE has no pile-up problems), as well as frequent surveys of the Galactic plane and ridge, with the expected discovery of new transient X-ray sources thanks to the unprecedented sensitivity in the hard X-rays.
Moreover, HXMT, by exploiting the multiple-FOV method and the knowledge of its internal background thanks to the addition of blinded units to each instrument, will provide a measurement of the CXB spectrum over the 1-250 keV energy band, with unprecedented sensitivity at energies > 20 keV.
In addition to the normal features described above, the HXMT/HE instrument will be operated also in a GRB modality that will allow to derive with high accuracy the temporal and spectral properties of the detected GRBs in the energy range from 200 keV to 3 MeV, thanks to an average effective

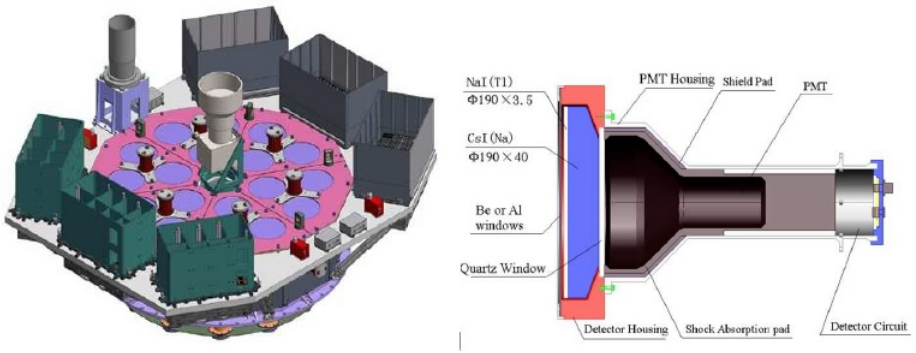

Figura 4.1: Sketch of the HXMT payload. The green boxes on the left show the LE instrument, whereas the gray boxes on the right are the ME instrument. The HE instrument, which will also be operated as a GRB monitor, is made of the 18 units (here shown in violet color) filling the central part of the optical bench. Two star trackers (ST) are also shown in the central and top-left position of this representation of the payload accommodation. On the right we can see one unit of detection of HE.

area[1] of $\sim 1500 - 2000\ cm^2$. In the GRB operation mode, modality which is activated during Earth occultation of pointed sources, the HV (i.e. High Voltage) of the HE instrument units is lowered, in order to reduce the gain by a factor of ~ 5, thus changing the energy band of the NaI detectors from 20-250 keV to 100-1250 keV and that of the CsI from 40-600 keV to 200-3000 keV. The effective area is shown in Fig. 4.2 as a function of photon energy in GRB mode, as derived by means of extensive Monte Carlo simulations. In this way, HXMT will complement perfectly the sensitivities of presently flying main GRB detectors, like, e.g., Swift/BAT and Fermi/GBM, the former being limited to an energy band of 15-300 keV [35], and the latter covering photon energies from ~ 10 keV up to 20-30 MeV, but with an effective area $< 200\ cm^2$. Because of the above mentioned energy band and sensitivity limitations, Swift/BAT measures mostly power-law spectra, thus providing estimates of E_p only for a small fraction of GRBs and almost no estimates of the high energy index β, and most Fermi/GBM spectra can be fit with a cut-off power-law, which provides no information on β and a possible overestimate of E_p, because it has not enough sensibility to detect sufficiently the spectral curvature at higher energies. Therefore HXMT can provide a relevant contribution to the understanding of the physics of the prompt emission, one of the main open issues in the GRB field.
I performed some simulations aimed at quantifying the expected performances of HXMT for GRBs alone and in combination with Fermi/GBM measurements. The simulations were performed using the XSPEC X-ray spectral fitting package [5]. The response matrix [2] of HXMT/HE in GRB mode was obtained through intensive Monte Carlo simulations of the instrument and of the whole satellite, combined with extensive on-ground calibrations (see, e.g., [115]). In particular, we used the response matrix for an offset incident angle of 135 deg, which is the rear side direction. The background spectrum was

[1]The effective area depends on the geometric area of the telescope, on the fraction of photons reflected by the mirros (reflectivity), the fraction of "lost" photons (vignetting) and fraction of incident photons on the detector actually registered by the detector (quantum efficiency).

[2]The response of a detector, whose signal depends of the energy of an incoming photon, like a proportional counter, distributes the photons of a certain energy over many pulse height channels according to the gain and energy resolution of the detector. Usually this resolution function is relative complicated and depends on the photon energy. Since the resolution of a given detector is determined by its design it is convenient to table this function while the photon energy serves as a parameter. This procedure leads directly to a form of a matrix and gives the whole data set the name detector response matrix.

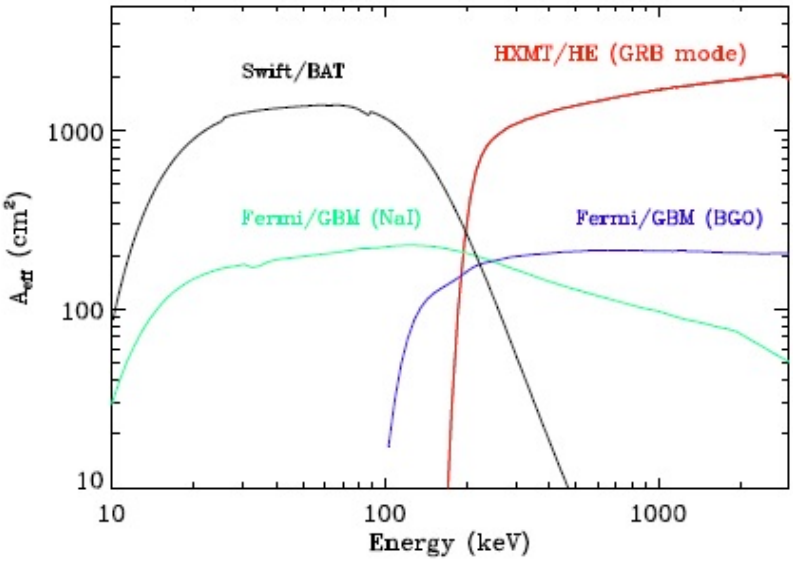

Figura 4.2: Effective area as a function of energy for Swift/BAT (on-axis), Fermi/GBM (sum of two NaI detectors and BGO) and HXMT (in GRB mode).

derived by taking into account the expected in-flight background components, including CXB (cosmic X-ray background), primary and albedo protons, electrons and positrons, gamma-rays albedo and SAA (South Athlantic Anomaly) proton activated fluorescence by instrument and satellite structures.
For Fermi/GBM, spectra have been simulated by using the response matrices and background files from observations of a real GRB. In particular, we have simulated the spectra of two NaI detectors and the BGO detector, according to typical analysis of real data.
Firstly, we have simulated the spectrum of a medium-weak intensity GRB (10–1000 keV fluence of 5×10^{-6} $erg\ cm^{-2}$) with a typical Band spectral shape and $\alpha = -1$, $\beta = -2.3$, $E_p = 300$ keV and 25 s duration. (Fig. 4.3). As can be seen, for such a GRB, while the BGO would provide only an upper limit, HXMT would give a sensitive spectral measurement up to a few MeV, thus providing a fundamental contribution to the estimate of spectral peak energy and high–energy spectral index.
Then, in order to quantify the improvement in the accuracy in the estimates of E_p and β, which would be obtained by adding HXMT to Fermi/GBM, we simulated a set of Fermi/GBM and HXMT/HE spectra by assuming the

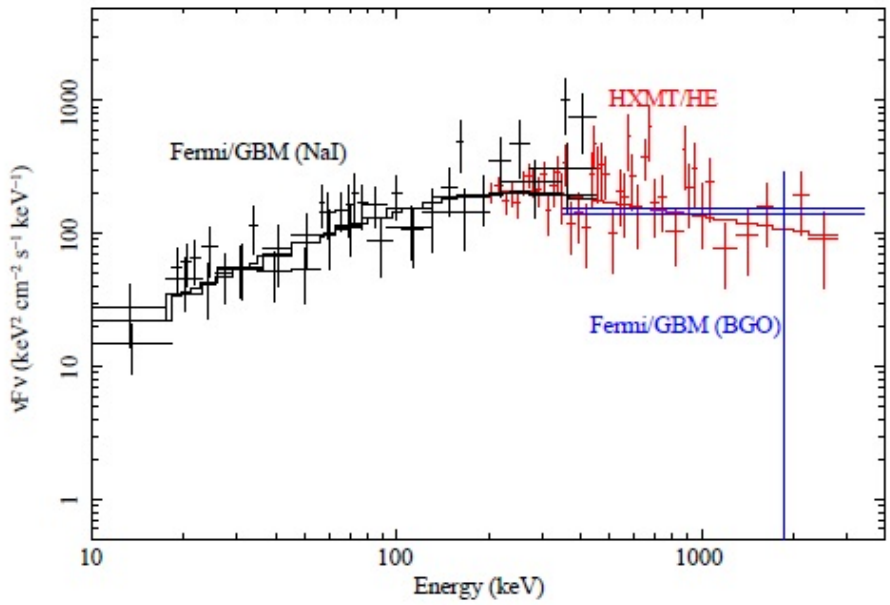

Figura 4.3: Simulated Fermi/GBM and HXMT/HE (GRB mode) spectra of a medium-weak GRB (10-1000 keV fluence of 5×10^{-6} erg cm^{-2}) with a typical Band spectral shape with $\alpha = -1$, $\beta = -2.3$ and $E_p = 300$ keV and 25 s duration. At high energies Fermi BGO (blue point) is not statistically relevant and can be treated as an upper limit; conversely, HXMT can better detect the high energy tail.

typical spectral shape and parameters (i.e. $\alpha = -1$, $\beta = -2.3$ and $E_p = 300$ keV) and a 10–1000 keV fluence varying from 10^{-4} to 10^{-7} erg cm^{-2}. Thereafter, we have fitted these spectra by considering all these parameters free, in order to check the accuracy of the estimates of E_p and β obtained.
The results are reported in Fig. 4.4 and Fig. 4.5, in terms of fractional 1σ uncertainty in the estimates of respectively E_p and β as a function of GRB fluence. We can notice that GBM can measure E_p, even for medium/weak GRBs, better than HXMT because the latter has an effective area whose energy range starts at some hundreds of keV, so it cannot constrain well E_p, whose distribution of values peaks at 300 keV, as we have already said. GBM can measure well β only for the brightest GRBs. Conversely, HXMT can better constrain β, arriving at higher energies than the GBM, while it measures E_p only for the brightest GRBs. Given the value of 300 keV

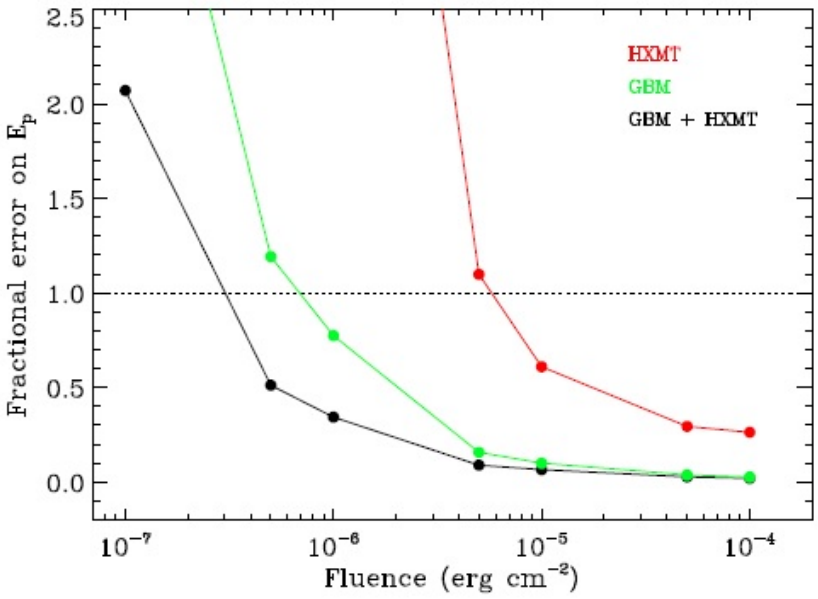

Figura 4.4: Fractional error on E_p as a function of fluence (10-1000 keV) for a GRB with $\alpha = -1$, $\beta = -2.3$ and $E_p = 300$ keV and duration 25 s, as would be measured by Fermi/GBM alone, HXMT/HE alone and a joint spectral analysis of spectra from the two instruments. A fractional error higher than 1 is indicative that the measure is an upper limit.

assumed for E_p, HXMT/HE alone can provide a good measurement of the spectral peak energy only for the brightest GRBs, while it can provide an

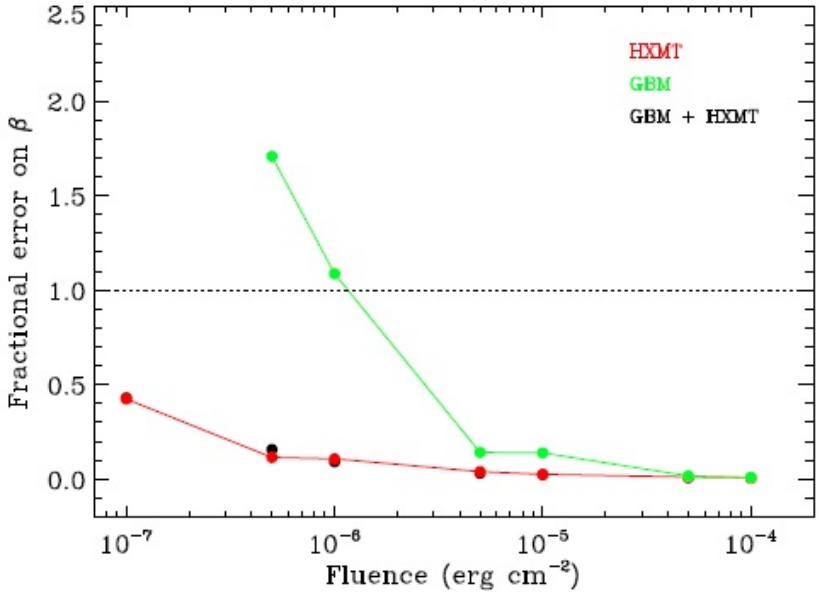

Figura 4.5: Fractional error on β as a function of fluence (10-1000 keV) for a GRB with α=-1, β=-2.3 and E_p=300 keV and duration 25 s, as would be measured with Fermi/GBM alone, HXMT/HE alone and a joint spectral analysis of spectra from the two instruments. A fractional error higher than 1 is an upper limit.

accurate estimate of β down to the faintest ones (i.e. 10-1000 keV fluence of $5 \times 10^{-7} erg\ cm^{-2}$). Conversely, the Fermi/GBM alone can provide good measurements of E_p down to medium-bright GRBs (i.e. 10-1000 keV fluence of $5 \times 10^{-6} erg\ cm^{-2}$).
However, it is only with the joint analysis of the spectra of the two instruments that it will be possible to get a sensitive measurement of E_p down to fluences as low as 5×10^{-7} erg cm^{-2}.
In Fig.4.6 we report a comparison of the accuracy in the estimate of E_p as a function of flux from time-resolved spectral analysis as obtained for GRB080817 by using Fermi/GBM alone (true spectra) (from Yu et al. 2016 [109]) and by the joint analysis of Fermi /GBM and HXMT/HE (GRB mode) spectra (simulated); for the latter, we have assumed as model the effective values (previously measured) of α, β and E_p for each interval of the same burst, and then we have fitted the simulated spectra, by considering all these parameters free. We can see that the accuracy in measurements made by a joint analysis between HXMT and Fermi/GBM is absolutely improved with respect to Fermi/GBM alone (Fig. 4.6).

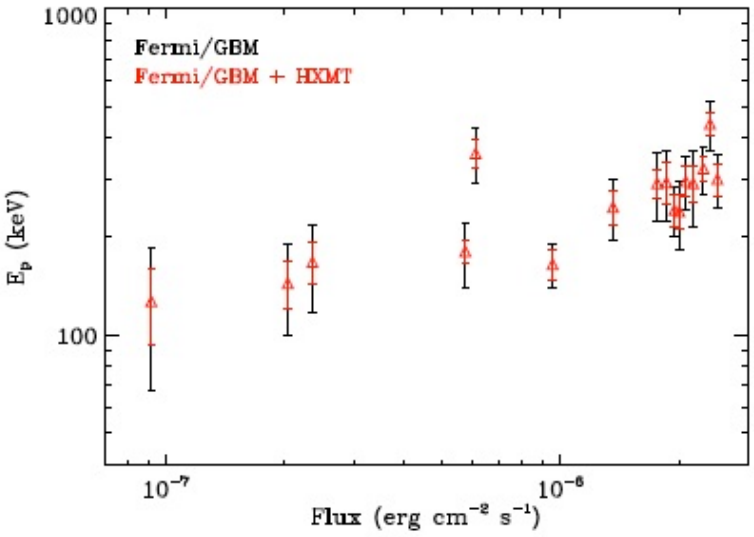

Figura 4.6: Comparison between the accuracy in the estimate of E_p as a function of flux from time-resolved spectral analysis as obtained for GRB080817 by using Fermi/GBM alone (black points, from Yu et al. 2016) and by the joint analysis of Fermi/GBM and HXMT/HE (GRB mode, simulated) spectra (red points).

We can safely conclude that the addition of HXMT data to those presen-

tly available not only will turn into more accurate measurements of the key spectral parameters, but will also extend the possibility of measuring them to much weaker fluences (down to 10^{-7} erg cm^{-2}) and will provide more insights into their temporal evolution with respect to what is feasible with current experiments alone.

Capitolo 5

Conclusions and perspectives

The physics of the prompt emission, jet structures and opening angles of GRBs and the reliability of the techniques aimed at standardizing them for cosmology are among the most relevant open issues still affecting our full understanding and exploitation of GRBs. Under these respects, an important and deeply investigated property of GRBs is the existence of the correlation between the spectral peak energy (at which a typical GRB νFν spectrum peaks) and the burst "intensity", i.e., the radiated energy (E_{iso}), peak luminosity (L_p) or average luminosity (L_{iso}). On the one side, the properties of this power–law correlation, i.e. its slope and dispersion, provide a fundamental test and input for GRB prompt emission mechanisms and geometry; on the other side, it represents the most promising and effective tool for using GRBs as probes of the geometry and expansion rate of the Universe.
The research work reported in this Thesis is focused on the further characterization and calibration of the time-resolved $E_{p,i}$ - Luminosity correlation in GRBs based on the systematic analysis of the measurements by Fermi/GBM and CGRO/BATSE. The fact that the $E_{p,i}$ - Luminosity correlation holds also "within" individual GRBs provides a decisive confirmation of the physical reliability of the most investigated E_p - "intensity" correlations based on time-integrated spectra ($E_{p,i}$ - E_{iso} "Amati relation", $E_{p,i}$ - L_p "Yonetoku" relation, etc.). Over the last years, a few research groups have investigated this correlation mostly using Fermi/GBM spectral measurements of GRBs with known redshift. If we place in the same graph the values of $E_{p,i}$ and Luminosity of the different time intervals of different GRBs, we can obtain a correlation with a slope and dispersion consistent with that of the "Amati" relation. This supports the picture that the main emission mechanism at

work during the prompt emission of GRBs produces a power–law correlation between spectral peak energy and luminosity with slope ∼0.5; this evidence is useful in discriminating and developing further the numerous proposed models differing in the emission process (e.g. synchrotron, Comptonization, thermal), in the degree of magnetization of the jet, etc. Moreover, it confirms that the $E_{p,i}$ - E_{iso} and E_p - L_p correlations are not significantly affected by selection effects, providing reliability to their use for "standardizing" GRBs. However, the results of the studies based on datasets of GRBs with known redshift are affected by two main limitations: they depend on the cosmological model assumed (thus introducing a "circularity" when one wants to use this correlation for standardizing GRBs) and by our limited knowledge on the different jet opening angles, which forces the use of an "isotropic-equivalent" luminosity.
The basic idea behind our analysis was to address these two issues, thus making a significant step forward in the use of the $E_{p,i}$ - L correlation for GRB physics and cosmology; in this regard we use time-resolved analysis of large samples of GRBs without measured redshift, i.e, by going back to the E_p - Flux plane. Indeed, for a single GRB, the measured time-resolved E_p - Flux correlation has the same slope and dispersion of its intrinsic $E_{p,i}$ - L correlation, independently on the cosmological model and its jet opening angle. The systematic study of the distributions of the values obtained by fitting the E_p - Flux correlation of each GRB provides a cosmology-independent and unbiased estimate and calibration of the slope and dispersion of the E_p - L correlation.
Firstly, in this work I have focused the analysis on GRBs with Fermi/GBM data analyzed by Yu et al. (2016); I have studied how the distributions of the slope and dispersion of E_p – Flux correlation obtained through two different methods (i.e. a least squares linear fit and a likelihood function accounting for the extra-Poissonian dispersion proposed by Reichardt 2001) depend on various factors, such as, e.g., the fraction of the GRB duration considered in the fit, the goodness–of–fit and the model used for fitting the spectra. Moreover, an innovative aspect of this thesis consists in fitting, with the Reichardt function, the E_p – Flux values of the time intervals of all GRBs simultaneously, under the assumption that all GRBs follow the same correlation.

This systematic analysis of the Yu et al. catalog provides indication that the slope of E_p - L correlation is about ~ 0.5 and its intrinsic dispersion is about half of that of the E_p – E_{iso} and other correlations based on time-

integrated/averaged spectra (about 0.1 dex). The results of the simultaneous fit converge to the same conclusion with a higher level of accuracy. In addition, a fraction of GRBs show significant deviations from the E_p – Flux correlation, particularly during the rising phase of the first part and in the final part of the emission. In order to investigate the reliability of these deviations, I have independently reduced the spectra of these GRBs with two different tools (RMFIT 1 v4.3BA and XSPEC) and adopted different statistics and techniques for background subtraction. I find that it is not possible to provide a firm evidence of the lack of E_p – Flux tracking (especially in the rising phase) based on Fermi/GBM data, because of relevant background subtraction issues of this instrument for low source fluxes.
Subsequently, the same investigation has been performed with the time-resolved spectral analysis of bright BATSE GRBs reported by Preece et al. (2000). This analysis of BATSE data allows us a more accurate measurement of the spectral parameters and of slope and dispersion of E_p - L correlation, confirming and strenghtening the results obtained based on GBM data by Yu et al. Furthermore, the absence of correlation between E_p and Flux during the rising and the final part of the emission in a small fraction of GRBs ($\sim 1/3$) seems effective based on BATSE data. As for the analysis of Yu et al., the simultaneous fit of the data of all GRBs provides more accurate estimates for the slope and the scatter with respect to the analysis of the distributions of the results of the fits of single GRBs.
As discussed above, the unbiased (from cosmological and jet opening angles effects) characterization of the slope and dispersion of the E_p – Luminosity correlation strenghtens its implications for GRB physics and cosmology. A striking result is that the value of $m = 0.5$ is not consistent with that obtained by Nava et al. (2006) [79], who corrected the E_p – L_{iso} correlation for the jet angle, finding $m \sim 0.7-1$. Different values of m have been calculated by using different physical models for the radiation mechanism. For instance, a power-law electron distribution generated in an internal shock within a fireball can led to a value of $m = 0.5$, similar to an emission mechanism due to synchrotron radiation (see Sec. 3.1.1).
Also the value of the extra-poissonian scatter (σ_{ext}) of the E_p – Flux correlation can shed some light on the model which can account for the physics of the prompt emission (see Sec. 3.1.3). For instance, the value of ~ 0.1 dex is challenging for internal shocks models which predict a significantly larger dispersion. This quantity provides also insights on the jet opening angles. Our results suggest that half of the scatter of the E_p – E_{iso} or E_p – L is due

to the distribution of jet opening angles, although viewing angle effects and the inhomogeneity of the structure of the jet may also play a role (see Sec. 3.2).
An important result of this work is also that there are time intervals in which GRBs apparently do not follow the correlation. Some authors believe that the decaying phase of the correlation may be the main source of the global E_p – flux correlation. The different behavior of E_p in correlation with the flux (i.e. "intensity tracking" or hard-to-soft evolution) could be explained by different kind of models, but a detailed theoretical modeling is desirable, in order also to explain the coexistence of different evolutionary trends in different pulses of the same burst (see Sec. 3.1.2).
Finally, I have discussed on the main implications of this kind of time-resolved analysis for cosmology. Thanks to the calibration of the slope of the correlation carried out in this work, using accurate spectral measurements obtained by a sensitive instrument such as BATSE, I was able to place more stringent constraints on cosmological parameters like Ω_M by using the results obtained through the simultaneous fit. The accuracy of the estimate of Ω_M with GRBs has been improved by about $\sim 15-20\%$ with respect to the previous time-integrated analysis made by other authors: I have obtained a value of $\Omega_M = 0.24^{+0.18}_{-0.11}$, while without calibrating the slope the value of Ω_M is $\Omega_M = 0.26^{+0.23}_{-0.13}$ (see Tab. 3.1 in Sec. 3.3). More in general and in perspective, the cosmology and jet opening angle independent calibration of the slope of the E_p – Luminosity correlation made possible by the analysis reported in this thesis is a fundamental step towards the possibility and reliability of using GRBs for investigating the nature and the evolution of "Dark Energy", in a complementary way to other probes.
In conclusion, I can say that the method adopted in my thesis work is innovative since, for the first time, with such a high level of precision in its characterization, I have performed, for the first time, a time-resolved analysis of data collected by the BATSE instrument, which provides accurate spectral measurements.
Moreover, the present results have been supported by the comparison between two sets of data, i.e. Yu et al. and Preece et al. catalogs, by obtaining a further confirmation of our results.
A forward step in the understanding GRB phenomenon will be provided by the satellite HXMT launched in the mid of June 2017 (named "Insight"). In this regard, I have simulated its expected performances in the context of the collaboration of the GRB group of INAF-IASF of Bologna with the Uni-

versity of Ferrara and the Chinese group involved in the mission. A better calibration of the slope and dispersion of the E_p – Luminosity correlation will be also possible with future missions, such as SVOM (it will be launched in 2022) and proposed THESEUS (2029), which will perform spectral measurements of prompt GRB emission with a larger effective area and in a broader energy band with respect to present flying telescopes and will increase the number of GRBs with known redshift by more than one order of magnitude.

Bibliografia

[1] L. Amati et al., 2002, A&A, 390, 81

[2] L. Amati et al., 2006, MNRAS, 372, 233

[3] L. Amati et al. 2008, MNRAS, 391, 577

[4] L. Amati and M. Della Valle, 2013, Int.J.Mod.Phys. D 22, 1330028

[5] K.A. Arnaud, 1996, ASP Conference Series, 101, 17

[6] D. Band et al., 1993, ApJ, 413, 281

[7] A.M. Beloborodov, 2009, MNRAS, arXiv:0907.0732

[8] E. Berger, S.R. Kulkarni and D.A. Frail, 2003, ApJ, 590, 379

[9] R.D. Blandford and R.L. Znajek, 1977, MNRAS, 179, 433

[10] Z. Bosnjak et al., 2006, A&A, astro-ph/0502185

[11] D.N. Burrows et al., 2005, Science, 309, 1833

[12] S. Campana et al., 2006, Nature, 442, 1008-1010

[13] W. Cash, 1979, ApJ, 228, 939-947

[14] G. Chincarini et al., 2010, MNRAS, 406, 2113

[15] E. Costa et al., 1997, Nature, 387, 783

[16] G. D'Agostini, 2005, arXiv:0511182

[17] X. Dai and B. Zhang, 2005, ApJ, 621, 875

[18] W. Deng and B. Zhang, in preparation

[19] C.D. Dermer, 2004, ApJ, 614, 284

[20] T.Q. Donaghy, 2006, ApJ, 645, 436

[21] J. Dyks, B. Zhang and Y.Z. Fan, 2006, ApJ, 642, 354

[22] D. Eichler and A. Levinson, 2004, ApJ, 614, L13

[23] Y.Z. Fan and D.M. Wei, 2005, MNRAS, 364, L42

[24] E.E. Fenimore et al., 1996, ApJ, 460, 964

[25] C. Firmani et al., 2009, MNRAS, 393, 1209

[26] G. Fishman et al., 1994, ApJ Supp, 92, 229

[27] G. Fishman et al., 1995, ARA&A, 33, 415

[28] G. Fishman et al., 1999, A&AS, 138, 395

[29] D.A. Frail et al., 1997, Nature, 389, 261-263

[30] D.A. Frail et al., 2001, ApJ, 562, L55

[31] F. Frontera et al., 2000, ApJS, 127, 59

[32] F. Frontera et al., 2012, ApJ, 754, 138

[33] F. Frontera et al., 2013, ApJ, 779, 175

[34] T.J. Galama et al., 1998, Nature, 395, 670-672

[35] N. Gehrels et al., 2004, ApJ, 611, 1005-1020

[36] B. Gendre et al., 2013, ApJ, 766, 30

[37] D. Giannios, 2008, A&A, 480, 305

[38] G. Ghirlanda et al. 2003, A&A, 406, 879

[39] G. Ghirlanda et al., 2004c, ApJ, 613, L13

[40] G. Ghirlanda et al., 2005, MNRAS, 360, L45

[41] G. Ghirlanda et al., 2006, New J. Phys., 360, L45

[42] G. Ghirlanda et al., 2009, A&A, 496, 585

[43] G. Ghirlanda et al., 2012, MNRAS, 422, 2553

[44] G. Ghirlanda, A. Celotti and G. Ghisellini, 2003, A&A, 406, 879

[45] G. Ghirlanda et al., 2005, MNRAS, 361, L10

[46] G. Ghisellini et al., 2000, MNRAS, 316, L45

[47] G. Ghisellini et al. 2001, arXiv:0111584

[48] S. Golenetsky et al. 1983, Nature, 306, 45

[49] J. Granot et al., 2002, ApJ, 570, L61-L64

[50] D. Gruber et al., 2014, ApJ, 211, 12

[51] S. Guiriec et al., 2015, ApJ, 814, 10

[52] J. Hjorth et al., 2003, Nature, 423, 847

[53] K. Ioka, 2010, Prog. Theor. Phys., 123, 743-755

[54] P. Jakobsson et al., 2010, GRB Coordinates Network, 10438, 1

[55] R. Klebesadel et al., 1973, ApJ, 182, L85-L88

[56] C. Kouveliotou et al., 1993, ApJ, 413, L101

[57] C. Kouveliotou et al., 1995, Astroph. Sp. Sci, 231, 49

[58] P. Kumar and A. Panaitescu, 2000, ApJ, 541, L51-L54

[59] D.Q. Lamb et al., 2004, NewA Rev., 48, 423

[60] D.Q. Lamb et al., 2005, ApJ, 620, 355

[61] D. Lazzati and M.C. Begelman, 2009, ApJ, 700, L141

[62] D. Lazzati and R. Perna, 2007, MNRAS, 375, L46

[63] W.H. Lee and E. Ramirez-Luiz, 2007, New J. Phys., 8, 123

[64] A. Levan et al., 2014, ApJ, 781, 13

[65] A. Levinson and D. Eichler, 2005, ApJ, 629, L13

[66] E.W. Liang et al., 2004, ApJ, 606, L29

[67] E.W. Liang and B. Zhang, 2006, ApJ, 638, L67

[68] T. Liu et al, 2016, ApJ, 821, 132

[69] N.M. Lloyd and R.S. Petrosian, 2002, ApJ, 565, 182-194

[70] N.M. Lloyd, V. Petrosian and R.S. Mallozzi, 2000, ApJ, 534, 227-238

[71] N.M. Lloyd-Ronning, X. Dai and B. Zhang, 2004, ApJ, 601, 371

[72] R.J. Lu et al., 2012, ApJ, 756, 112

[73] A.I. MacFadyen and S.E. Woosley, 1999, ApJ, 524, 1

[74] R. Margutti et al., 2011, MNRAS, 417, 2144

[75] C. Meegan et al., 1996, ApJS, 106, 65

[76] C. Meegan et al., 1999, ApJS, 122, 465-495

[77] M.R. Metzger et al., 1997, Nature, 387, 878

[78] Mochovitch et al., 2015, A&A, 576, A31

[79] L. Nava et al., 2006, A&A, 450, 471

[80] L. Nava et al. 2007, MNRAS, arXiv:0701705

[81] L. Nava et al., 2011, A&A, 530, A21

[82] J.A. Nousek et al., 2006, ApJ, 642, 389-400

[83] B. Paciesas et al. 1999, ApJS, 122, 465

[84] A. Pe'er et al., 2006, ApJ, 642, 995

[85] E. Pian et al., 1998, GCN Report, 61

[86] E. Pian et al., 2006, Nature, 442, 1011-1013

[87] R.D. Preece et al., 2000, ApJS, 126, 19

[88] R.D. Preece et al., 2013, Science Express, arXiv:1311.5581

[89] Y.-P. Qin, 2008, ApJ, arXiv:0804.2175

[90] J.L. Ramirez-Ruiz et al., 2005, ApJ, 625, L91

[91] M.J. Rees and P. Meszaros, 2005, ApJ, 628, 847

[92] E. Rossi, D. Lazzati and M.J. Rees, 2002, MNRAS, 332, 94

[93] F. Ryde, 2005, A&A, 429, 869

[94] F. Ryde et al., 2011, MNRAS, 415, 3693

[95] R. Sari et al., 1998, ApJ, 497, L17

[96] B.E. Schaefer et al., 2003, 588, 387-399

[97] K.Z. Stanek et al., 2003, ApJ, 591, L17-L20

[98] M. Tavani et al., 1995, , Ap&SS, 231, 181

[99] L. Titarchuk et al., 2012, ApJ, 752, 116

[100] K. Toma et al. 2005, ApJ, 635, 481

[101] K. Toma et al., 2011, MNRAS, 415, 1663

[102] J. Van Paradijs et al., 1997, Nature, 386, 686

[103] A. von Kienlin et al., 2014, ApJS, 211, 13

[104] D.H. Weinberg et al., 2013, Phys. Rep., 530, 87

[105] S.E. Woosley, 1993, ApJ, 405, 273

[106] R. Yamazaki et al., 2003, ApJL, 594, L79

[107] R. Yamazaki, K. Ioka and D. Nakamura, 2003, ApJ, 591, 283

[108] D. Yonetoku et al. 2004, ApJ, 609, 935

[109] H.F. Yu et al., 2016, A&A 588, A135

[110] B. Zhang et al, 2002, ApJ, 581, 1236-1247

[111] B. Zhang et al., 2004, ApJ, 601, L119

[112] B. Zhang et al, 2006, ApJ, 642, 354

[113] B. Zhang et al., 2009, ApJ, arXiv:0902.2419

[114] B. Zhang et al., 2011, ApJ, 730, 141

[115] B. Zhang et al., 2014, ApJ, 787, 66

[116] B. Zhang and H. Yan, 2011, ApJ, 726, 90

[117] B. Zhang and P. Kumar et al., 2015, PhR, 561, 1

[118] B. Zhang and P. Mezsaros, 2002, ApJ, 571, 876